Experimental and Numerical Investigations on Sensible Heat Storage Systems

A thesis submitted in partial fulfilment of the requirements for the degree of

Doctor of Philosophy

By

Chilaka Ravichandra Rao

Department of Mechanical Engineering

Indian Institute of Technology Guwahati

Guwahati – 781039, India

October 2018

Department of Mechanical Engineering
Indian Institute of Technology Guwahati
Guwahati – 781039, India

THESIS CERTIFICATE

This is to certify that the work contained in the thesis entitled **Experimental and Numerical Investigations on Sensible Heat Storage Systems** by **Chilaka Ravichandra Rao**, a student of the Department of Mechanical Engineering, Indian Institute of Technology Guwahati, for the award of the degree of **Doctor of Philosophy** has been carried out under my supervision and that this work has not been submitted elsewhere for any degree.

Prof. P. Muthukumar

Department of Mechanical Engineering

Indian Institute of Technology Guwahati

Guwahati – 781039, India

Dedicated

To

My parents and family

Acknowledgement

It is my pleasure to acknowledge the roles of several individuals who have helped me in various ways during the tenure of my PhD work at IIT Guwahati. I have been supported and accompanied by many people and I am grateful to each and every one.

I am greatly indebted to my supervisor Prof. P. Muthukumar who inspired me to pursue research in the field of Solar Energy. I am highly grateful to him for his guidance and encouragement during the research work. Without his support, advice and motivation, it would have just been an impossible task for me to carry over this research work. I enjoyed each and every moment working under his supervision and learnt many things from him, which will be an asset for my future research. His inspiring guidance and most invaluable ideas have enabled me to overcome all the difficulties during my research work. I believe that the way he has shown is everlasting and fruitful to my career. Also, I feel it is worthwhile to mention about his financial assistance during the severe ill health situations, for which I am extremely grateful.

I would like to thank Department of Science and Technology (DST), Government of India, for their financial support in the fabrication of the experimental setup (Project No: DST/TM/SERI/2K10/53(G)). I am thankful to Prof. M Ramgopal (Dept. of ME) for providing valuable technical suggestions and ideas and to Prof. Charles Jacob (Dept. of Mat. Sc.) of IIT Kharagpur for providing the testing facilities to carry out this research. I would also, like to acknowledge the financial, academic and technical support of the Indian Institute of Technology Guwahati and its staff that provided the necessary support for continuing this research.

I would like to acknowledge to my doctoral committee members, Prof. Niranjan Sahoo (Chairman), Prof. Pugazhenthi G., and Dr. Pranab Kumar Mondal for their consistent support, constructive criticisms, valuable suggestions and direction during the course of this dissertation. I would like to express my sincere thanks to Prof. Debabrata Chakraborty (ex.HOD), Prof. Pinakeswar Mahanta (ex.HOD) and Prof. Anoop Kumar Das (ex.HOD) for providing all the facilities needed for my research work and the general issues. I am also thankful to the present head of the mechanical engineering department, Prof. Santosh Kumar Dwivedy for extending the department financial support during the tenure of my doctoral programme. I take this opportunity to thank all the faculty members of the department for their valuable suggestions and cooperation during my course work.

I am thankful to Dr. Arunbor Saikia, Scientific Officer (Dept. of Civil Engg), Hazarika, and Suresh of IIT Guwahati for their assistance whenever is needed during the concrete moulding, testing the samples and with other aspects of my research. I would like to express my sincere thanks to the departmental personnel, Mr. Dilip Chetri, Mr. Monoj Kumar Baishya, Mr. Mrinal Sarma, Mr. Porag Saikia, Khaklary Dhaneswar, Das Nandan, Mr. Nip Borah, Kalita Amal and Mr. Rituraj Saikia for their help and support during the course of fabrication of the experimental setup and experimentation. I am also thankful to Mr. BVVR Raja for his extended help during the commissioning of the experimental set-up.

I am thankful to my senior lab-mates, Dr. Anbarasu, Dr. Satya Sekhar, and Dr. Niraj Kumar Mishra who helped me at the time of joining the institute. I would like to thank my colleagues, Dr. Hakeem Niyas, Mr. Nithin Narmada, Mr. Sunku Prasad and Mr. Aloke Kumar who helped me to prepare this report to this level. I would like to extend my appreciation to Mr. Vishal Ganore, Mr. Likhendra Prasad, Mr. Vivek Selvan, Mr. Sujit Roy, Mr. Bheem Chowre, Mr. Vigneshwaran, Mr. Viswakarma, Dr. Gyan Sagar Sinha, Dr. Deva Kanta Rabha, Mr. Kiran Naik Bukke, Mr. Gurpreet Singh Sodhi, Mr. Viswanth, Mr. Sureandhar Gunasekaran, Mr.Kamalesh Singh, Mr. Bhuvnesh Garg, Mr. Malleswara Rao, Mr. Bharat, Mr. Abhishek, Mr. Mrinal Bhowmik, Mr. K. Atul , Mr. A.K Shukla, Mr. Manoj Kumar, and Mr. Lav Kumar Kaushik for their constant support and valuable friendship.

I am very glad to take this opportunity to thank some of my friends who helped me in the critical situations. Dr. G.N. Shelke, Dr. D. Anil Kumar, Mr. Vishnu Chowhan and Dr. Simon Peter Mr. Shiva who helped me to collect the financial support in the severe situation of ill health. I also thank Dr. NVV Subba Rao, Dr. Ajay Kumar, Dr. Suresh, Dr. Ramakrishna, Dr. Peetala Ravi, Dr. Pallekonda Ramesh Babu, Dr. H.M. Sateesha, Dr. A.Muthuraja, Dr. Sateesh Veeraswamy, Dr. N.Shanmuga Priya, Dr. Arpan Kumar Mondal, Dr.D.K.Yaduwanshi, Dr. Yadiah, Dr. Johnney Mertens, Dr. R. Kalidasan, Dr. Jai Manik, and Mr. B. Ravi, Mr. PVSS Sridhar, Mr. Srikanth Prasad Mr. Hari Krishna, Mr. S. Satish for their continuous motivation, care and affection shown.

I would like to express my sincere gratitude to my parents, Mr. Babu Rao (Late) and Mrs. Bhagyam, my brothers, Mr. Raja Rao, Mr. Bhaskar Rao (late) and Mr.Vijay Kumar, my sisters Mrs. Baby and Mrs. Syam Sundari and brother-in-laws Mr. Sambasiva Rao, Mr. Ravi Kumar (late), Mr. Khadar, Mr. Kareem and Mother-in-law Mrs. John bee for their great encouragement, love and warm wishes.

I must thank my pleasing children, Bhaskar Babu and Naveen Joel, for always making me smile. Last but not the least, my deepest gratitude goes to my beloved wife, Mrs. Malini for her unlimited sacrifices, great patience, sincere prayers, motivation and continuous support throughout my studies.

I bow my head and record my sincere gratitude to the *Lord Jesus Christ* almighty for giving me the strength, the good health and the spirit of patience to complete my research work.

CHILAKA RAVICHANDRA RAO

Abstract

Energy plays a major role for the existence of mankind. It is necessary to adopt human development and economic growth of any nation with secure, affordable, reliable, clean and sustainable energy supply. Today, the world is facing several challenges such as global warming, depletion of natural resources, population growth, increase in energy demand and price and unequal distribution of energy sources. All these factors contribute to the urgent need to transform the energy sector, which primarily depends on fossil fuels, to the one that uses renewable energies and energy efficient technologies. Renewable energy is one of the key solutions to the current challenges facing by the world. Many countries have already explored various options of generating power from the renewable energy through different approaches.

Concentrated solar power (CSP) is one of the promising large-scale power generation technologies among the renewables, which is being widely commercialized now. The CSP technologies exist in four common forms namely parabolic trough, central tower, and parabolic dish and linear fresnel reflector. The major problem faced by all types of CSP plants is the intermittent solar radiation, which halts the generation of electricity during night and overcast day. This issue can be solved by incorporating a thermal energy storage (TES) system. TES systems are broadly classified into sensible heat storage (SHS), latent heat storage and thermochemical heat storage. TES systems using SHS solid materials are highly attractive due to their high thermal storage capacity, abundant availability, cheap, compatibility with container materials, and chemical stability.

In general, SHS system consists of a regenerator type heat exchanger wherein the heat transfer fluid (HTF) is passed through the storage media for charging and discharging processes. During charging, the high-temperature HTF transfers the heat to the storage medium. The stored energy is released during discharging as the low-temperature HTF passes through it. Design and optimization of SHS prototypes require extensive analysis on heat transfer characteristics between the SHS medium and HTF. The number of HTF tubes and fins on the HTF tube’s outer surface play a major role in transferring the heat between them. Un-optimized prototype with more number of HTF tubes and fins would lead to higher material account. In addition, the overall weight of the system will increase too. Hence, a detailed optimization study is needed to have a cost-effective SHS system. In view of the above, the major objectives of the present work are formulated as

(i) To develop a 3D thermal model for predicting the charging and discharging characteristics of the solid SHS prototype with the optimized number of tubes and fins at different operating conditions

(ii) To test the various mix designs of the concrete mix design to fill inside the designed tube matrix of the SHS beds (M2 and M3)

(iii) To measure thermo-physical properties of the selected concrete mixture samples

(iv) To test the thermal storage performances of the solid SHS prototype at various operating conditions.

A numerical study of conjugate heat transfer in a shell-and-tube type prototype of 15 MJ capacity filled with a SHS material is presented. The materials used in the present study are cast steel and concrete (Mix Design M30 grade). Mix design of M30 grade is a mixture of cement, fine aggregate (sand), coarse aggregate (gravel) and Water in the weight proportion of 1:1.52:3.21:0.49. The governing equations involved in the thermal model are1solved using a finite element based software product, COMSOL^{TM} Multiphysics 4.3a.

The thermo-physical properties of the concrete such as volumetric heat capacity and thermal conductivity were measured with the help of a thermal property analyser, Hot Disk TPS 2500 S by using the transient plane source technique. Two concrete specimens of diameter 25 mm and length 20 mm were prepared for testing the thermo-physical properties at different temperatures. It is observed from the measurements that the thermal conductivity and diffusivity of concrete decrease and the volumetric heat capacity of concrete increases with temperature. The maximum uncertainty in the estimation of thermal conductivity, volumetric heat capacity and diffusivity were ±3 %, ±5% and ±3.5 %, respectively.

Employing optimization configuration of the storage module, three number of lab-scale shell-and-tube based SHS prototypes (i) cast steel prototype (termed as M1), (ii) concrete prototype with copper finned tubes (termed as M2) and (iii) concrete prototype with mild steel finned tubes (termed as M3) of 15 MJ capacity each were fabricated. Five different concrete mix designs were studied and the mix design M30 was selected for thermal storage, as they possess high compressive strength-cost ratio. Charging and discharging characteristics were tested at different operating temperature ranges viz. 343 K – 403 K/353 K – 413 K/363 K – 423 K for M1 prototype and 333 K – 413 K/343 K – 423 K/353 K – 433 K for M2/M3 prototypes during charging and discharging. The storage prototypes were also tested at different velocities of the heat transfer fluid (v = 0.1, 0.25, 0.5 m/s). It is observed that the charging/discharging rate is faster for lower/higher HTF inlet temperature. Similarly, the charging/discharging rate is faster for higher HTF flow velocities. The numerically predicted average bed temperature variation of the storage module is in good agreement with experimental data. It is observed that the charging process is faster than the discharging process due to the domination of preliminary convection heat transfer (during charging) over the preliminary conduction heat transfer (during discharging). For an HTF inlet temperature of 353 / 413 K during charging/discharging and HTF velocity of 0.25 m/s, it took about 1263 / 1803 s, for charging/discharging of the M1 prototype in the experiments. Similarly, it took about 1106 / 1572 s, for charging/discharging in the numerical simulations.

It is observed that partial charging/discharging process is efficient than complete charging/discharging process for the SHS material having less thermal conductivity (concrete ceramic, rock, etc.) They take more time to completely charge/discharge due to lesser heat transfer rate between the SHS materials and the HTF. Hence, partial charging/discharging is better in M2/M3 prototypes and this is addressed using a parameter named, effective charging/discharging time. Effective charging/discharging time is the time taken by the storage prototype's volume average temperature to reach a temperature, which is 5 K lower/higher than the HTF inlet temperature during charging/discharging cycle. Experimentally observed effective charging/discharging time of the M2 and M3 prototypes for the temperature range of 353-433 K are 5210/6297 s and 7160/7780 s and the respective values predicted from the numerical study are 4371/5196 s and 6155/6360 s.

In addition to the major objectives of the thesis, different high temperature lab scale SHS bed configurations are compared numerically. The numerical model used for the performance evaluation of the high temperature SHS beds is slightly modified to study the storage characteristics. Employing concrete, cast steel and cast iron heat storage beds, numerical investigations have been carried out for different geometrical configurations viz., square, circular and hexagonal. The storage volume and heat transfer area of the beds were kept same in thermal modeling for the different configurations. It is found that the cylindrical bed is storing the required heat in less time when compared with other geometries due to the symmetrical heat transfer rates. Simulations have been carried out at the temperature range of 523 K -583 K (cast iron & cast steel) and 523-593 K (concrete) in laminar flow regime. It is also found from the numerical study that the charging time of cast iron (1357 s) and cast steel (1552 s) are much less than that of concrete bed (6183 s) in circular bed designs. Charging time of circular concrete bed (6183 s) is less when compared to its hexagonal (6755 s) and square (6667 s) configurations.

Based on the above discussions, one can conclude that the shell-and-tube based SHS prototype with fins can be effectively used for storing the heat. Further, the results presented in this thesis will be useful for developing the commercial SHS devices for industrial applications. Using the developed thermal model, one can predict the performances of shell-and-tube based SHS prototype with fins filled with different solid SHS materials without performing the expensive experimental studies.

Nomenclature

a : Centre distance between adjacent tubes, (m)

a_m : Latent heat of fusion (J/kg)

a_r : Fraction of reaction

b : Thickness of fins on the charging tubes, (m)

C : Weight of cement per m^3 of concrete, (Kg)

Ca : Weight of coarse aggregate, (Kg)

C_{ap} : Average specific heat of solid SHS material, (J/kg K)

C_{ps} : Specific heat of solid SHS material, (J/kg K)

C_{pf} : Specific heat of liquid or heat transfer fluid, (J/kg K)

$C_{lp,pcm}$: Specific heat of PCM in liquid phase, (J/kg K)

$C_{sp,pcm}$: Specific heat of PCM in solid phase, (J/kg K)

d : Internal diameter of the charging tubes, (m)

D : Diameter of storage bed, (m)

E : Energy stored by chemical reaction, (J)

fa : Weight of fine aggregate, (Kg)

f_{ck} : Characteristic strength, (Mpa)

f'_{ck} : Mean characteristic strength, (Mpa)

h : Height of fins on the charging tubes, (m)

h_m : Enthalpy of fusion, (J/kg)

k_s : Thermal conductivity of solid SHS material, (W/m K)

L : Length of SHS prototype or bed, (m)

m : Mass of storage material (kg)

n : Number of charging tubes

n_{fin} : Number of fins on a charging tube

p : Ratio of fine aggregate to total aggregate

Qs : Heat storage capacity, (J)

S : Standard deviation

S_c : Specific gravities of cement, (Kg/m^3)

S_{fa} : Specific gravities of fine aggregate, (Kg/m^3)

S_{ca} : Specific gravities of coarse aggregate, (Kg/m^3)

t_{ch} : Charging time, (s)

t_{dis} : Discharging time, (s)

T_avg : Volume average temperature $\frac{\int_V T dV}{V}$

T_{ch} : Volume average temperature of SHS bed during charging, (K)

T_{disch} : Volume average temperature of SHS bed during discharging, (K)

T_f : Final temperature, (K)

T_i : Initial temperature, (K)

T_{ini} : Initial temperature of storage system, (K)

T_m : Phase change temperature, (K)

T_{inlet} : HTF inlet temperature, (K)

T_{outlet} : HTF outlet Temperature, (K)

$\vec{v}$: Velocity of HTF, (m/s)

V : Volume of storage material or fresh concrete, (m^3)

V_{min} : Minimum volume of storage material, (m^3)

W : Weight of water per m^3 of concrete, (Kg)

Greek Symbols

ρ : Density (kg/m^3)

μ : Dynamic viscosity of HTF, (Ns/m^2)

γ : Kinematic viscosity of HTF, (m^2/s)

Subscripts

ch : charging

dis : discharging

Ini : Initial

f : Fluid, HTF

s : Solid

Symbols

Δ : Differential operator

Abbreviations

FEM : Finite element method

HTF : Heat transfer fluid

LEC : Levelized electricity cost

MSA : Maximum size of aggregate

PCM : Phase Change Material

SHS : Sensible Heat Storage

STPP : Solar thermal power plant

Contents

List of Figures

List of Tables

Chapter 1

Introduction

1.1 Foreword

Today, the world is facing major challenges such as global warming, depletion of natural resources, population growth, even increasing energy demand, rising energy prices and unequal distribution of energy sources. The global primary energy consumption in 2015 was 5.83×10^{20} J, equal to an average power consumption of 18.5 TW (Perez M and R, 2015). Majority of the world's energy demand is fulfilled by the non-renewable energy sources, which occupies a share of 80.8 % (Sawin JL et al., 2016). Depending on the non-renewable energy sources at the same proportion for another century, will results in depletion of the natural resources. All these factors contribute to the immediate need to transform the energy sector, which primarily depends on fossil fuels, to one that uses renewable energies and energy efficient technologies. Renewable energy is one of the key solutions to the current challenges facing by the world. Many countries (Spain, US, France, Italy, Israel and Germany etc.) have already started harvesting the various forms of renewable energy sources.

Solar energy is the most sustainable alternative energy source for producing electricity to meet the future energy demand. As illustrated in Fig. 1.1., the potential of solar energy is much higher than other renewable energy resources. It can be observed from Fig. 1.1 that the solar energy is the best available renewable energy source in terms of energy potential. Other than fossil fuels, nuclear, large hydro-power wind energy, bio-mass, tidal energy and geothermal energy are the other sources which can contribute in a small way to meet the world's present energy demand.

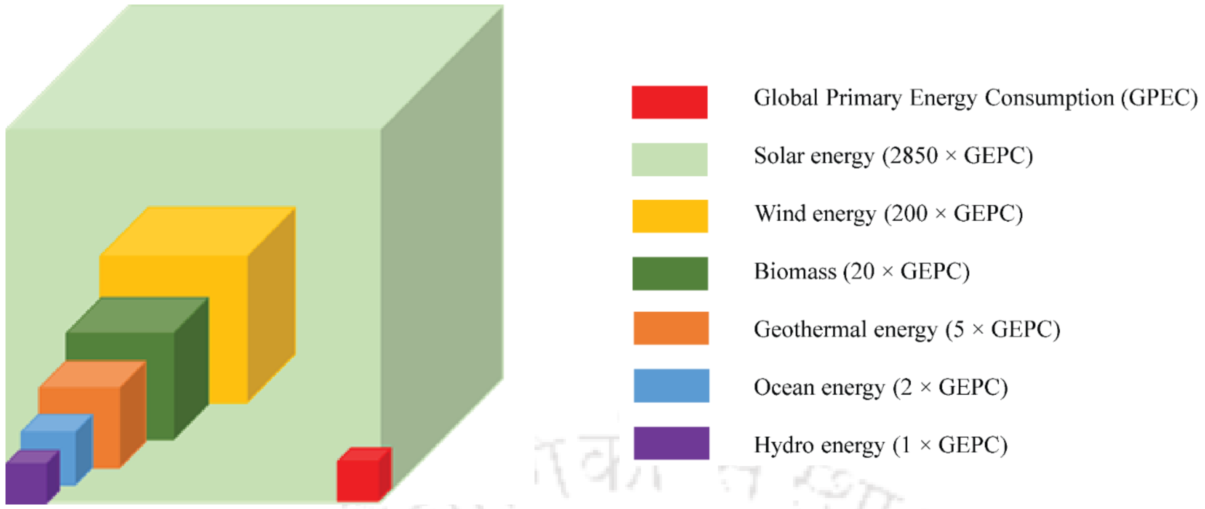

Fig.1. 1 Natural availability and technical global potentials of renewable energies (Muller-Steinhagen and Nitsch, 2005)

Traditionally, solar energy is used for space heating, water heating, cooling, air-conditioning and food drying applications. But, nowadays it has also evolved as an integral part of electric power generation unit. The schematic representation of various types of solar power generation methods are shown in Fig. 1.2.

Solar energy can be converted to electricity directly using photovoltaic (PV) cells, or indirectly using concentrated solar power (CSP) devices. Photovoltaic converts the sunlight into electric current using the photovoltaic effect. CSP plants use reflective lenses or mirrors and tracking systems to focus a large amount of sunlight on to a boiler located as the concentration point or focal point of the concentrated solar collector, the high concentration ratio generates huge heat that heats the working fluid to a higher temperature. In direct steam generation (DSG) parabolic trough power plants, the working fluid is generally water, and the steam produced is directly fed to the turbine for electricity generation. In non-DSG plants, the primary working fluid is generally a synthetic oil that receives heat from the concentrated sunlight. Synthetic oil transfers the heat to the secondary working fluid (water/steam), which is then supplied to the turbine for power generation. The major disadvantage with the PV and CSP plants is the inability to generate electricity during night and overcast day, which reduces the operating time. These demanding issues can be in-line by incorporating thermal energy storage (TES) that operate synergistically in CSP plants. Dincer I and M., 2002; Hasnain, (1998); Kuravi et al., (2013), discussed in detail about the various aspects of TES technologies and their applications for CSP plants. Though several prototypes of TES were developed across the world, only a few large-scale TES systems have been commissioned in the CSP plants (Gil et al., 2010).

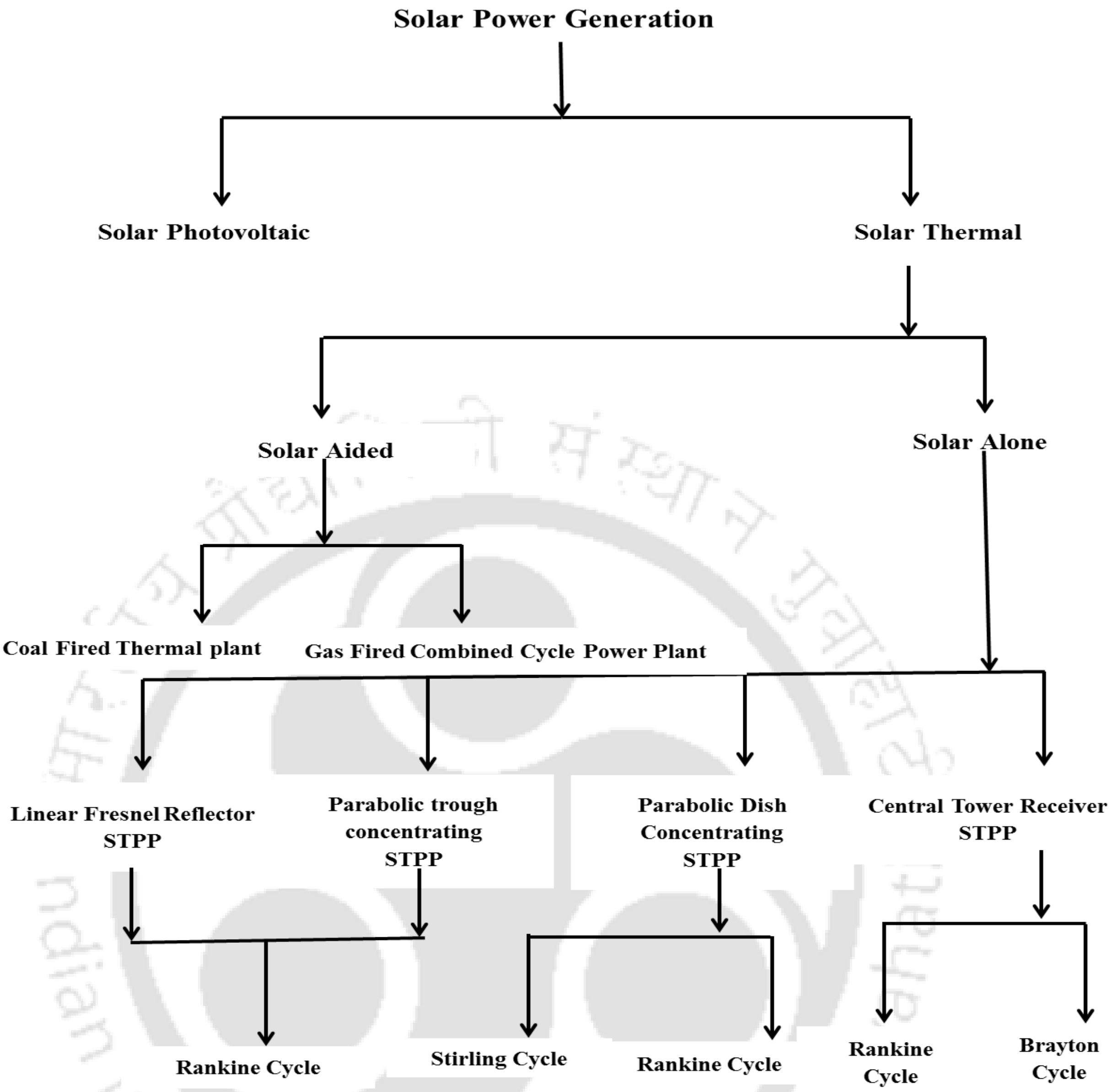

Fig.1. 2 Schematic view of solar power generation methods (Reddy et al., 2013)

1.2 Thermal energy storage system

A plant which generates power solely by solar concentrated power is called as Solar Thermal Power Plant (STPP). The major elements that obstruct the development of STPP are – intermittence of solar energy, high cost of the operating devices and low efficiency. Since the availability of solar energy is free and unlimited, the limitation possessed by the high cost of the solar devices and low system efficiency can be stabled with the advancement in mass production technology. Thus, the fluctuating and irregular solar intensity throughout the day and year is only the key issue for solar-based thermal applications. Overcoming this barrier is the main focus of several researchers for many years. Hence, it compelled the development of TES system which is necessary to ensure the STPP's reliability and effectiveness (Tamme et al., 2004).

The major elements of the STPP are: receiver, concentrator, power conversion device and TES system (Laing et al., 2010). The TES system bridges the gap between the energy supply and demand in STPP by storing the energy during the low energy demand and deliver it to a later period, when there is high energy demand (Cabeza, 2012; Dincer I and M., 2002; Mehling and Cabeza, 2010). Also, the TES systems help in the integration of STPPs into the power grids, which finally smoothen out the fluctuations in the supply of electricity. Mainly, the TES system consists of a regenerator type heat exchanger wherein the heat transfer fluid (HTF) passes through the storage media during the charging/ discharging processes. During charging, the high temperature HTF transfers the heat to the storage medium. The stored heat energy is released from the TES system during discharging as the low-temperature HTF passes through it. Fig.1.3, shows the schematic of a STPP incorporated with the TES system.

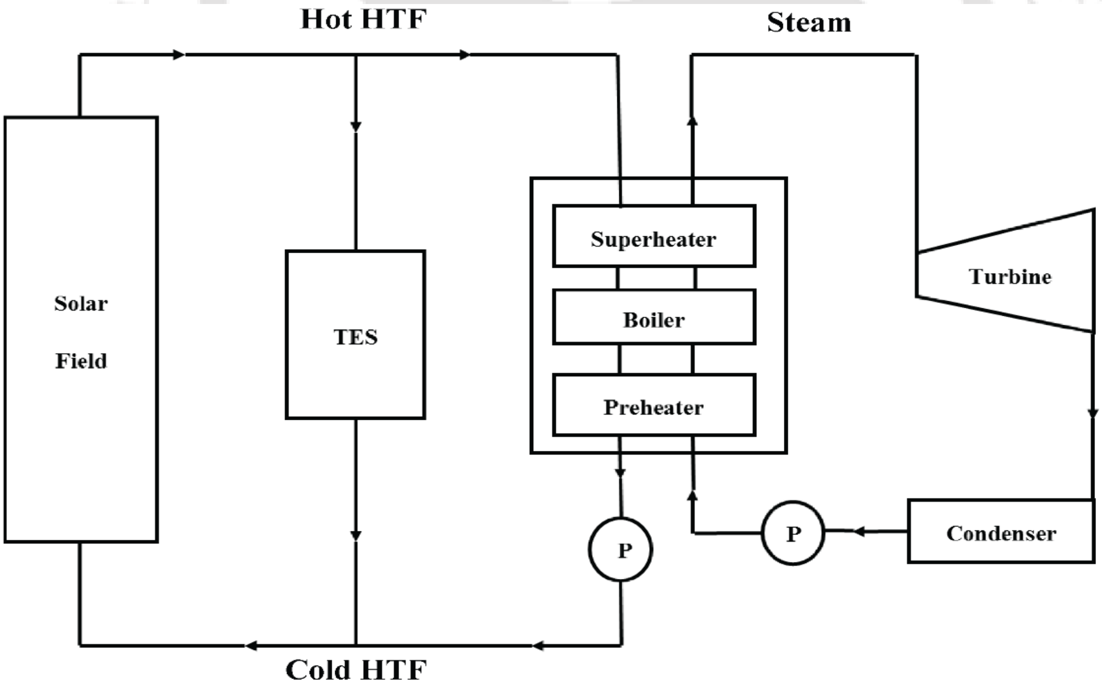

Fig.1. 3 Schematic of STPP with TES system

TES system can be integrated with STPP in the following ways;

(i) Storage charging only

(ii) Steam generation and storage charging

(iii) Steam generation from storage discharge only

(iv) Steam generation from solar field and storage discharge.

In the first case, the hot HTF from the solar field is allowed to pass through the TES system and then recirculated to the solar field itself. In the second case, excess thermal energy that is not used to generate steam is stored. The HTF flows from solar field to both heat exchangers of steam generator and TES in parallel and flow back to the pumping station. The third one applies when there is no solar field output and steam is required. The HTF runs in loop between storage heat exchanger and steam generator. The last one is related to a situation, when there is solar field output, but it is desirable to supplement that output with energy from storage. The HTF flows from solar field and storage heat exchanger (both solar field and storage heat exchanger act in parallel) to the process steam generation unit and from there, flows back to the pumping station.

1.3 Thermal energy storage systems in CSP plants

Many plants under construction or planned to generate electricity in large scale require a TES system large enough for continuous production during periods of low solar intensity. Sensible storage is the dominant TES technology used in CSP plants. Fig. 1.4 shows the percentage of CSP plants implementing the TES system.

About half of the plants (47%) currently in operation integrated with a TES system. There is a notable increase in the use of TES systems for plants under construction (72%) and planned (77%). This increase can be partially explained by the technological progress and advancements achieved in storage systems and the necessity to install such systems to be economically competitive (Pelay et al., 2017).

1.4 Thermal energy storage concepts

Fig. 1.5 depicts the various storage concepts available in the TES systems. The storage concept (shown in Fig.1.3) decides the fluids flow passage. Depending upon the role played by the storage medium, storage concept can be mainly a type of active or passive storage system. In active storage system, storage material itself circulates through a heat exchanger and this heat exchanger can be a solar receiver or a steam generator (Gil et al., 2010). Generally, the active storage system uses one tank thermocline system (Yang and Garimella, 2010a) or two massive storage tanks containing the corresponding storage material.

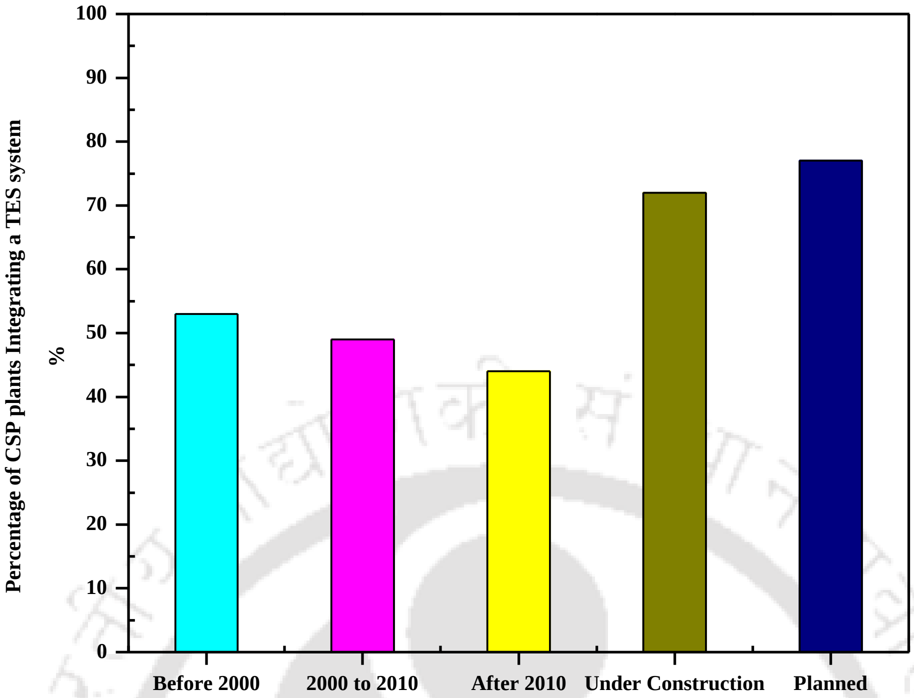

Fig.1. 4 Presence of TES system in CSP plants (Pelay et al., 2017)

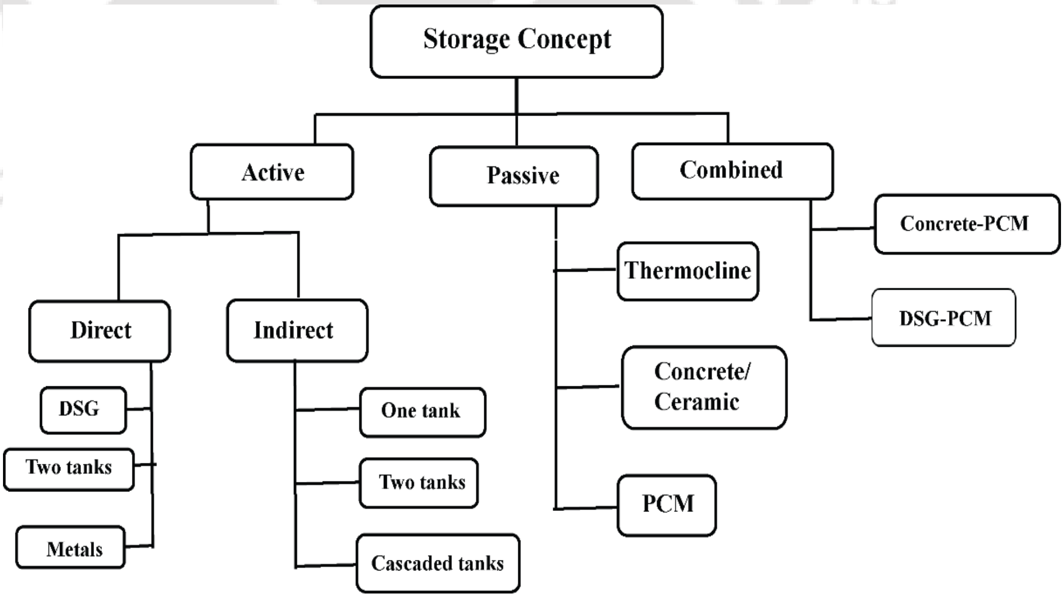

Fig.1. 5 Storage concepts of TES system

Active storage system is further classified into direct and indirect systems. In active direct system, the storage material acts as the HTF also, while in active indirect system, a secondary fluid such as oil is used to extract the energy from the storage material. Hence, the cost of the indirect storage system is comparatively more due to the additional heat exchanger.

Passive storage system consists of a regenerator type heat exchanger in which the HTF is passed through the storage media during the charging and discharging processes. During the charging process, the high temperature HTF transfers the heat to the storage medium. This stored heat is released back to the HTF during the discharging process when the low temperature HTF is passed through it. Usually the materials are mainly solid storage substances (i.e. concrete or PCMs). The advantages of solid concrete are the very low cost of thermal energy stored, with facility to handle the material and low degradation of its properties (Gil et al., 2010; Kuravi et al., 2013). Integration of various TES system concepts in the CSP plants can be seen in Fig.1.6 (a-d). Table 1.1 summaries the various merits and demerits of the main thermal energy storage concepts: active and passive heat storage systems.

(a)

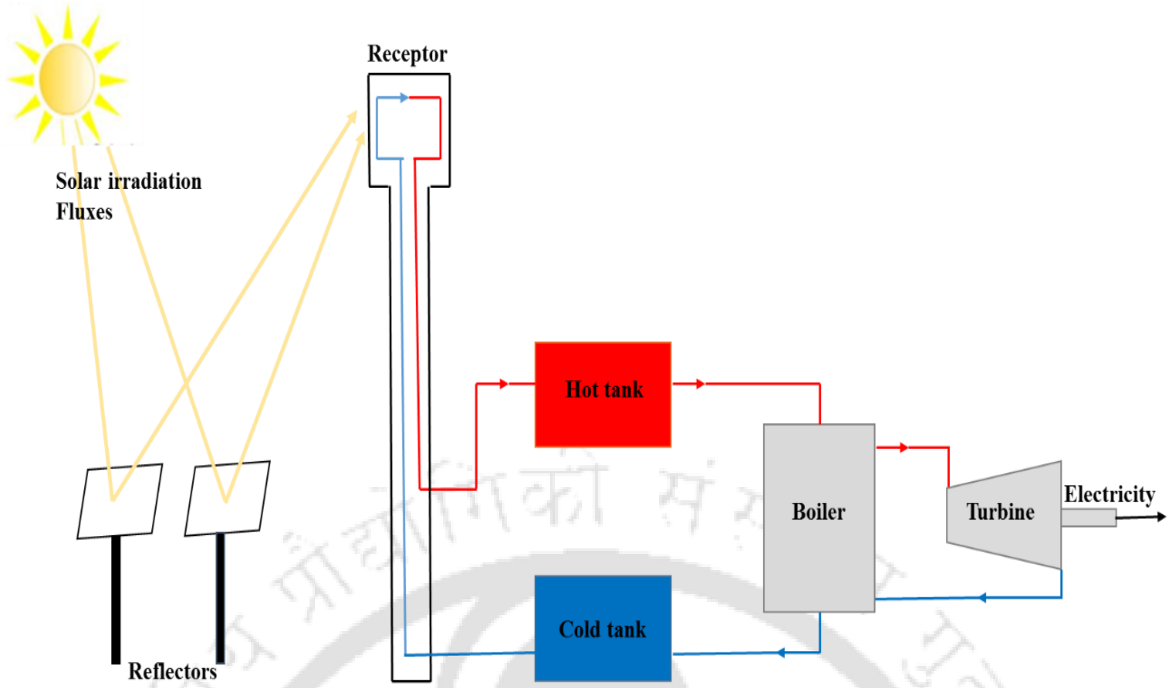
Receptor
Solar irradiation
Fluxes
Hot tank
Boiler
Turbine
Electricity
Cold tank
Reflectors

(b)

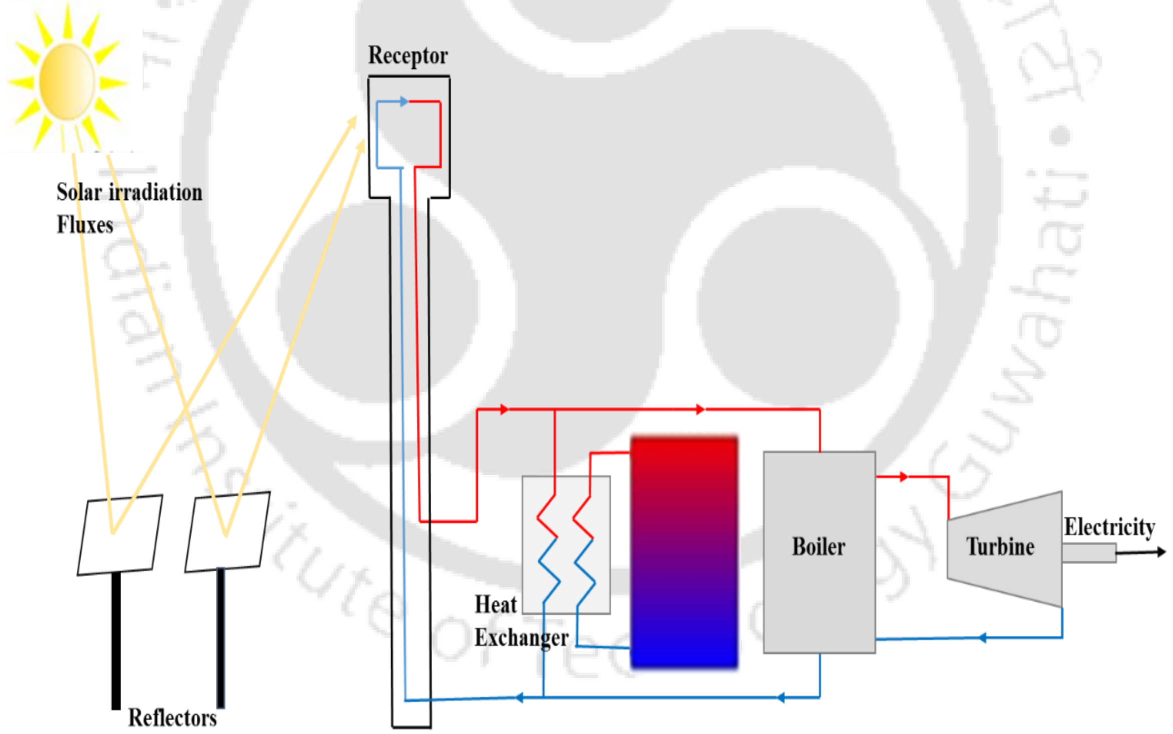
Receptor
Solar irradiation
Fluxes
Boiler
Turbine
Electricity
Heat
Exchanger
Reflectors

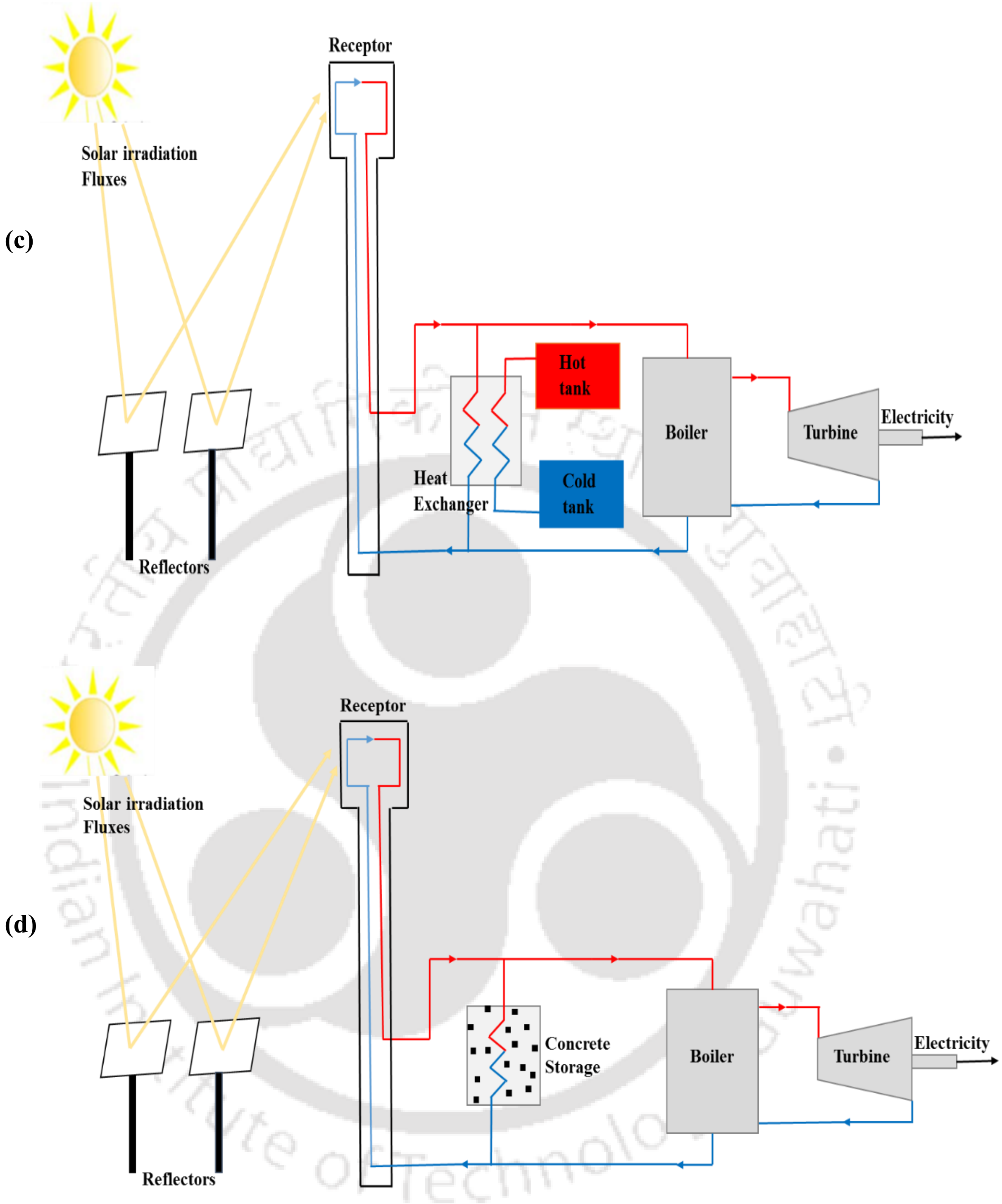

Fig.1. 6 TES integration by (a) active direct concept, (b) active indirect concept-single tank, (c) active indirect concept-two tanks and (d) passive concept (Alva et al., 2018).

Table 1. 1 Merits and demerits of active and passive storage systems (Medrano et al., 2010).

Storage System & Concept	Merits	Demerits
Active Direct Storage System – Direct steam generation	• Intermediate HTF and steam generation exchanger is not necessary, improving the efficiency loss in steam generation. • Overall plant configuration is simple. • Lower investment and operation and Maintenance cost. • Solar field can be operated at higher temperatures, increasing the power cycle efficiency (Reduction of LEC).	• Increase of pipe installation cost (is necessary to work at very high pressures). • Need of auxiliary protective heating systems for start-up, maintenance and recover from frozen conditions. • Instability of the two phase flow inside the receiver tubes (procedures for filling and draining). • Difficult to control the solar field under solar radiation transients.
Active Direct Storage System – Two tanks	• Cold and hot HTF are stored separately. • Low-risk process. • Solar field output temperature can be raised to 450/500 °C (in trough plants) and thereby the Rankine cycle efficiency of the power block steam turbine will be achieved up to 40%.	• Very high cost of the material used as HTF and TES. • Heat exchanger and two tanks are expensive as they are very large in size. • Relatively small temperature gradient between the hot and cold fluid in the storage system.

	• The HTF temperature rise in the collector field can increase up to a factor of 2.5, thereby reducing the physical size of the TES.	• High risk of solidification of storage fluid, due to its relatively high freeze point which in turn increases the maintenance and operational costs. • The high temperature of both tanks pushes to an increase of losses in the solar field. • The lowest cost TES design does not correspond to the lowest cost of electricity.
Active Indirect Storage System – Two tanks	• Cold and hot HTF are stored separately. • Also low-risk process. • The HTF temperature rise in the collector field can reduce the physical size of the TES. • TES material flows only between hot and cold tanks, not through the parabolic troughs (decreases the risk of solidification of salts).	• Very high cost of the TES material. • Heat Exchanger between the HTF and TES material is needed. • Heat exchanger and two tanks are expensive as they are very large in size. • Relatively small temperature gradient between the hot and cold fluid in the storage system. • The high temperature of both tanks causes to increase the heat losses in the solar field. • Efficiency is decreased when compared with two tanks direct system.

Active Indirect Storage System – Cascaded tanks	• Higher utilization of PCM-storage capacities. • More uniform outlet temperature over time.	• Heavy increase of cost, due to a higher number of: storage tanks, HTF loops and PCM. • Further PCM need to be identified which also offer a sufficient heat of fusion and a satisfying corrosiveness. • No real experiences as of now, only simulation.
Active Indirect Storage System – Single tank thermocline	• Decrease of storage tanks cost, as it uses only one tank. • Low cost of the filler materials (rocks and sand). • In cost comparisons, the thermocline system is about 35% cheaper than the two-tank storage system, due to reduction of storage volume and elimination of one tank.	• Relatively high freeze point of most molten salts formulations (is necessary to maintain a minimum system temperature to avoid freezing and salt dissociation). • More difficult to separate the hot and cold HTF. • The high outlet temperature causes to increase the heat loss in the solar field. • Maintaining of thermal stratification requires a controlled charging and discharging procedure, and appropriate methods or devices to avoid mixing. • Design of storage system is complicated • Thermodynamically it was an inefficient power plant

		• This system is riskier w.r.t the performance
Passive storage system – concrete/ceramics	• Very low cost of thermal energy storage media, due mainly to the filler cost. • High heat transfer rates into and out of the solid medium (due to a good contact between the concrete and piping). • Facility to handling of the material. • Low degradation of heat transfer between the heat exchanger and the storage material.	• Increase of cost of heat exchanger and of engineering. • Long-term instability.
Passive storage system – PCM – Sensible – PCM	• Increasing of storage capacity. • Better use of PCM-storage capacities. • Cost is reduced when compared with storage systems of only PCM as storage media. • Storage ratio is improved when compared with systems of only SHS materials.	• Necessary to develop technologies to analyse this concept.

1.5 Classifications of Thermal Energy Storage System

The major TES methods that are available currently can be classified as

(i) Sensible heat
(ii) Latent heat and
(iii) Thermochemical heat storage.

The first two are being the most widely used TES systems. A schematic of storage methods of solar thermal energy is shown in Fig. 1.7.

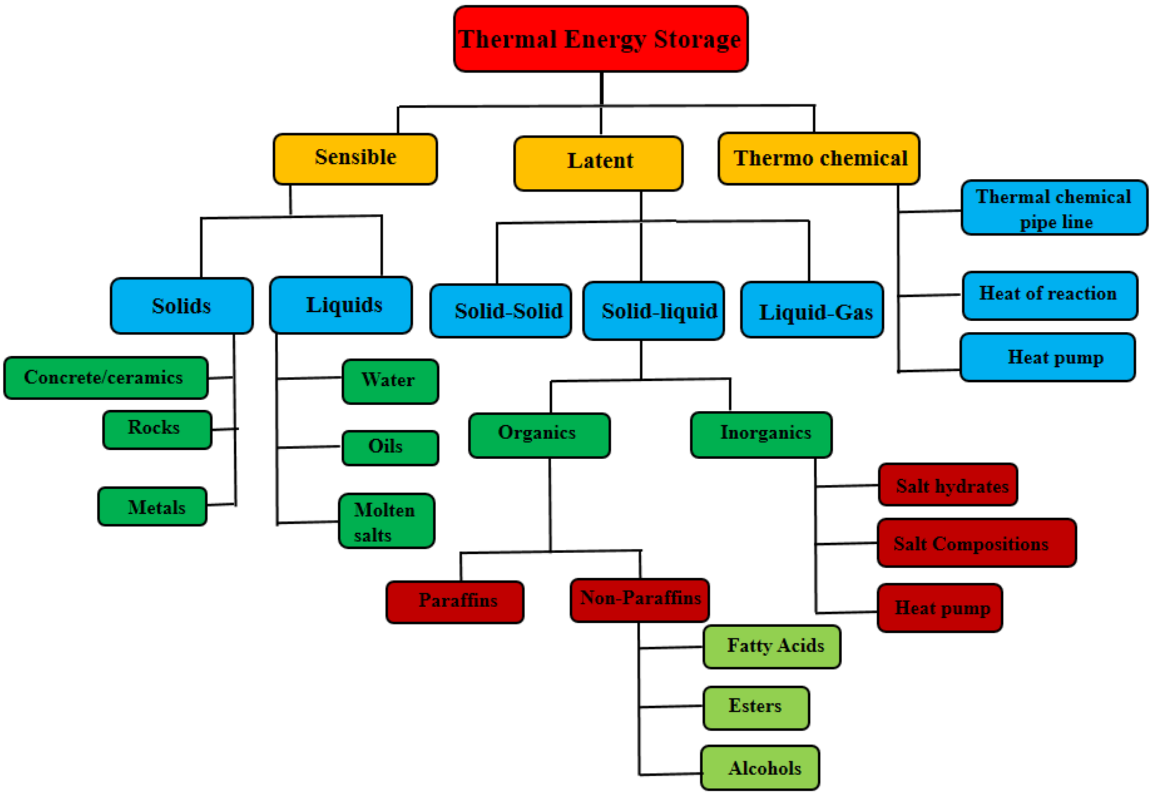

Fig.1. 7 Overview of thermal energy storage systems

1.5.1 Sensible heat storage

In sensible heat storage (SHS), thermal energy is accumulated in the storage material by raising the temperature of the storage medium. Sensible storage utilizes the heat capacity of storage material to store thermal energy.

The parameters like heat storage capacity and temperature range determine the size and suitability of the storage system respectively. For a given quantity of energy to store at prescribed temperature gradient, material with higher specific heat requires less mass of storage material. The thermal energy stored by sensible heat storage material is given by the following equation 1.1.

$$Q=\int_{T_i}^{T_f} mC_p\,dT = mC_{ap}(T_f - T_i) \qquad (J) \tag{1.1}$$

Sensible energy can be stored in both solids and liquids. The commonly used solid based SHS materials are cast steel, brick, rock, sand, concrete and ceramic. The liquid based SHS materials include oils (synthetic, mineral and silicon), molten salts and water. A detailed explanation on the classification of SHS materials is given in the section 1.6. The major problem with the liquid storage system is that it requires bulky storage tanks and expensive heat exchangers. Oro et al., (2012) reported that the two tanks storage system utilizes a huge amount of storage materials thereby leaves the highest environmental impression and hence, better alternatives should be adopted to minimize the storage material and heat exchanger cost. Although one tank can be eliminated by using the thermocline system, freezing of liquid materials (mostly salts) at high temperature is still a problem. Free and abundant liquid water can be utilized as SHS material for the applications where low temperature storage systems are needed. But, for high temperatures (> 100 °C), expensive pressure equipment is essential to increase the pressure of steam to avoid condensation. Liquids such as synthetic oil cannot be used as a storage material at high temperatures because of its high vapor pressure (Yang and Garimella, 2010b). However, it can be employed as the heat transfer fluid (HTF), due to its better heat transfer characteristics.

1.5.2 Latent heat storage

In latent heat storage (LHS), thermal energy is stored by phase change of a material e.g. solid to liquid or liquid to vapour or solid to solid. Utilizing the latent heat of fusion (i.e. solid to liquid) is a known method as it fulfils the maximum requisite properties. In solid-solid transition heat is stored as the material is transformed from one crystalline to another. This transition has smaller latent heat and volume change than solid–liquid transition.

Comparatively higher latent heat is associated with liquid-vapour transition, but change of phase causes drastic volume change which rule out their use in TES systems. LHS is particularly attractive due to its ability to provide higher storage density and achieve energy storage/retrieval at a near constant temperature.

The major difficulties with PCM are their degradation with thermal cycling especially at high temperature and very low conductivity which slows down the charging and discharging rates. They also require a special attention to be paid to enhance their heat transfer characteristics. The total energy stored in the material during charging cycle is given as

$$Q = \int_{T_i}^{T_m} m C_{sp,pcm}\, dT + m a_m \Delta h_m + \int_{T_m}^{Tf} m C_{lp,pcm}\, dT \quad (J) \qquad 1.2$$

$$Q = m\left[C_{sp,pcm} \left(T_m - T_i\right) + a_m \Delta h_m + C_{lp,pcm}\left(T_f - T_m\right)\right] \quad (J) \qquad 1.3$$

1.5.3 Thermochemical heat storage

Thermo chemical storage systems (TCHS) rely on the energy absorbed and released in breaking and reforming molecular bonds in a completely reversible chemical reaction. In this case, the thermal energy storage depends on the amount of storage material (m), the endothermic heat of reaction (Δh_r) and the extent of conversion– fraction reacted (a_r), and the energy stored is given by Eq. 1.4. For long term storage, chemical TES is a feasible option but technological complexity and high costs limit their use.

$$E = m \Delta h_r\, a_r \quad (J) \qquad 1.4$$

Amongst above thermal energy storage techniques, sensible heat thermal energy storage is particularly attractive due to its low economic provision, reliable and easy maintenance to power production at a reduced cost per unit.

1.6 Sensible heat storage materials

SHS materials are a group of materials that undergo no phase change within the temperature range of the energy storage/retrieval process (Fernandez et al., 2010). The desirable properties of SHS materials for high temperature storage applications are (Khare et al., 2013);

- Thermo-physical properties: High energy density, high thermal conductivity, high heat capacity, high density and long term thermal cycling stability.
- Chemical properties: Long term chemical stability with no chemical decomposition, non-toxic, non-explosive, low corrosion potential or reactivity to HTFs, and compatible with materials of construction.

- Economic properties: Cheap and abundant materials with low cost of manufacturing into suitable shapes.
- Mechanical properties: Good mechanical stability, low coefficient of thermal expansion, high fracture toughness, high compressive strength.
- Environmental properties: Low manufacturing energy requirement and CO_2 foot print.

The amount of energy stored in a SHS material should be more in order to make it an economically feasible option. For a given volume, to store more amount of heat, the material should have higher heat capacity. But, a material with more heat capacity does not guarantee the best thermal storage performance (Mawire et al., 2009). The properties such as density and thermal conductivity are also equally important for achieving better performance. In general, higher heat capacity decreases the SHS volume and higher thermal conductivity improves the heat transfer dynamics of the storage prototype (Laing et al., 2006).

Based on the temperature range, the SHS materials are sub-divided into

(i) Low temperature SHS
(ii) Intermediate and
(iii) High temperature SHS materials.

The low temperature storage range is defined in the temperature less than 100 °C. Water is the most potential low temperature storage liquid with high thermal conductivity and can be stored at atmospheric pressure in that temperature range. It is advantageous when the collector fluid in the solar energy system is water due to its high specific heat values. However, it is corrosive to some materials and the lifetime of water tanks is only about 10 years. The intermediate temperature storage range is defined as between 100 °C and 500 °C. Materials in this range are suitable to be coupled with concentrating solar energy collectors. Unpressurized organic liquids (oils) used for intermediate temperature range. Temperatures higher than 500 °C is in the high temperature range. Molten salts and liquid metals are candidate SHS materials for the high temperature range. It is possible to store energy at elevated temperatures as sensible heat in solids. Heat can be stored at temperatures from low to high (up to 800 °C) in sand, rocks, high temperature concrete, ceramics, cast iron, cast steel, aluminum, aluminum oxide, magnesium oxide, and granite (Hasnain, 1998). However, the problem is the material of the fluid pipe should be the same as that of the storage medium, since contact separation might occur between them as a result of different expansion coefficients.

A list of the most common solid and liquid SHS materials along with their properties is given in Tables 1.2 and 1.3 respectively. Within the indicated solids, concrete and cast ceramics have been extensively studied due to their low costs, good thermal conductivities and moderate specific heats. In liquids storage materials, molten salts are widely used in power tower. Since they are non-flammable and non-toxic and their operating temperatures are compatible with current high-pressure and high temperature turbines (120 °C–600 °C). These molten salts are already used in the chemical and metallurgical industries as HTF. From Tab.1.3, it is clear that the main candidate for liquid SHS is a solar salt, i.e. a binary salt (60% of $NaNO_3$ and 40% of KNO_3) that melts at 221 °C.

SHS materials have been widely studied and are currently applied in CSP applications. Most of the molten salts have a high freezing point (around 100 °C), and the high outlet temperature results in heat losses and require more expensive piping and materials. This high freezing point is a problem for solar power plants because of the required heat trace during non-functioning periods.

Another important disadvantage is the low energy storage density of sensible heat materials, which demand large volumes or quantities in order to deliver the amount of energy storage necessary for high temperature TES applications (Fernandes et al., 2012).

Table 1. 2 Main characteristics and SHS solid materials for solar power plant TES applications (Fernandes et al., 2012).

Storage Medium	**Temperature**		**λ**	**C_p**	**ρ**	**Cost**
	Cold (°C)	**Hot (°C)**	**(W/m K)**	**(J/kg K)**	**(kg/m³)**	**(€/kg)**
Sand-rock-mineral oil	200	300	1	1300	1700	0.12
Reinforced Concrete	200	400	1.5	850	2200	0.036
Nacl (solid)	200	500	7	850	2160	0.12
Cast iron	200	400	37	560	7200	0.724
Cast steel	200	700	40	600	7800	-
Silica fire Bricks	200	700	1.5	1000	1820	0.724
Magnesia fire Bricks	200	1200	1	1150	3000	1.45

Table 1. 3 Main characteristics and SHS liquid materials for solar power plant TES applications (Fernandes et al., 2012; Garg et al., 1985).

Storage Medium	**Temperature Cold (°C)**	**Hot (°C)**	**λ (W/m K)**	**C_p (J/kg K)**	**ρ (kg/m³)**	**Cost (€/kg)**
HITEC Molten Salt	142	540	0.61	1560	1680	-
Mineral oil	200	300	0.12	2600	770	0.217
Synthetic Oil	250	350	0.11	2300	900	2.173
Silicon Oil	300	400	0.1	2100	900	3.622
Nitrite salts	250	450	0.57	1500	1825	0.724
Nitrate salts	265	565	0.52	1600	1870	0.362
Carbonate salts	450	850	2	1800	2100	1.739
Liquid sodium	270	530	71	1300	850	1.449

The classification of sensible TES systems based on long term storage is given in Fig. 1.8. Basically, sensible TES consists of a storage medium, a container, and input/output devices. In thermally stratified TES tanks a well-designed positions of the inlet and outlet is to be required. Since the tank stores thermal energy for several hours, heat loss/gain occurs from the tank. The thermal-retaining performance of a tank is an important factor in its design. Rock is a good sensible TES material from the economic point of view, but its volumetric thermal capacity is only half of that of water.

1.6.1 Cast iron and Cast steel storage materials

Some metallic solid materials, such as cast iron and cast steel, have been considered or used for TES purposes due to their good thermo-physical properties (Fernandes et al., 2012; Garg et al., 1985). The key parameter of these materials for thermal energy storage is the product of density and heat capacity (ρ×C), as well as thermal conductivity. While the former determines the volumetric energy storage capacity, the latter is important to the TES efficiency. High thermal conductivity will result in less exergy loss due to the heat transfer processes in the heat charging and discharging processes. These materials are more advantageous where there is a need for thermal stability, less thermal degradation and higher number of thermal cycles. Similarly, they are preferred where cost and availability is the prime criteria.

1.7 Storage system geometrical configuration and heat exchanger design

The geometrical configurations of TES system/tank have a huge impact on the performance parameters of the system like heat transfer rate, charging and discharging time, the temperature distribution of the materials in the system, heat exchanger characteristics of the system and quantity of TES materials etc. (Mao, 2016). Currently employed geometrical configurations of the storage system are cylinder and rectangle configurations. Recently, other geometrical configurations of the storage system, i.e., multi-materials/multi-tanks, helical tube, and vertical wavy enclosure have also been designed and studied. It is obvious that there are different heat transfer characteristics for different shapes. Figure 1.9 shows two typical TES systems/tanks in CSP plant with cylindrical and rectangular shapes.

In order to obtain lower cost and higher efficiency of the power plant, the optimization of the geometrical configuration of TES tank is very necessary. Once the storage material is selected primarily based on the temperature range of the application, the subsequent vital factors to consider are the arrangement of the HTF tubes and the optimum sizing of the tube and heat exchanger required for a given amount of the storage material. All these factors have a direct influence on the storage characteristics of the storage material and eventually affects the charging and discharging rates of the SHS unit.

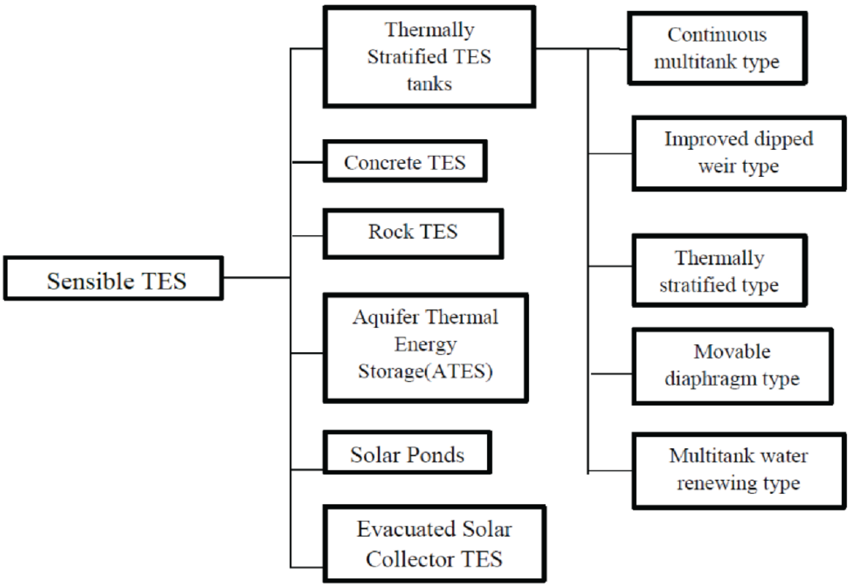

Fig.1. 8 Classification of sensible TES systems

To ensure long-term thermal performance of any SHS unit, the size and shape of the unit must be carefully selected. The most intensely analysed configuration is the shell-and-tube TES system. Also, the heat loss from the shell-and-tube system is minimal (Kuravi et al., 2013). Because of its high efficiency and relatively smaller volume, the shell-and-tube heat storage unit is widely used in TES systems. In the shell-and-tube TES system, the storage material fills the annular shell space around the tube, while the HTF flows through the tubes. Higher/lower heat capacity HTF such as thermic oil/air is generally passed through the tubes and exchanges heat with the storage material (Mao, 2016). Also, finned tube-in-shell cylinder storage tank is the main trend to optimize the heat transfer performance. In a solid media storage, the heat exchanger for the HTF is embedded in a solid matrix (Tamme et al., 2004).

The thermo-physical properties of the solid storage materials are of great relevance. High cycling stability is important for a long lifetime of the storage. Embedded structures used for improving heat transfer have been studied by many researchers at both low temperature and high temperature ranges. However, if high thermal conductivity materials are used, they must be compatible with both the storage material and HTF. For high temperature sensible heat storage, concrete system with an integrated tubular heat exchanger have been investigated by Tamme et al., (2004). A tubular heat exchanger is integrated into the storage material for efficient heat transfer. The heat exchanger demands a significant share of the investment costs. The feasibility of using different fin materials was studied by Steinmann et al., (2009).

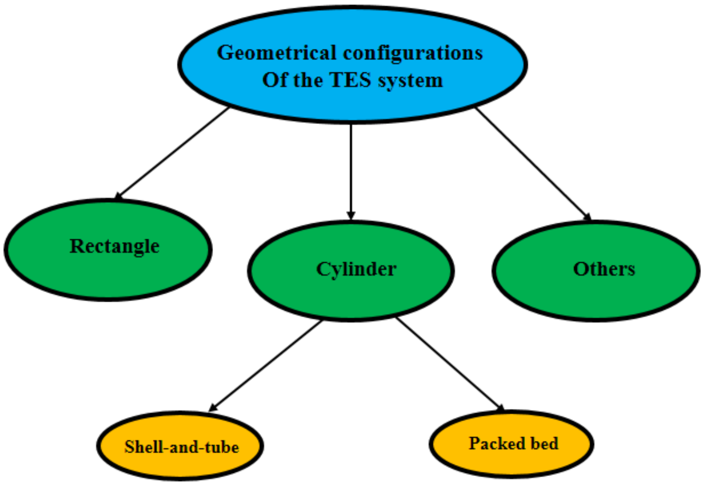

Fig.1. 9 Classification of TES system geometrical configuration (Mao, 2016).

1.8 Concrete Thermal Energy Storage

Concrete is more suitable for TES application due to its low cost, availability throughout the world, and easy construction. Concrete has the following characteristics as a storage medium:

- High specific heat;
- Good mechanical properties (e.g., compressive strength);
- Thermal expansion coefficient near that of steel (pipe material); and
- High mechanical resistance to cyclic thermal loading.
- Non-toxic and non-flammable.

Since, concrete possesses good mechanical strength, it does not require a container to hold. Especially at higher working temperatures, the modular structure with optimized operation strategies make the heat storage in concrete attractive (Jian et al., 2015; Laing et al., 2008; Tamme et al., 2004). Concrete is a mixture of cement, gravel and sand. Gravels have the mineral composition of the type of rock. Sand is mostly quartz mineral which is 90% silica (SiO_2). Cement acts as the binder. Portland cement's main constituents before use in concrete mix are CaO (≈63%), SiO_2 (≈19%), Al2O3 (≈6%), etc. During the curing process cement undergoes hydration and forms cement phases like calcium silicate hydrate (C – S – H), calcium alumina silicate hydrate (C – A – S – H), Portlandite ($Ca(OH)_2$) etc. (Alva et al., 2018).

When concrete is heated, a number of transformations and reactions take place which influence its strength and other physical properties. On heating to about 100 °C, water is expelled (up to 130 kg of water per m^3 of concrete). The remaining water (50 to 60 kg of water per m^3 concrete), either physically bound in smaller pores or held by chemisorption, is expelled as temperatures rise from 120 °C to 600 °C. Most dehydration occurs between 30 and 300 °C. This water loss reduces the weight of concrete by 2 to 4%. The specific heat decreases in the temperature range between 20 and 120 °C, and the thermal conductivity decreases from 20 °C and 280 °C. The mechanical properties are also slightly influenced by the loss of water; compressive strength decreases by about 20% at 400 °C. Resistance to thermal cycling depends on the thermal expansion coefficient of the materials used in the concrete. To minimize such problems, a basalt concrete is used. Steel needles and reinforcement are added to the concrete to obstruct cracking and so thermal conductivity is increased by about 15% at 100 °C and 10% at 250 °C (Dinter et al., 1990).

1.9 Current Solar Thermal Power Generation and Energy Storage Status

Till date, globally about 91 solar thermal power plants have been installed. Additionally, 65 plants are under commissioning, which makes it a total sum of 156 power plants. Majority of the power plants are based on parabolic trough technology (99 plants) followed by power tower (40 plants) and linear Fresnel reflector (LFR – 17 plants). In storage perspective, less than half number of these plants have been incorporated with certain storage systems. Molten salt two tank indirect storage systems were adopted in 45 power plants, despite of the high cost of TES material due to its comparatively lesser cost than two tank direct storage system.

Table. 1.4 provides the information on the power technology, electricity generation capacity and storage system of solar thermal power plants. It is seen from Table. 1.4 that there is no solar power plants implemented with passive high temperature storage systems. This necessitates the importance of research on passive high temperature storage systems such as concrete and PCM or combined systems.

Table1. 4 Solar thermal power plants – Generation and Storage (www.nrel.gov)

Sl. No.	Project Name	Country	CSP Technology/ Storage Concept	Capacity (MWe)	Key features (HTF/Storage/ Field Area-m^2/ Storage time)
1	Aalborg CSP	Denmark	Trough/–	16.6	– – 26,929 –
2	Abhijeet Solar Project	India	Trough/–	50	Therminol VP-1 – – –
3	ACME Solar Tower	India	Tower/–	2.5	Water/steam – 16,222 –
4	Agua Prieta II	Mexico	Trough/–	12	Thermal Oil – 85,000 –
5	Air light Energy Ait-Baha	Morocco	Trough/ Other	3	Air Rocks 2,053 5 hrs.
6	Alba Nova 1	France	LFR/ Other	12	Water – 1,40,000 1 hr.
7	Andasol-1 (AS-1)	Spain	Trough/ 2-tank indirect	49.9	Downtherm A Molten salt 5,10,150 7.5 hrs.
8	Andasol-2 (AS-2)	Spain	Trough/ 2-tank indirect	49.9	Downtherm A Molten salt 5,10,150 7.5 hrs.
9	Andasol-3 (AS-3)	Spain	Trough/ 2-tank indirect	50	Thermal Oil Molten salt 5,10,150 7.5 hrs.
10	Archimede	Italy	Trough/ 2-tank direct	4.72	Molten salt Molten salt 31,860 8 hrs.
11	Arcosol 50 (Valle 1)	Spain	Trough/	49.9	Diphenyl

			2-tank indirect		Molten salt 5,10,150 7.5 hrs.
12	Arenales	Spain	Trough/ 2-tank indirect	50	Biphenyl Molten salt 5,10,150 7 hrs.
13	ASE Demo Plant	Italy	Trough/–	0.35	Molten salt Molten salt 3,398 –
14	Ashalim	Israel	Tower/–	121	– Molten salt – 4.5 hrs.
15	Ashalim Plot B (Megalim)	Israel	Tower/–	121	Water/steam – 10,52,480 –
16	Aste 1A	Spain	Trough/ 2-tank indirect	50	Dowtherm A Molten salt 5,10,120 8 hrs.
17	Aste 1B	Spain	Trough/ 2-tank indirect	50	Dowtherm A Molten salt 5,10,120 8 hrs.
18	Astexol II	Spain	Trough/ 2-tank indirect	50	Thermal Oil Molten salt 5,10,120 8 hrs.
19	Atacama-1	Chile	Tower/ 2-tank direct	110	Molten salt Molten salt 14,84,000 17.5 hrs.
20	Aurora	Australia	Tower/ 2-tank direct	150	Molten salt Molten salt – 8 hrs.
21	Augustin Fresnel 1	France	LFR/ Other	0.25	Water – 400 0.25 hrs.
22	Bokpoort	South Africa	Trough/ 2-tank indirect	50	Dowtherm A Molten salt 5,88,600 9.3 hrs.
23	Borges Termosolar	Spain	Trough/–	22.5	Thermal Oil – 1,83,120

					–
24	Casablanca	Spain	Trough/ 2-tank indirect	50	Diphenyl Molten salt 5,10,120 7.5 hrs.
25	Chabei	China	Trough/ 2-tank direct	64	Molten salt Molten salt – 16 hrs.
26	City of Medicine Hat ISCC	Canada	Trough/–	1.1	Xceltherm®600 – 5,248 –
27	Colorado Integrated Solar	USA	Trough/–	2	Xceltherm®600 – 6,540 –
28	Copiapo	Chile	Tower/ 2-tank direct	260	– Molten salt – 14 hrs.
29	Crescent Dunes	USA	Tower/ 2-tank direct	110	Molten salt Molten salt 11,97,148 10 hrs.
30	Dacheng Dunhuang	China	LFR/ 2-tank direct	50	Molten salt Molten salt – 13 hrs.
31	Dadri ISCC Plant	India	LFR/–	14	Water – 33,000 –
32	Dahan Power Plant	China	Tower/ Other	1	Water/steam Saturated steam 10,000 1 hr.
33	Delingha Solar Thermal Power	China	Tower/ 2-tank direct	810	Thermal Oil Molten salt – 9 hrs.
34	DEWA	UAE	Tower/ 2-tank direct	100	Molten salt Molten salt – 15 hrs.
35	DEWA	UAE	Trough/ 2-tank indirect	600	Thermal Oil Molten salt – 10 hrs.

36	Dhursar	India	LFR/–	125	– – – –
37	Diwakar	India	Trough/ 2-tank indirect	100	Synthetic Oil Molten salt – 4 hrs.
38	eCare Solar Thermal Project	Morocco	LFR/ Other	1	Water Steam 10,000 2 hrs.
39	Enerstar (Villena)	Spain	Trough/–	50	Thermal Oil – 3,39,506 –
40	Extresol-1 (EX-1)	Spain	Trough/ 2-tank indirect	50	Diphenyl Molten salt 5,10,120 7.5 hrs.
41	Extresol-2 (EX-2)	Spain	Trough/ 2-tank indirect	49.9	Diphenyl Molten salt 5,10,120 7.5 hrs.
42	Extresol-3 (EX-3)	Spain	Trough/ 2-tank indirect	50	Diphenyl Molten salt 5,10,120 7.5 hrs.
43	Gansu Akesai	China	Trough/ 2-tank direct	50	Molten salt Molten salt – 15 hrs.
44	Gemasolar Thermo solar Plant	Spain	Tower/ 2-tank direct	19.9	Molten salt Molten salt 3,04,750 15 hrs.
45	Genesis	USA	Trough/–	250	Dowtherm A – – –
46	Godavari	India	Trough/–	50	Dowtherm A – 3,92,400 –
47	Golden	China	Tower/ 2-tank direct	100	Molten salt Molten salt – 8 hrs.
48	Golmud	China	Tower/ 2-tank direct	200	Molten salt Molten salt

					– 15 hrs.
49	Greenway CSP Mersin Tower	Turkey	Tower/–	1	Water/steam Molten salt – –
50	Gujarat Solar One	India	Trough/ 2-tank indirect	25	Diphenyl Molten salt 3,26,800 9 hrs.
51	Gulang	China	Trough/ 2-tank indirect	100	Thermal Oil Molten salt – 7 hrs.
52	Guzmán	Spain	Trough/–	50	Dowtherm A – 3,10,406 –
53	Hami	China	Tower/ 2-tank direct	50	Molten salt Molten salt – 8 hrs.
54	Helioenergy 1	Spain	Trough/–	50	Thermal Oil – 3,00,000 –
55	Helioenergy 2	Spain	Trough/–	50	Thermal Oil – 3,00,000 –
56	Helios I (Helios I)	Spain	Trough/–	50	Thermal Oil – 3,00,000 –
57	Helios II (Helios II)	Spain	Trough/–	50	Xceltherm®MK – – 2 hrs.
58	Holaniku at Keahole Point	USA	Trough/ Other	2	Xceltherm®600 – – 2 hrs.
59	Huanghe Qinghai Delingha	China	Tower/ 2-tank indirect	135	Water/steam Molten salt – 3.7 hrs.
60	Ibersol Ciudad Real (Puertollano)	Spain	Trough/–	50	Dowtherm A – 2,87,760 –

61	Ilanga I	South Africa	Trough/2-tank indirect	100	Thermal Oil Molten salt 8,69,800 4.5 hrs.
62	IRESEN CSP-ORC	Morocco	LFR/ Other	1	Mineral Oil – 11,400 20 min.
63	ISCC Ain Beni Mathar	Morocco	Trough/–	20	TherminolVP-1 – 1,83,120 –
64	ISCC Duba 1	Saudi Arabia	Trough/–	43	Thermal Oil – – –
65	ISCC Hassi R'mel	Algeria	Trough/–	20	Thermal Oil – 1,83,120 –
66	ISCC Kuraymat	Egypt	Trough/–	20	TherminolVP-1 – 1,30,800 –
67	Ivanpah Solar Electric Generation	USA	Tower/–	377	Water – 2,60,000 –
68	Jemalong Solar Thermal Station	Australia	Tower/ 2-tank direct	1.1	Liquid sodium Liquid sodium 15,000 3 hrs.
69	Jülich Solar Tower	Germany	Tower/ Other	1.5	Air Ceramic 17,650 1.5 hrs.
70	Kathu Solar Park	South Africa	Trough/ 2-tank indirect	100	Thermal Oil Molten salt – 4.5 hrs.
71	KaXu Solar One	South Africa	Trough/ 2-tank indirect	100	Thermal Oil Molten salt 8,00,000 2.5 hrs.
72	Khi Solar One	South Africa	Tower/ Other	50	Water/steam Saturated steam 5,76,800

					2 hrs.
73	Kimberlina Solar Thermal Power	USA	LFR/–	5	Water – 25,988 –
74	Kogan Creek Solar Boost	Australia	LFR/–	44	
75	KVK Energy Solar Project	India	Trough/ 2-tank indirect	100	Synthetic Oil Molten salt – 4 hrs.
76	La Africana	Spain	Trough/ 2-tank indirect	50	– Molten salt 5,50,000 7.5 hrs.
77	La Dehesa	Spain	Trough/ 2-tank indirect	49.9	Dephenyl Molten salt 5,52,750 7.5 hrs.
78	La Florida	Spain	Trough/ 2-tank indirect	50	Dephenyl Molten salt 5,52,750 7.5 hrs.
79	La Risca (Alvarado I)	Spain	Trough/–	50	Biphenyl – 3,52,854 –
80	Lake Cargelligo	Australia	Tower/ Other	3	Water/steam Graphite 6,080 –
81	Lebrija 1 (LE-1)	Spain	Trough/–	50	Therminol VP-1 – 4,12,,020 –
82	Liddell Power Station	Australia	LFR/–	9	Water/steam – 18,490 –
83	Likana	Chile	Tower/ 2-tank direct	390	Molten salt Molten salt – 13 hrs.
84	Llo Solar Thermal Project (Llo)	France	LFR/ Other	9	Biphenyl – 3,72,240 –
85	Majadas I	Spain	Trough/–	50	Dephenyl – 3,72,240

					–
86	Manchasol-1 (MS-1)	Spain	Trough/ 2-tank indirect	49.9	Diphenyl Molten salt 5,10,120 7.5 hrs.
87	Manchasol-2 (MS-2)	Spain	Trough/ 2-tank indirect	50	Diphenyl Molten salt 5,10,120 7.5 hrs.
88	Maricopa Solar Project	USA	Dish/Engine/-	1.5	– – – –
89	Martin Next Generation Solar	USA	Trough/–	75	Dowtherm A – 4,64,908 –
90	Megha Solar Plant	India	Trough/–	50	Xceltherm MK1 – 3,66,240 –
91	MINOS	Greece	Tower/ 2-tank indirect	52	– Molten salt – 5 hrs.
92	Mojave Solar Project	USA	Trough/–	250	Therminol VP-1 – – –
93	Morón	Spain	Trough/–	50	Therminol Oil – 3,80,000 –
94	National Solar Thermal Power	India	Trough/–	1	Therminol VP-1 – 8,000 –
95	Nevada Solar One (NSO)	USA	Trough/ 2-tank indirect	72	Dowtherm A – 3,57,200 0.5 hrs.
96	NOOR I	Morocco	Trough/ 2-tank indirect	143	Dowtherm A Molten salt – 3 hrs.
97	NOOR II	Morocco	Trough/ 2-tank indirect	200	Thermal Oil Molten salt –

					7 hrs.
98	NOOR III	Morocco	Trough/ 2-tank indirect	150	Molten salt Molten salt – 7 hrs.
99	Olivenza 1	Spain	Trough/–	50	Thermal Oil – 4,02,210 –
100	Orellana	Spain	Trough/–	50	Thermal Oil – 4,02,210 –
101	Palen Solar Electric Generation	USA	Tower/–	500	
102	Palma del Río I	Spain	Trough/–	50	Biphenyl – 3,97,240 –
103	Palma del Río II	Spain	Trough/–	50	Biphenyl – 3,97,240 –
104	Pedro de Valdivia	Chile	Trough/ 2-tank indirect	360	Thermal Oil Molten salt – 10.5 hrs.
105	Planta Solar 10 (PS10)	Spain	Tower/ Other	11	Water – 75,000 1 hr.
106	Planta Solar 20 (PS20)	Spain	Tower/ Other	20	Water – 1,50,000 1 hr.
107	Puerto Errado 1 Thermosolar	Spain	LFR/ Thermocline	1.4	Water – – –
108	Puerto Errado 2 Thermosolar	Spain	LFR/ Thermocline	30	Water – 3,02,000 0.5 hr.
109	Qinghai Delingha Solar Thermal	China	Tower/ 2-tank indirect	270	Molten salt Molten salt – 6 hrs.
110	Rays power Yumen	China	Trough/ 2-tank indirect	50	Thermal Oil Molten salt –

					7 hrs.
111	Redstone Solar Thermal Power	South Africa	Tower/ 2-tank indirect	100	Molten salt Molten salt – 12 hrs.
112	Rende-CSP Plant	Italy	LFR/–	1	Diathermic Oil – – –
113	Rice Solar Energy Project (RSEP)	USA	Tower/ Other	150	
114	Saguaro Power Plant	USA	Trough/–	1	Xceltherm ®600 – 10,340 –
115	Shagaya	Kuwait	Trough/ 2-tank indirect	50	– Molten salt – 10 hrs.
116	Shams 1 (Shams 1)	UAE	Trough/–	100	Thermal VP-1 – 6,27,840 –
117	Shangyi	China	Tower/ 2-tank indirect	50	Water/steam Molten salt – 4 hrs.
118	Sierra Sun Tower (Sierra)	USA	Tower/–	5	Water – 27,670 –
119	Solaben 1	Spain	Trough/–	50	Thermal Oil – 3,00,000 –
120	Solaben 2	Spain	Trough/–	50	Thermal Oil – 3,00,000 –
121	Solaben 3	Spain	Trough/–	50	Thermal Oil – 3,00,000 –
122	Solaben 6	Spain	Trough/–	50	Thermal Oil – 3,00,000 –
123	Solacor 1	Spain	Trough/–	50	Thermal Oil –

					3,00,000 –
124	Solacor 2	Spain	Trough/ None	50	Thermal Oil – 3,00,000 –
125	Solana Generating Station	USA	Trough/ 2-tank indirect	250	Therminol PV-1 Molten salt 2,20,000 6 hrs.
126	SEGS I	USA	Trough/ 2-tank direct	13.8	– Molten salt 82,960 3 hrs.
127	SEGS II	USA	Trough/–	30	– – 1,90,338 –
128	SEGS III	USA	Trough/–	30	Thermal Oil – 2,30,000 –
129	SEGS IV	USA	Trough/–	30	Thermal Oil – 2,30,000 –
130	SEGS V	USA	Trough/–	30	Thermal Oil – 2,50,000 –
131	SEGS VI	USA	Trough/–	30	Thermal Oil – 1,88,000 –
132	SEGS VII	USA	Trough/–	30	Thermal Oil – 1,92,280 –
133	SEGS VIII	USA	Trough/–	80	Thermal Oil – 4,64,340 –
134	SEGS IX	USA	Trough/–	80	Thermal Oil – 4,83,960 –
135	Solnova 1	Spain	Trough/–	50	Thermal Oil – 3,00,000 –

136	Solnova 3	Spain	Trough/–	50	Thermal Oil – 3,00,000 –
137	Solnova 4	Spain	Trough/–	50	Thermal Oil – 3,00,000 –
138	Stillwater GeoSolar Hybrid Plant	USA	Trough/–	17	Water – 656 –
139	SunCan Dunhuang Phase I	China	Tower/ 2-tank direct	10	Molten salt Molten salt 1,75,375 15 hrs.
140	SunCan Dunhuang Phase II	China	Tower/ 2-tank direct	100	Molten salt Molten salt – 11 hrs.
141	Sundrop	Australia	Tower/–	1.5	Water – 51,505 –
142	Supcon Solar Project	China	Tower/ 2-tank direct	50	Molten salt Molten salt 4,34,880 6 hrs.
143	Tamarugal	Chile	Tower/ 2-tank direct	450	Molten salt Molten salt – 13 hrs.
144	Termesol 50 (Valle 2)	Spain	Trough/ 2-tank indirect	49.9	Diphenyl Molten salt 5,10,120 7.5 hrs.
145	Termosol 1	Spain	Trough/ 2-tank indirect	50	Thermal Oil Molten salt 5,23,200 9 hrs.
146	Termosol 2	Spain	Trough/ 2-tank indirect	50	Thermal Oil Molten salt 5,23,200 9 hrs.
147	Thai Solar Energy 1 (TSE1)	Thailand	Trough/–	5	Water – 45,000 –
148	Tooele Army Depot	USA	Dish/Engine/–	1.5	Helium –

					35 –
149	Urat	China	LFR/ 2-tank indirect	50	Thermic Oil Molten salt – 6 hrs.
150	Urat Middle Banner	China	Trough/ 2-tank indirect	100	Thermic Oil Molten salt – 4 hrs.
151	Waad Al Shamal ISCC Plant	Saudi Arabia	Trough/–	50	Thermic Oil – – –
152	Xina Solar One	South Africa	Trough/ 2-tank direct	100	Thermic Oil Molten salt – 5.5 hrs.
153	Yumen	China	Tower/ 2-tank direct	100	Molten salt Molten salt – 10 hrs.
154	Yumen	China	Tower/ 2-tank direct	50	Molten salt Molten salt – 9 hrs.
155	Yumen	China	Trough/ 2-tank indirect	50	Molten salt Molten salt – 7 hrs.
156	Zhangbei	China	LFR/ Other	50	Water Concrete – 14 hrs.
157	Zhangjiakou	China	LFR/ Other	50	Water Concrete – 14 hrs.

1.10 Motivation of the thesis

SHS systems store/release the heat energy at high heat transfer rates during heat storage and recovery processes, due to which the SHS systems are widely used in commercial purposes. The charging and discharging times of the SHS systems should be low. Hence, proper design and optimization of SHS systems is of vital importance. The development of a 3D numerical model is necessary to evaluate the performance characteristic of the storage system without conducting expensive experimental studies.

A detailed experimental study is also required to crosscheck the developed numerical model for further applicability of the model to the development of real time storage systems. In the present thesis, the performances of lab-scale shell-and-tube regenerative type SHS prototype with multiple tubes and fins is studied. A major importance is given to the heat transfer between the SHS material and HTF.

1.11 Organization of the thesis

The thesis is organized in 7 chapters. A brief description of the content of each of the chapters is provided below:

Chapter 1, starts with a brief introduction of TES, types of TES and the importance of TES with CSP plants. Special focus is given to the SHS system. The classification of SHS systems and their various engineering applications and motivation of the present work are presented in Chapter 1.

In Chapter 2, a detailed review of literature on various aspects of SHS technology such as conjugate heat transfer, storage module configuration and heat-transfer enhancement techniques are presented. Various numerical models and experimental investigations carried out at different operating conditions during charging and discharging processes of sensible based SHS systems are also reviewed. Based on the conclusions of the literature survey, objectives of the present thesis work are framed.

Chapter 3, gives the details of the concrete mix design grade and fabrication of the lab scale SHS prototypes. In addition, measurement of thermo physical properties of the filled concrete material and thermal cycle's effects are presented in this chapter.

Chapter 4, describes the design of various prototype configurations, experimental setup and the procedure followed for testing the lab-scale SHS prototype. The results acquired from the experimental studies during the charging and discharging processes are presented.

Chapter 5, is devoted to the design and 3D numerical formulation of the lab scale storage device for predicting the conjugate heat transfer characteristics. The results obtained from the numerical model during both charging and discharging processes are presented. Detailed parametric studies on all three prototypes chosen are also discussed.

Chapter 6, covers the details of thermal modelling of different high temperature SHS bed configurations. The results obtained from the comparative study on the performances of different high temperature SHS configurations are presented.

Chapter 7, draws the major conclusions arrived from the numerical and experimental studies on various lab-scale SHS prototypes. Scope for future work and recommendations are also given in this chapter.

1.12 Summary

This chapter starts with a brief introduction of various methods and concepts of TES systems. Various advantages of the SHS systems when compared with the other TES systems are also explained. The classification of SHS systems and its usage in several applications are presented. The motivation of the thesis is discussed and finally the thesis structure is clearly explained in sequence.

Chapter 2

Review of literature

Concentrating solar power (CSP) technologies have been used for many years. They allow the utilization of clean and renewable energy, which is also cost competitive when compared to the traditional fossil fuels. Also, as compared to other renewable energy technologies like, wind power and photovoltaic, CSP technology is relatively cheap and efficient in terms of energy storability and dispatchability. The four existing configurations of CSP technologies, in the order of priority are Parabolic Trough Collector (PTC), Linear Fresnel Reflector (LFR), Solar Power Tower (SPT) and dish/engines for power generation in stand-alone mode at various plant capacities (Brosseau et al., 2005; Reddy and Kumar, 2012; Skinner et al., 2013).

However, the intermittent nature of the solar radiation necessitates the integration of a TES system which further increases the efficiency of CSP plant. TES systems are necessary component for more than 70% of recent CSP plants and such plant has a potential to generate much more revenue than the one without TES (Pacheco et al., 2002). More importantly, the integration of efficient and cost effective TES systems is one of the key factors that determine the development of CSP technology, so as to overcome the CSP's intermittent character and render it more economically competitive. Sensible heat storage (SHS) technology is the most used TES in CSP plants due to their reliability, low cost, ease of implementation (Pelay et al., 2017). Hence, a significant amount of works are reported in the literature on the SHS technologies. There are different types of sensible heat TES systems available which include: active one-tank and two-tank direct/indirect TES systems, and single tank passive packed bed TES systems, with different storage media and HTFs.

Development of a stable and real-time numerical model is important to predict the storage performance, which overcomes experimental constraints. However, performing experimental studies in real situation is very challenging to get the realistic performance of the systems. Hence, several researchers developed various numerical models, including aspects such as heat-transfer enhancement techniques, and new solving methodologies. Alternate performance tests on SHS systems conducted at different operating conditions are also reported in the literature. In this chapter, the state of technological developments on SHS and various heat transfer enhancement techniques are discussed. A detailed literature survey on the numerical models and experimental investigations on the SHS systems are discussed. Further, influence of different TES methodologies and improved HTFs with the CSP power plants are presented.

2.1 Active – sensible TES in Commercial CSP plants

A system in which storage medium is circulating between the heat exchanger to transfer the heat energy either to the working fluid or the HTF is called as active system. In the active system, the storage system is often composed of two tanks, one for the coldest part of the storage media and the other for the warmest part. The storage media is a fluid within the range of temperature considered, and it is also used as a HTF. It flows through a heat exchanger to transfer heat during the charging/discharging processes.

2.1.1 Thermocline

A thermocline TES system uses a single tank to store both the hot and cold fluid, along with a low cost filler material making it competitive against two-tank storage systems. A thermal stratification is present in the tank due to the natural buoyancy forces of fluids. The thermal stratification is enhanced by a filler material. Generally, during the charging/discharging phase, the TES system needs to be fed with hot/cold air from the top/bottom of the tank (Pacheco et al., 2002). This type of TES system is more efficient and cheaper (35% in cost) solution for STPPs compared to 2-tank TES systems design (Brosseau et al., 2005).

Schumann, (1929) presented the mathematical treatment of the problem to find the distribution of temperature in the prism (or cylinder) and in the fluid (HTF at a higher temperature) with respect to time. The temperature distributions were solved assuming the well-known heat transfer laws from a liquid in turbulent motion to a solid. If a gas is used instead of a liquid, the problem is much more complicated, but a dimensional method of treating the problem leads to results which would be very useful in practice.

Bejan, (1978) made an analysis of the thermodynamic irreversibilities associated with storing energy in huge liquid baths from a hot gas source as sensible heat and pointed out two thermodynamic optima.

(i) There exists well defined quantity of hot gas to be used to maximize the useful work stored in the bath.

(ii) There exists a relation, which provides a procedure for estimating the heat exchanger optimum number of thermal units (N_{tu}). Increasing the parameters more than the above optima lead to severe thermodynamic losses.

Krane, (1987) reported the second law techniques based on the minimization of entropy generation and applied to optimal design and sensible heat TES system. The results of his study showed

(i) Entire operational cycle (heat charge and discharge process), must be considered in order to optimize the design and performance of sensible heat TES system.

(ii) A typical optimum system destroys 70 – 90 % of the entering availability and so it has low thermodynamic efficiency.

Eames and Norton, (1998) validated a transient 3-D, finite-volume based model to investigate the thermal performance of a stratified hot water storage tank. It is validated by comparison with the measured temperatures from a series of thirty-two experiments. These experiments included the variation of inlet velocities, temperatures and initial store stratification profiles. A parametric analysis estimated the effect of inlet/outlet port locations on store performance for a range of operating conditions. The effects of finite volume size on predicted levels of entrainment and diffusion in the inlet region were reported.

Guo, (2001) described the mechanism of convective heat transfer based on the analogy between convection and conduction with heat sources. The analysed results showed that the strength of convective heat transfer depends not only on the fluid velocity and fluid properties, but also on the coordination of fluid velocity and heat flow fields. Further, based on the included angle (ß) of velocity and temperature gradient vectors, the presence of fluid motion may reduce or enhance heat transfer.

Rosen, (2001) numerically investigated the performance of TES systems with thermal stratification based on energy and exergy analyses. The researcher considered about six temperature distribution models (linear, stepped, continuous-linear, general-linear, basic three-zone and general three-zone) were considered for evaluation of energy and exergy contents. The models depicted the way that the quantities of energy and exergy contained in a vertically stratified TES differ. Improving stratification increased the TES efficiency, and use of stratification could increase the exergy storage capacity of TES.

Yang and Garimella, (2010b) developed a comprehensive two-dimensional model to investigate TES in a molten-salt thermocline. The governing equations are solved using a finite-volume approach. Thermal characteristics including temperature profiles and discharge efficiency were reported. They developed correlations to predict the discharge efficiency of the thermocline storage tank for Reynolds number in the range of 1–50 and non-dimensional tank height of 10–800. The same research group (2010) investigated the adiabatic and non-adiabatic wall boundaries using a computational heat transfer model for the discharging process with the HITEC molten-salt as the HTF and the filler material as the quartzite in the tank. Results showed that

(i) The differences in temperature profiles between adiabatic and non-adiabatic thermoclines are greatly reduced as the HTF flow rate is increased.

(ii) During the discharge process the outflow temperature is significantly reduced at lower Reynolds number in non-adiabatic thermoclines, compared to that of adiabatic ones, which in turn decreased the discharge efficiency of thermoclines. However, its effect is insignificant at high HTF-flow Reynolds numbers.

2.1.2 Two – tank storage concepts for direct and indirect TES Systems

The most common and advanced TES solutions for STPPs are based on two-tank systems with synthetic oil or molten salt. In a two-tank direct TES system, the storage medium also used as the HTF. The heat energy is directly transferred to the working fluid without the aid of any intermediate heat exchanger. The main advantage is that the cost is reduced due to the elimination of the expensive intermediate heat exchanger in the system. Where as in indirect TES systems a secondary medium is used as HTF and necessitates an intermediate heat exchanger (Gil et al., 2010; Kuravi et al., 2013).

Two-tank sensible heat TES system consists of a hot and cold tank. The hot tank is the one where the heated fluid from the collector field (direct system) or the heat exchanger (indirect system) is stored in order to be used during cloudy periods or night time. This hot fluid is taken from the hot tank to heat steam for power generation. The cold fluid that has released its stored thermal energy is then moved to the cool tank. The cool tank holds the liquid until it is needed again to charge the TES system. The hot and cold fluid does not exchange heat, as they are not in contact with each other (Wang et al., 1985). Further, there can be a large difference in the temperatures of the hot and cold tank which will increase the Rankine cycle efficiency. A disadvantage of these systems is that, cost of the tank and the fluid make this option considerably expensive one in both direct and indirect 2-tank TES systems. According to Dinter et al., (1990), the cost for such storage is about \$41/kWh$_{th}$. Kelly and Herrmann, (2000) also, confirmed this number in their study. In addition, at high temperature storage, there is a risk of solidification of the fluids due to their high freezing temperatures. Hence, the operating temperature is limited to 400 – 550 °C (Gil et al., 2010; Wang et al., 1985).

Other promising storage concepts are significantly less advanced and are under development, such as concrete storage, PCM storage, and chemical storage. These concepts promise a considerable cost reduction compared to the 2-tank systems (Herrmann and Kearney, 2002). The 2-tank storage systems which have been demonstrated in large scale [SEGS I (oil) and Solar Two (molten salt)] and the oil-rock thermocline (Solar One).

The following review gives the overview of the 2-tank (direct and indirect) TES systems with different technologies, optimization and cost-effective methodologies.

Wang et al., (1985) presented three concepts namely, raft-thermocline, two-tank and dual-media-thermocline systems) for high-temperature TES in solar central receiver systems. They presented design options and operation criteria for sensible-heat, molten-salt storage with internal insulation to reduce corrosion and retain strength sufficiently in the storage containing wall.

Kandari, (1990) conducted an experimental investigation on a stratified tank (22 m^3) which acted as a buffer reservoir between the paraboloid-dish solar collector and the turbine energy-conversion device. The results showed that the disturbed zone is 1500 mm thick (i.e. nearly, 30% of usable tank height). Based on these results, an experimental model of 1/25th scale by volume was constructed to study the effect of using improved distributor header geometry. Using the new header configuration, extraction efficiencies for both the charging/discharging processes are in the range of 73 to 85%.

Castro et al., (1991) described a comparison and evaluation of the Solar One, CESA-I receiver and TES systems. The evaluation is based on operating data from Solar One (l0 MWe) and CESA-I (1.2 MWe) experimental CSP plants. Major comparisons included between were: external verses cavity receiver; thermocline vs. 2-tank storage; and 10 MWe versus 1.2 MWe plant size. The performance comparison has provided the understanding of the plant design variables to improve the future CSP plants.

Kearney et al., (2003) investigated the feasibility of using a molten salt as the HTF and storage material in a parabolic trough solar field to improve system performance and to reduce the Levelized electricity cost (LEC). Assuming a two-tank system and a maximum operation temperature of 450 °C, the LEC could be reduced by 14.2 % compared to a state-of-the-art parabolic trough plant, such as the SEGS plants in California. They also concluded that if higher temperatures are possible, the improvement would be as high as 17.6%.

Pacheco et al., (2002) developed a thermocline indirect TES system in which quartzite and silica sand are selected as the most practical filler materials because of their availability, cost and compatibility with nitrate salts. Results from the pilot-scale test confirmed that the thermal capacity of the thermocline was near the calculated value. The height of the thermal gradient corresponded to that predicted (6.1 m) by the model. Heat losses were higher than predicted primarily due to the heat losses through pump penetrations on the top of the tank. However, in a large TES that effect would be negligible impact. The results of this work showed that a molten-salt thermocline system is a feasible option for TES in a PTPP.

Kearney et al., (2004) investigated the feasibility of utilizing a molten salt as HTF and for thermal storage in a parabolic trough solar field to improve system performance and reduce the LEC. This work addressed the concerns of operation and maintenance issues associated with the routine freeze protection, solar field preheat methods, collector loop maintenance and the selection of appropriate materials for piping and fittings.

Herrmann et al., (2004) assessed the technical and economic feasibility of a 2-tank molten salt storage. Detailed performance and cost analyses were conducted to evaluate the economic value. The analyses are mainly based on the operation experience from the SEGS plants and the solar two project. The study concluded that the specific cost for a 2-tank molten salt storage is in the range of US$ 30–40/kWh$_{th}$, depending on storage size and it can be reduced further, provided the storage is big enough. A storage of 12 hr. full load capacity reduces the LEC by about 10%.

Vaivudh et al., (2008) studied two types of heat exchangers namely, the vertical pipe and helical coiled pipe heat exchangers for high temperature TES (max. 340 °C). Thermal oil is used as the HTF and TES medium in this experiment. The charging and discharging times were 40 min for 3 kWh capacity of charging and 1 kWh capacity of discharging respectively. The highest TES efficiency during the charging/discharging was 43.6% / 63.1% at the HTF flow rate of 0.1 kg/s in a helical coiled pipe heat exchanger. They validated the model experimentally with ± 10 % errors.

Andreu-Cabedo et al., (2014) studied the storage performances of the salt -nano-fluids based on eutectic mixtures of nitrate with SiO_2 (silica) nanoparticles system. Solar salt (60% $NaNO_3$ + 40% KNO_3) used in the CSP plants was doped with silica nanoparticles at different solid mass concentrations (i.e., 0.5, 1.0, 1.5, and 2 wt. %). From the synthesized samples, it was revealed that specific heat increased to 25 % at an optimal concentration of 1 wt. % of nanoparticles for a temperature range from 250 °C to 420 °C. The mechanism involved in the specific heat increment is based on a surface phenomenon. The increase in the specific heat capacity of the salt based nano-fluid could significantly reduce the cost of the TES media in CSP.

2.1.3 Steam accumulators

Steam accumulator is an equipment which accumulates energy in the form of pressurized hot water that flashes to produce steam at lower pressure. The accumulator releases the steam when the demand is greater than the boiler's ability and accepts the steam when demand is low. Producing the steam by Direct Steam Generation (DSG) concept in parabolic trough collectors is a promising option. According to previous studies, the cost reduction of the DSG process compared to the SEGS technology is expected to be approximately 10 % (Markus et al., 2009).

Lavan and Thompson, (1977) studied experimentally the temperature stratification in hot water TES systems. A novel inlet and exit configuration scheme was designed for a 300 L and a 1900 L storage tank. The experimental study showed that even at very large flow rates, thermal stratification can be maintained in cylindrical water tanks. Stratification improves with increasing the tank length to diameter ratio (L/D), ΔT, inlet and outlet port diameters, while it decreases with increasing flow rates. The data were experimentally correlated to predict the efficiency in terms of an inlet Reynolds number, a tank Grashof number and the L/D ratio. The extraction efficiency in the case of 300 L was 90 % due to the transport of heat via the vessel walls.

Eck et al., (2003) investigated both experimentally and theoretically to improve the DSG process for short time energy storage for more than 3700 h in a test facility of the DISS (Direct solar steam) project. It includes thermal storage, water–steam separators and receivers to withstand higher process temperatures. The main conclusions of this task were: the DSG process is feasible in horizontal parabolic troughs, and the recirculation process is the most attractive option for commercial DSG collector fields. Furthermore, a deep insight in the thermo-hydraulic behavior of the DSG process in horizontal parabolic troughs has been achieved.

Herrmann et al., (2004) presented a comparative analysis of PTPP with and without TES system. This analysis was for steam generation and storage mode. They used binary mixture of sodium nitrate and potassium nitrate as the storage media for storing 50 MWh energy in the temperature range of 300-385 °C for 0-15 hr. of storage. Outputs were validated with the measured data of performance results of SEGS plant. Results showed that storage time of 12 hour can reduce the LEC by 10 %.

Zarza et al., (2006) designed the first solar power plant (5-MWe) in the world using DSG in a parabolic-trough solar field connected to a superheated steam Rankine power cycle. Experience in the DSG process acquired during the DISS project was applied in designing the solar field of this plant, assuring high operational flexibility and reliability. The solar field produced 410 °C/70-bar superheated steam.

Markus et al., (2009) commissioned the distributed control system and heating of the TES system. This was the first time that the DSG process and the required components were investigated experimentally at the elevated operation conditions (112 bar and 500 °C). Thus, the group got valuable information required for the future design of a commercial DSG power plant with these optimized operating conditions.

Montes et al., (2009) described the influence of the solar multiple on the annual performance of 50 MWe DSG power plant, with TES and auxiliary natural gas-fired boiler. Once the yearly parameters of the STPP were calculated, the economic analysis was performed, assessing the effect of the solar multiple in the LEC, as well as in the annual natural gas consumption. LCE values have been obtained for a specific economic scenario. It can be observed that the LEC is greater as the solar multiple of the power plant increases, mainly due to the high investment cost in the solar field.

Birnbaum et al., (2010) presented the changes in the plant layout of a parabolic trough power plant with DSG and compared a plant with indirect steam generation oil system. Two configurations for the steam parameters, i.e., 110 bars/400°C and 156 bars/500°C, were suggested based on a commercially available steam turbine. A reheat system was desirable to avoid high moisture content in the low-pressure turbine for both configurations. The interactions between the three subsystems; solar field, power block, and thermal storage were analyzed. Different alternatives based on available technologies were presented and evaluated as the environmental issues of the oil based technology was not feasible for CSP. Other options such as hybridization for enhanced steam parameters could be interested under different boundary conditions

Dersch et al., (2014) compared two parabolic trough CSP plants technically and economically using full thermodynamic models. One of them was a hybrid plant (natural gas fired) in order to reach 540 °C steam temperature whose design was similar to the Shams one plant (www.nrel.gov). The second plant was a parabolic trough plant using molten salt as the HTF and TES material. Both plants were equipped with almost the same power block and showed similar annual performance. The molten salt plant demonstrated a cost reduction of about 10 % compared to the reference plant. Furthermore, the molten salt plant offers electricity production towards the evening hours since it had a TES.

Prieto et al., (2018) compared three different TES options in DSG plants: accumulators with superheating (Acum-SH), accumulators with 2-tank molten salt (Acum-MS), and PCM with 2-tank molten salt (PCM-MS) at higher temperatures above 400 °C. The higher temperatures were achieved; in a first stage heating up to 450 °C and in a second stage heating up to 550 °C. It was concluded that the combination based on PCM-MS with a more equivalent storage of 6 hr., Acum-SH with lower than 6 hr. and Acum-PCM for more than 6 hr. of storage were considered as the best options.

2.2 Passive –TES Concepts for SHS systems

Passive TES systems are typically dual medium storage systems in which the HTF carries energy received from the energy source to the storage medium during charging and transfers energy from the storage system when discharging. The storage medium is mainly solid substance such as concrete/rocks/sand/PCMs which does not circulate (Kuravi et al., 2013). These systems are also called as regenerators. The arrangement for the HTF to flow through the storage medium is a major concern due to low heat transfer rate with the solid storage materials. The foremost disadvantage of these systems is that the temperature of HTF decreases during discharging as the storage medium cools down. However, the advantage of solid concrete is the very low cost of thermal energy stored with facility to handle the material and low degradation of its properties (Gil et al., 2010; Kuravi et al., 2013).

2.2.1 Solid SHS media with air as the HTF

Riaz, (1977) described the dynamic behavior of rock-bed TES systems using single and two-phase models. The classical Schumann two-phase model normally ignores axial conduction while the single-phase model is essentially a simple convection—conduction representation in which rock and air are at the same temperature. The developed closed-form solutions for the transient response of the equivalent single-phase model of a packed bed provided a simple and convenient means for estimating the long-term dynamic performance of TES systems without resorting to complex computer simulations.

Sragovich, (1989) analysed the transient behaviour of SHS material (magnesia). He reported that HTF outlet temperature increased with reduced tube diameter and that is because of increase in convection heat transfer inside narrower tubes. They further noticed that there is always a critical mass flow rate at which outlet temperature of HTF dropped suddenly and this critical value varies in same fashion as tube diameter.

Aly and Elsharkawy, (1990) studied numerically the effects of storage medium properties on the thermal behaviour of packed beds using 1-D model to describe the temperature fields in the air (HTF) and solid media. They reported that increasing either the density or specific heat, increases the rate and capacity of energy storage, and decreases the rate of temperature rise throughout the storage medium. On increasing the thermal conductivity, increases the rate of temperature rise and energy stored inside the bed.

Domanski and Fellah, (1996) studied numerically the thermo-economic aspects in designing and operating sensible heat TES systems for the entire charging–discharging cycle. They analysed a balance between the cost of the irreversibility rate and storage system which is the basic technique for thermo-economic optimization. This analysis provided a tool to select the right storage unit for a given application at minimum total cost.

Hanchen et al., (2011) developed and experimentally validated a heat transfer model for a TES system consisting of a packed bed of rocks for evaluating charging/discharging characteristics. Validation was accomplished using the data extracted from a pilot-scale experimental setup built with a packed bed of crushed steatite (magnesium silicate rock). A parameter study of the packed bed dimensions, fluid flow rate, particle diameter and solid phase material was carried out to evaluate the charging/discharging characteristics, daily cyclic operation, overall thermal efficiency and capacity ratio. A cyclic steady state is reached after about 26 hr charge and 6 hr discharge daily cycles.

Strasser and Selvam, (2014) proposed an alternative to the currently-used thermocline storage systems by structured concrete systems to avoid the issues of material settlement and thermal ratcheting. Numerical models were developed to simulate the performance of the utility scale packed bed thermocline (PBTC) and structured concrete thermocline (SCTC) storage systems. It is found that, a PBTC was 8.4 % more efficient than a SCTC. However, SCTC storage system bears no concerns of thermal ratcheting of the tank’s walls and concluded that the SCTC was the most viable TES option.

2.2.2 Packed beds

Thermoclines with filler materials can be characterized as packed bed systems. These packed bed systems are single tank systems which consist of storage material elements in numerous shapes and sizes. A HTF flows between these elements to transfer the heat to the storage material. Since the HTF is in direct contact with the storage material, heat transfer coefficients can be large. These systems can maintain the thermal gradient when very low conductive solid materials such as rocks/sands are used. By the utilization of solid storage materials and only one tank, cost of the system decreases when compared to the active two-tank systems (Bradshaw et al., 2002).

Handley and Heggs, (1969) formulated the mathematical equations to describe the transient heat transfer between the HTF flowing through a packed bed for the situations where there was resistance to heat transfer within the solid phase and thermal conduction in the solid phase along the direction of HTF flow. These equations were used to reveal a dimensionless group which predicted a dividing line between the Schumann model (1929) and the axial conduction (intra-particle) model for dimensionless bed length (> 4).

Ismail and Stuginsky, (1999) numerically investigated different thermal models suitable for sensible and latent heat TES systems. The models investigated are: continuous solid phase model, Schumann's model, single phase model and a thermal diffusion model. It was found that the model with a thermal gradient inside the solid particles seemed to consume more than twenty times the computational time required by Schumann's model for the simulation. Obviously, the use of the sophisticated model would be considered only when there is a need for detailed information within the solid particles.

Mawire and McPherson, (2009) simulated and validated experimentally the axial temperature distribution of an oil-pebble bed TES system under a variable heat source during charging process. Two models namely, the Schumann model and the modified Schumann model were simulated and compared with the experiment to find the thermodynamic behaviour of the TES system. The Schumann model was found to be in fair agreement with the experiment at lower TES temperatures. Large deviations between simulation and experiment were found at TES temperatures greater than 140 °C. The modified Schumann model was in closer agreement with the experiment at later stages of the charging process.

Mawire et al., (2009) used a simplified 1-D single phase model for an oil-pebble TES system to examine the thermal performance of three solid SHS pebble materials (fused silica glass, alumina and stainless steel). The thermal performance of these materials was evaluated in terms of the axial temperature distribution, the total energy stored, the total exergy stored and the transient charging efficiency. The results indicated that the amount of exergy stored and the degree of thermal stratification should be considered in addition to the value of the total amount of energy stored for the thermal performance of oil-pebble-bed TES systems. A high ratio of the total exergy to the total energy stored was suggested as a good measure of the thermal performance of the pebble material. From the simulation results, it was observed that the fused silica owns the best thermal stratification performance whereas stainless steel achieved the highest total energy stored. Alumina, on the other-hand, was found to have the fastest energy storage rate and had the best exergy to energy ratio variation during the charging process.

Dreissigacker et al., (2010) predicted the thermo-mechanical behaviour of storage under thermo-cyclic operation by using discrete element method. Initial simulation results include the temporal and spatial displacements as well as the forces acting on the individual bodies for a thermo-cyclic operation. These models were coupled by a term for the thermal expansion of the particles. It is observed that, the bed densification became apparent in the simulation results. The resulting temporal and spatial distribution of forces acting on particles and containment were determined and could be used as an input to stress analyses. Thus, the presented approach provided a good basis for a design tool that can identify low-stress solutions for packed bed TES systems in large scale installations.

Van et al., (2011) presented the modeling and solution of heat transfer and energy storage in a storage tank having a filler material. The method of characteristic was primarily applied to solve the governing equations numerically for predicting the heat charging/discharging process in the storage tank. Finally, design procedures using the numerical modeling tool, sizing procedures and other issues related to operation of a thermocline TES were discussed. The technique presented in this study dramatically reduced the computation time with more accurate results.

Xu, B. et al., (2012) presented the procedure to find the effective heat transfer coefficient between the solid and fluid for larger Biot number with different typical structures of solid TES material. These structures were a flat plate, a cylinder with HTF flowing longitudinally around it, and a tube where HTF flowed inside. It was found that the thermocline development and the corresponding effective discharging efficiency could hardly be influenced when increasing the inlet flow rate by ten times or changing the temperature difference of the molten salt from 50 °C–200 °C. This work provides a framework for interpreting the complicated thermocline behavior, optimizing the system configurations and operational strategies of the packed-bed molten salt thermocline system.

Xu, C. et al., (2012) developed a transient 2-D two-phase model for heat transfer and fluid dynamics within the packed-bed molten salt thermocline TES to investigate thermal behavior of a discharging process. The model was first validated based on the experimental results in the literature. It was used to numerically study the discharging process of the packed-bed thermocline system and evaluate the interstitial heat transfer coefficient, the effective thermal conductivity and effect of the thermal conductivity of solid fillers. The major findings from the study were that the thermocline region was moving upward with slight expansion and this could cover more than 1/3rd of the whole tank with its maximum thickness (i.e. at tank height, h =14 m). It was also found that decreasing the heat transfer rate between HTF and TES material or increasing the thermal conductivity of TES material, resulted an increase in the thermocline thickness which finally reduced the effective discharging time and its efficiency.

Zanganeh et al., (2012) tested a pilot-scale (6.5 MWh_{th}) TES system of rocks. Also, a dynamic numerical heat transfer model built for separate fluid and solid phases. The validated model was further applied to design and simulate an array of two industrial-scale TES systems of 7.2 GWh_{th} capacity each, for a 26 MW_e round-the-clock CSP plant during multiple 8 hr. charging/16 hours-discharging cycles with 95% overall thermal efficiency.

Cascetta et al., (2014) analyzed the transient behaviour of a packed bed TES (spherical particles of alumina) system using three different fluids (oil, molten salt and air). The analysis is based on a 1-D two-phase modified Schumann model. Oil and molten salt showed good performance even after continuous operations. However, after few cycles for air, energy storage capacity reduced significantly. Though oil and molten salt present important benefits, air allows a larger temperature range, with additional benefits such as wide availability and the absence of technical and environmental problems.

Klein et al., (2014) proposed a high temperature TES in randomly packed beds of ceramic particles as an effective storage solution for Solar Gas Turbine cycles. An experimental test program was successfully conducted to generate heat transfer data for a packed bed operating over the temperature ranges 350 °C–900 °C and 600 °C–900 °C. The fluid and solid temperature profiles in the packed bed were recorded in the axial and radial directions and were compared to a numerical model. The test data could be used by researchers wishing to validate their numerical TES models.

Wu et al., (2014) studied the impact of concrete structures on the discharging performance of the tank-type concrete TES system to replace the typical, packed-bed filler material. The typical concrete structures studied were: the channel-embedded structure, the parallel-plate structure, the rod bundle structure and the packed-bed structure. The packed-bed structure gave the best discharging performance, followed by the rod-bundle structure, the parallel-plate structure and the channel-embedded structure sequentially. The thermocline behaviors during the discharging process for the four structures with the influences of feature size and fluid inlet velocity were analyzed and the corresponding effective discharging time and efficiency were reported.

2.2.3 Rocks and sand

Rocks after crushing to rough sizes of around 5 cm and gravel or silica sand with an average grain size of 0.2–0.5 mm can be used as a storage media in a packed bed using air as the HTF. The rocks could be used directly in solar receiver to collect the solar thermal energy as they fall under gravity from the top in the solar receiver tower (Schlipfa et al., 2015). Hot/ cold air flows between the gaps of the storage media and heat it/gets heated during charging/discharging process. There is a large contact surface area available for heat transfer between the air and storage media which improves the heat transfer efficiency. Rocks are poor thermal conductors and there is a small contact area between rock pieces which minimizes the heat loss during storage. Rocks have advantages like being non–toxic, non–flammable, very cheap and easily available. However, few disadvantages include that they require large air mass flow rates and lead to larger pressure drops (Hanchen et al., 2011).

Shitzer and Levy, (1983) presented an analytical solution to the transient thermal behavior of a rock-bed TES system when subjected to varying air inlet temperature. Results of this solution were verified experimentally and compared to a numerical solution which was developed previously. Agreement in both these cases were very good.

Beasley et al., (1985) examined the transient thermal response of a rock bed with no net fluid flow during all-day charging under clear sky conditions. The experimental system consists of; air (HTF), a flow control system, a rock bed (0.357 m^3) for TES and solar field. Experimental measurements of the temperature distribution in the bed for a 13 hr stagnation period allowed a preliminary estimate of the losses in the available energy of the TES medium. The net loss in the thermodynamic availability was found to be 30 %. Preliminary results for the thermocline decay in a rock bed TES indicated that the natural convective motion of the fluid may occur in commercial scale systems. For systems where significant storage times were expected, the loss of thermodynamic availability during stagnation conditions should be considered in the system design.

Elsayed et al., (1988) designed an air-sand fluidized bed and tested for TES. Results were taken for the pressure and temperature along the cylindrical bed of diameter 30 cm and height varying in between 6–15 cm. Following three cases were considered, which were constant, linear time-dependent, and exponential time-dependent for supply temperature. The results were analyzed and concluded that the storage efficiency in the case of linear and exponential time dependent supply temperature was always less than that obtained with constant supply temperature.

Fricker, (1991) designed a natural rock heat storage bed using 555 steel containers stacked in 15×37, inside the main steel vessel. Atmospheric air at 400 °C was used as the HTF. The rock was arranged in the form of a pebble bed assuming 35% voids. He demonstrated that the storage unit produced a discharging air temperature almost similar to charging air temperature and also advised that the pebble bed with ceramic materials as a cost-effective alternative.

Meier et al., (1991) experimented to describe the transient behaviour of high temperature rock bed storage with air as HTF (150 °C – 550 °C). Model predictions and the experimental results obtained from the small thermal storage system ‘ARIANE’ were fairly good in agreement. The other parameters like temperature stratification, heat losses though the wall and the pressure drop were reproduced quite accurately.

Brosseau et al., (2005) studied the durability of filler (rock and silica sand) materials in molten nitrate salts over a range of operating temperatures by performing a series of isothermal and thermal cycling experiments. The experimental results showed that the quartzite rock and silica sand were able to withstand the molten salt environment quite well. No remarkable deterioration that would impact the performance or operability of a thermocline TES system was evident.

Zavattoni et al., (2014) proposed a high temperature rock-bed based TES system model by means of accurate 3D time-dependent CFD simulations (air as HTF). The thermodynamic behavior of the TES system was analyzed through 15 consecutive charge and discharge cycles to evaluate the thickness evolution of the thermocline zone, and hence the overall thermal efficiency of the system. They observed a porosity variation with the packed bed depth both in numerically and experimentally. This was mainly due to the own weight of the packing of the TES system.

Grirate et al., (2016) proposed six different rocks (quartzite, basalt, granite, hornfels, cipolin and marble) as filler material with direct contact of synthetic oil for testing the TES potential. These rocks were selected as the candidate TES materials according to their abundance to use in the CSP plants in the temperature range of 250 °C–350 °C. Based on the experimental results obtained, Quartzite and Cipolin were identified as good candidate TES materials to be used in direct contact with synthetic oil due to their chemical compatibility. This has been proved in support by the other research groups previously that quartzite behaves well as TES material (Agalit et al., 2015; Brosseau et al., 2005; Zanganeh et al., 2012). However, further testing of chemical interactions that could occur during direct contact between the materials chosen and the HTF was needed.

Jemmal et al., (2016) investigated the potential of gneiss rock as a low cost TES material for CSP plants. The obtained results proved the potential of this type of rocks in terms of high thermal capacities, high density and good thermal stability up to 550 °C. However, But, thermal cycling tests would be required to evaluate the durability of these rocks.

Jemmal et al., (2017) investigated the potential of two varieties of siliceous rocks namely, flint and quartzite (filler materials) in a packed bed TES system with air as the HTF to evaluate the thermal performance. Characterization experiments concluded that the quartzite (silica rocks) as the potential candidate TES material. Furthermore, these rocks were of low cost and environmental friendly. However, the presence of silanol (a functional group) in silica rocks is responsible for the rock degradation while cyclic thermal loads. Further specific heat treatment would be necessary to get rid of silanol.

Xu et al., (2017) tested sand saturated with thermal conductive fluid as a new low-cost TES material for better heat transfer rates. Also, they validated a 1- D transient enthalpy-based model for simulation of TES system. It was found that more energy could be stored and extracted if Hitec-saturated sand is used as the TES media, which might also reduce the cost when compared to the concrete TES based on a study for a 600 MW_e, CSP system in operation for a year.

The detailed summary of the above described literatures on packed beds of different storage materials, sizes and range of parameters of investigations by various researchers are reported in Table 2.1

Table 2. 1 The detailed summary on packed beds of different storage materials, sizes and range of parameters

Author(s) and Year	**Storage material/ Size/ Contributions/Remarks**
Furnas, (1930)	• Non-uniform solids of coal, coke, lime stones and iron ores • Small size • Gas temperatures up to 1100 °C for iron ores and below 300 °C for coke and coal
Colburn, (1931)	• Granular materials, pebbles, porcelain balls and zinc balls • A range of different small sized elements
Lof and Hawley, (1948)	• Gravel • 4.8–9.6 mm, 9.6–12.7 mm • Void fraction: 0.426–0.454; air temperature: 38–121 °C
Littman et al., (1968)	• Spherical particles of copper, lead and glass • 0.5–2.0 mm • Void fraction: 0.431–0.532
Standish and Drinkwater, (1970)	• Glass spheres; coke particles; ceramic rings • 16.7 mm; 22, 15.7, 9 mm; 12.7 mm • Void fraction: 0.41–0.59; Sphericity: 0.53–1.0
Chandra and Willits, (1981)	• Washed river gravel and crushed granite • 9.9–6.9 mm • Porosity range: 0.38–0.46
Coutier and Farber, (1982)	• Rocks • 18–30 mm • Bed diameter: 570 mm length: 840 mm; flow rate: 0.4–2.0 m^3/s • Developed a numerical model accounting for thermal losses and conduction. • Also elaborated a new calculation method for the volumetric convective heat transfer coefficient using the compared results of experimental tests and theoretical modelling.

Hollands and Sullivan, (1984)	• Thoroughly washed rocks • 8.02–16.8 mm • Void fraction: 0.31–0.48
Beasley and Clark, (1984)	• Soda lime glass spheres • 12.6 mm • Void fraction: 0.364; bed to particle diameter ratio 30 • Improved agreement with the predictive model is obtained when a Nusselt number correlation is used which is about 50% greater than current correlations. • The model is also verified by comparison with experimental data from a commercial size bed packed with natural rock.
M. Waked, (1986)	• Rocks • 20 mm, 25–50 mm • Void fraction: 0.36 and 0.47 • The major portion of the heat stored could be recovered (i.e. about 60%) at a temperature very close to the maximum storing temperature due to the temperature stratification along the pile axis • The remaining 20-30% of the stored energy could be recovered within a reasonable change in the temperature.
Sorour, (1988)	• Rock and gypsum • 12–30 mm • Influence of particle diameter, length of bed and flow rate on thermal performance of small SHES unit investigated.
Ammar and Ghoneim, (1991)	• Rocks and Egyptian clay called as ‘Tafla’ • 10–40 mm • Obtained optimum bed explicit parameters: 210 mm for bed length, 19 mm for particle diameter, 900 kg/h for mass flow rate and the charging time about 8 hrs. • Numerically optimized a SHS unit packed with spheres.
Audi, (1992)	• Limestone, Tar sand, Zeolite and Basalt • Small size

Sagara and Nakahara, (1991)	• Gravel, brick, concrete block and concrete U-shaped gutter • 42 mm for gravel, 130 mm for brick, 100 mm concrete block, 100 mm U-shaped gutter • Void fraction: 0.38 for gravel 0.30–0.67 for brick, 0.46 for concrete block, and 0.58 for U-shaped gutter.
El-Kassaby and Ghoneim, (1993)	• Natural soil • Small size • Stratified tank void fraction: 0.24
Al-Nimr et al., (1996)	• Rocks • 33.9 mm • Void fraction: 0.43
A. Jalalzadeh-Azar et al., (1997)	• Zirconium oxide pellets • 18.3 mm • 300 thermal cycle with an operating temperature span of 25–980 °C
Nsofor and Adebiyi, (2001)	• Zirconium oxide pellets • 18.3 mm × 18.3 mm • Void fraction 0.136; mass flow rate 100–610 kg/h.
Ozturk and Bascetincelik, (2003)	• Volcanic material • 54 kg/m^2 • 6000 mm × 2000 mm × 600mm packed bed filled with 6480 kg of volcanic material.
Singh et al., (2013)	• Spherical and cubical element of concrete masonry brick, tile brick and T-Joint • Large sized materials • Sphericity: 0.55–1.00; void fraction: 0.306–0.63; mass velocity: 0.155–0.266 kg/m^2.

2.2.4 Concrete as the SHS material

From the previous studies, it can be concluded that the commonly used 2-tanks molten salts TES system was the one with the highest environmental impact and therefore, should be substituted by any other system which has less environmental impact and are cost-effective. Concrete is a passive heat storage material promising a low cost, workable and easily available medium anywhere (Oro et al., 2012). It is an attractive storage medium due to its properties such as relatively high specific heat and thermal conductivity, good mechanical properties, thermal expansion coefficient similar to that of steel pipe and ease of obtaining and processing. Since it possesses good mechanical strength, it does not require a container to hold. It has no vapor pressure and leakage issues thereby no need of pressure containing vessels. Especially the wide range of possible working temperatures, the modular structure with optimized operation strategies make the heat storage in concrete attractive (Jian et al., 2015; Laing et al., 2008; Tamme et al., 2004). TES in solid state systems are the next generation of solar power plants which bring a substantial optimization in the energy production sector (Mazzucco et al., 2017). Laing et al., (2009) proved that concrete storage technology is a suitable option for storing sensible heat with the successful start-up and thermal cycling operations of the concrete storage test module.

Currently, the CSP systems cost about $ 13-17/kWh thermal. But, concrete TES has a low material cost and is reported to be $1/kWh thermal (Herrmann and Kearney, 2002). Several TES methods, improved HTFs and materials have been developed over the past two decades to reduce the cost of CSP systems. However, the efficiency of the storage unit can be improved by increasing the operating temperature, which in turn is limited by the materials used by Selvam and Castro, (2010). Finally, there are concerns for using concrete as the TES medium. During discharging process, the temperature of the storage medium decreases and hence, the HTF temperature also decreases with time, while thermal cracks are formed at high temperatures after repeated cycles of thermal expansion and contraction.

Hill et al., (1977) proposed a test method for determining the “effective capacity” and heat loss from storage device. Series of steady state tests were conducted to find the heat loss characteristics and eight transient tests to determine the effective capacity for both heat storage and removal. During transient tests the entering fluid temperature was charged in a step-wise manner and the amount of energy stored or removed over a specified test time was determined.

Tamme et al., (2003) developed a simulation tool for the analysis of the transient performance of solid media SHS systems. The influence of the various parameters describing the TES system were determined. It was observed that the distance between the flow channels exceeds a value of 0.08 m, a radial temperature difference in the storage medium taken place at the end of the charging process. This would reduce the storage capacity even if there are no thermal losses to the environment. Furthermore, selection of geometry of the storage system is more important than the effects of storage material properties.

Tamme et al (2004) used castable ceramic and concrete as the sensible storage material and simulated a rectangular storage unit of length 23 m containing 36 heat exchanger tubes with synthetic oil as HTF with a temperature range of 350 °C to 390 °C. They analysed the influence of thermal conductivity of the storage material on the storage temperature and it was worthwhile to develop materials with higher thermal conductivity at lower economic base.

Laing et al., (2006) investigated ceramic and high temperature concrete for maximum storage temperature of 390 °C and a storage capacity of 350 kW. They concluded that concrete is more preferable although ceramic has 20 % higher storage capacity and 35 % more conductive. It was also found that there was no degradation of heat transfer between the heat exchanger and storage material after 60 cycles.

Laing et al., (2008) tested solid media SHS systems with the three types of heat exchangers i.e., the tubeless, encapsulated and the tube register designs using synthetic oil as the HTF in the operating temperature range of 350 °C –390 °C. The tube register design with straight parallel tubes without additional structures had been identified as the best option to avoid the leaks of the oil, and also reduced high manufacturing and investment cost. Heat transfer enhancement technique inside the storage material had been implemented. It was proven that concrete storage technology is a suitable option as a SHS material and is also scalable from the kWh to GWh storage capacity range.

Guo et al., (2010) fabricated a new type heat storage concrete material by using aluminates cement, high heat capacity materials (basalt and bauxite) as aggregate, and added high heat conductivity graphite. The experimental results showed that the addition of graphite improved the value of thermal conductivity of the concrete up to 2.34 W/m-K. However, the compressive strength and flexural strength decreased with the addition of graphite.

Fernandez et al., (2010) described in a simple way to compare materials through bar chart where a certain property was plotted for all the families of materials. They studied the storage materials for long term storage and short term storage in the temperature range of 150-200 °C with the objective of minimizing the cost. The methodology allowed combining multiple objectives to evaluate materials for TES application.

Selvam and Castro, (2010) developed a 3-D FEM model to perform parametric studies during the charging/discharging of concrete by selecting different geometries of fins such as rods, plates, and disks attached to the HTF tubes. Results showed that the charging times were reduced by 19.4%, 37.0% and 58.6% for the cases of 8 rods, 4 disks and 2 plates, respectively.

John et al., (2010) examined the effect of heating rates on high performance concrete mixtures. The concrete mixtures with water to cementitious material ratios (w/cm) of 0.15 to 0.30 and compressive strengths of up to 180 MPa were cast and subjected to heating rates of 3, 5, 7 and 9 °C/min. Preliminary results consistently showed that the concrete mixtures without polypropylene fibers cannot resist temperatures beyond 500 °C, irrespective of the heating rate employed. These mixtures spall at higher temperatures when heated at a faster rate (7 °C/min). Additionally, mixtures which incorporate polypropylene fibers can withstand temperatures up to 600 °C without spalling irrespective of the heating rate.

Bai and Xu, (2011) presented a thermal analysis of a two-stage TES system using concrete and steam accumulator for discharging process, assuming linear pressure drop from 25 to 10 bar in one hour and a steam tank volume of 100 m^3. They concluded that higher thermal conductivity of concrete lead to more uniform temperature distribution in the concrete along radial direction and a higher steam temperature-rise along the tube, which in turn leads to high energy efficiency of the TES system.

John et al. (2011) developed seven concrete SHS models of different concrete proportions. They found that after exposure to 10 thermal cycles from ambient temperature to 723 K, six of the seven mixtures maintained more than 50 % of their mechanical properties.

Skinner et al., (2011) developed a laboratory scale high performance concrete with a single ¾ inch stainless steel pipe embedded in a 4 x 4 inch concrete cross section to test the thermal performance at a temperature of 450 °C–500 °C. Molten nitrate is used as the HTF. Also, they tested three different interface materials: Teflon tape, Deacon 8875 and aluminum foil in order to minimize the cracks caused from high tensile stresses between the concrete and stainless steel pipe. Results showed that the ‘Teflon’ tape produces the best heat transfer from the steel pipe to the concrete. Testing on a larger scale would be needed to ensure the complete viability of the technology.

Oro et al., (2012) analyzed the environmental impact of three different TES systems used in the CSP plants and they have been compared using Life Cycle Assessment (LCA) methodology. The LCA for the systems included: SHS both in solid (high temperature concrete) and liquid (molten salts) TES media, and LHS which uses PCM. The system based on solid sensible media showed the lowest environmental impact per kWh stored of all the three systems compared. In addition, the liquid media (molten salts) exhibited the highest impact per kWh stored, because it needed more material and complex equipment. Even though the energy storage capacity of the solid media was lower than the PCM systems, the global impact per kWh stored was the lowest, being the most environment friendly TES system.

Bindra et al., (2013) analysed the dynamic temperature response during cyclic storage and recovery of a packed bed accounting for wall heat transfer and intra-particle diffusion effects. They evaluated the exergetic performance of both sensible and PCM storage beds on the basis of parameters which influence axial dispersion, ambient heat losses and energy storage density. The results showed that the higher axial dispersion and higher ambient heat losses leads to lower exergy efficiency in SHS systems even at high energy density than the PCM storage systems under similar high temperature storage condition.

John et al., (2013) developed 26 economic concrete mixtures that resisted temperatures up to 600 °C and significantly reduced the unit cost of energy storage from $\$ 30/\text{kWh}_{th}$ to $\$ 0.88/\text{kWh}_{th.}$ It is to be noted that the unit cost of energy storage for molten salt is $\$ 4.50/\text{kWh}_{th}$. They recommended two mixtures (No.15 and 16) out of 26 proportions as they were inexpensive and their specific heat and thermal conductivity were high to maintain the stored energy for a prolonged period and to reduce the charging time.

Khare et al., (2013) demonstrated the material selection process to identify suitable SHS materials for high temperature (500 °C–750 °C) TES systems. Alumina, silicon carbide, high temperature concrete, graphite, cast iron and steel were found to be highly suitable for the above range. High temperature concretes such as high alumina cement-based materials and alumina-silicate geo-polymers were identified as potential and promising group of SHS media as they are cheap composite materials, provided their thermo-physical properties could be optimised for SHS by a suitable choice of aggregates, binders and additives.

Prasad and Muthukumar, (2013) developed a finite element based 3-D numerical model for investigating the transient behavior of a concrete SHS unit (capacity of 10 MJ) of cylindrical configuration with embedded optimized HTF tubes using Therminol 55 as HTF in the temperature range of 523 K–673 K. Employing three storage materials viz., concrete, cast steel and cast iron, predicted their heat storage characteristics. The charging times of concrete bed were 1307 s and 1187 s for cases having tubes with four and six fins. Although the performance characteristics of other materials are better than the concrete, they have not highlighted them due to its high costs and lack of readiness to avail.

Ozger et al., (2013) tested the effect of nylon fibres on the mechanical and thermal properties of hardened concrete for TES systems by comparing with the plain concrete. The heat capacity and conductivity at 300 °C of the fibre-reinforced concrete were 0.63 J/kg-K and 1.16 W/m-K, whereas for the reference concrete, the corresponding values were 0.81 J/kg-K and 1.02 W/m-K, respectively. They also found that the reference concrete exhibited a good thermal stability up to 450 °C with no spalling and the porosity left by fibres melting (at 160 °C) seemed to help in preventing the propagation of thermal cracks.

Bergan and Greiner, (2014) described a special type of inexpensive concrete that has significantly higher thermal conductivity than the normal concrete. The main component was quartzite, a natural geo-material readily available in many parts of the world. This TES technology was fully scalable from moderate temperature (100 °C) to high temperature (550 °C) applications and can be installed almost anywhere for several GWh_{th} storage capacity. Thousands of storage elements are compactly arranged within an insulated building (called as a NEST TES) which is fully scalable for several GWh_{th} storage capacity.

Skinner et al., (2013) tested concrete prisms in the temperature range of 400 °C –500 °C with molten nitrate salt as the HTF. During charging, significant cracking occurs in both the radial and longitudinal directions in the concrete prisms due to the hoop stress induced by the dissimilar thermal strain rates of concrete and HTF tubes. A 2D FEM was developed and used to study the stress at the prism/exchanger interface. Polytetrafluoroethylene (PTFE) and heat curing fibered paste (HCFP) were tested as interface materials to reduce the stress in the concrete. A heat exchanger with helical fin configuration was incorporated to improve the heat transfer rate in the concrete. Testing confirmed that the fins increased the rate of heat transfer in the concrete. However, large cracks formed at each of the fin locations. Only the HCFP was tested as an interface material for the finned heat exchanger. The HCFP decreased the number and size of the cracks, however not to the desired hairline levels. Also, PTFE induced better heat transfer from the heat exchanger to the concrete.

Jian et al., (2015) developed a one-dimensional unsteady model using the modified lumped capacitance method for a cylindrical solid TES system. A modular charging/discharging control strategy was proposed which could improve the utilization of the TES material. The control strategy using two modules could increase the TES material utilization from 33.4% to 38%.

Mirzanamadi et al., (2018) investigated the thermal properties of asphalt concrete both numerically and experimentally. A 2-D numerical model of asphalt concrete based on the FEM was developed and estimated the thermal properties of the asphalt concrete. The numerical model was validated by the experimental results using the Transient Plane Source (TPS) method. The experimental results showed that an increase in the ratio of the TPS sensor size to maximum aggregate size (preferably > 2) improved the accuracy in the measured thermal properties.

Montanes et al., (2018) developed a physical model of a 50 MW CSP plant using the modeling language, Modelica for analyzing and evaluating the TES concepts; and plant operation strategy. Results have been successfully validated against the reference plant key steady-state data. Furthermore, the performance of the plant has been evaluated during a typical summer day including the effects such as the variation of solar irradiation, charging/discharging the TES system and dumping excess heat in the solar field. The developed models could be used for steady state and dynamic simulations.

2.3 Combined TES Systems

Though the state-of-the-art in TES makes use of a 2-tank sensible heat storage, the use of multiple types of systems has more advantages. The combined sensible and latent heat storage system eliminates the difficulties experienced individually in the SHS and LHS systems to a certain extent and own the benefits of both the systems. For instance, a two-stage TES system was used in the 1 MW Dahan DSG power tower plant.

Generally, steam accumulator stores saturated steam at low temperature stage and during discharging, the saturated steam was converted to superheated steam with the help of a two-tank indirect storage system which uses oil as the storage medium (Xu et al., 2011). A thermal analysis of a two-stage TES system was carried out in which concrete was used in the high temperature heat storage stage and steam accumulator was used in the low temperature stage (Bai and Xu, 2011). Similarly, a three-part storage system was proposed by Laing et al., (2011), combining sensible and latent heat storage using thermal oil as the HTF for the temperature range of 300 °C –400 °C. Concrete (22 m^3 module) was used as the SHS material to preheat and superheat the steam. And, $NaNO_3$ with 140 kg (8.5 m^3 module) was utilized as the LHS material to evaporate water in DSG power plants. After 172 thermal cycles around the melting temperature of 306 °C, it was found that no degradation in the properties was detected. This sandwich concept enhanced the heat transfer, proving the expected capacity and power density.

Horn et al., (2004) studied an integrated solar combined cycle (ISCC) system both technically and economically. Both PTC field and volumetric air receiver tower were considered as solar systems. The solar LEC was 9.5 US¢/kWh for HTF-trough and 10.2 US¢/kWh for air-tower. The LEC for the reference combined cycle was 2.4 US¢/kWh. The project provided an environmentally beneficial and economically attractive option for renewable power generation.

Hosseini et al., (2005) assessed technical and economic performance of the Integrated Solar Combined Cycle (ISCC) Power Plants by choosing thermal efficiency, capacity factor, environmental impact, fuel, investment and operation and maintenance costs as the main parameters. The performance analysis showed that ISCC systems (67 MWe) solar field was the most suitable plan when compared to a combined cycle. The LEC of ISCC system was 10 and 33% lower than the combined cycle and gas turbine power plants, respectively,

Nallusamy et al., (2007) tested combined TES (sensible and PCM) for 10 MJ capacity. Spherical encapsulated paraffin of melting point 60 °C was used as the PCM and water as storage material as well as HTF. Experiments were conducted at various inlet HTF temperatures and mass flow rates with electric heater as constant heat source and active solar flat plate collector as varying heat source. In the case of constant heat source, effect of mass flow rate was not significant on the charging rate whereas in the case of varying heat source, effect of mass flow rate had a significant role to extract the energy from the collector which in turn affects the charging rate of the TES unit.

Nandi et al., (2012) presented a comparative analysis of high temperature SHS and LHS systems for a solar power plant of 50 MW capacity and six hours of storage duration. They reported that concrete and castable ceramic as low cost SHS materials and LEC is minimum for thermocline system.

Zanganeh et al., (2014) numerically simulated a new TES concept that added a layer of encapsulated PCM on top of a packed bed (rock) using 1-D heat transfer model. This concept was based on the combination of sensible and LHS by adding relatively a small amount of PCM to the top of the bed. The simulations showed that a PCM having 1.33% of total storage volume was sufficient to achieve stabilization of the outflow air temperature around the PCM’s melting point. The thermal properties of the PCM were found to have a strong influence on the behavior of the combined TES. The overall efficiency was not significantly affected by the addition of PCM.

Mazzucco, G. et al., (2017) analyzed the coupled behaviour of concrete including PCM ($NaNO_3$-KNO_3 binary mixture encapsulated within steel spheres) particles employed as solid energy storage media to assess the thermo-mechanical performances. The change in mechanical strength of such a material is analytically and numerically investigated both at room temperature and during charging process. 3-D FEM models were developed at the meso-scale level to represent the main concrete components to better describe the evolutionary process of thermal damage if occurs during the plant functioning.

Pantaleo et al., (2017) performed a thermo-economic analysis on a hybrid (solar-biomass) combined cycle power plant with 2-tank molten salt TES system to increase the capacity factor and reduce the variations in the plant's operating conditions. The thermodynamic modelling had been performed by selecting different CSP sizes, storage levels and biomass combustor operation modes. The performance analysis results showed that the higher global conversion efficiencies were obtained with CSP integration and the thermo-economic analysis results showed a higher Net present value (NPV) of the investment when integrating solar energy, due to the avoided biomass supply costs and the higher value of solar-based electricity.

2.4 Other materials

In addition to the above stated common materials which are in use, many researchers have used different new and hybrid materials, by-products and other modified material to reduce the storage material cost as well as to achieve enhancement in the thermo-physical properties.

Sragovich, (1989) analysed the transient behaviour of SHS material using magnesia. They reported that the HTF (air) outlet temperature increased with reduced tube diameter and that was because of increase in convection heat transfer inside narrower tubes. They further noticed that there was always a critical mass flow rate at which the outlet temperature of HTF drops suddenly and this critical value varies in the same fashion as tube diameter.

Gluck et al., (1991) developed a new hybrid material (composite salt/ceramic) TES concept for industrial and solar applications of high temperature systems in the shape of checker brick. Charging of the TES was done with the flue gas of a 200 kW-gas burner. The influence of checker brick geometry–specific heating surface, specific free cross area, channel diameter, channel form on the storage performance cycle time, discharge power, temperature profiles were also investigated.

Mawire et al., (2009) modelled a simplified one dimensional single phase model for examining the thermal performances of three solid sensible heat pebble materials such as fused silica, alumina and stainless steel. It was found that exergy stored should be given more importance than the energy stored. Also, it was concluded that alumina has the best exergy to energy ratio variation during the charging process.

Kumaresan et al., (2011) investigated the performance of a solar PTC integrated with a storage unit, consisting a TES tank of 230 L and Therminol 55 as the HTF. An increase in the temperature of Therminol 55 is observed during charging. They found the peak instantaneous efficiency by the PTC at 12:00 h is 62.5 % (at mass flow rate 0.1 kg/s, max. temperature of 116 °C) and observed more heat loss than heat gained, beyond 14:00 h. Hence, it is not recommended to use PTC after 14:00 h, to charge the tank. They also advised that the PTC should be located very close to the storage.

Navarro et al., (2012) have given the alternative low cost by-product materials for solid SHS systems. These materials have high energy density, medium conductivity and lower prices when compared with the solar salt (60 wt. % sodium nitrate and 40 wt. % potassium nitrate). For long term storage better performing options are WDF (by-products of steel), Cofalite, IB (by-product of Potash) and WRutF (derivative of ilmenite) having highest energy density and lower cost. For short term storage, are WDF, the Halite mineral, concrete, WRutF, Cofalite and IB. Of which WDF, IB, Cofalite and WRutF were cost effective for CSP power plants.

2.5 Closure of Literature Survey

From the literature survey, the following conclusions are made.

- Most of the researchers emphasized on the use of concrete as an effective SHS material but there is lack of works on the heat transfer enhancement in solid media storage, although feasibility study has been done.
- Various researchers explored the possibility of using cast steel as the SHS material. Nevertheless, there is lack of optimization on the number of HTF tubes in the TES bed based on the charging /discharging time. It is also important to note that for a-given geometry of SHS system, its heat transfer augmentation techniques need to be optimized.
- Even though considerable research work on the thermal modelling of SHS system have been reported in the literature, very less experimental and numerical study have been carried out using SHS systems with optimized embedded tubes.
- Several researchers developed numerous thermal models for studying the charging / discharging characteristics of SHS systems. But, majority of the developed models were based on simple heat exchanger configurations such as rectangular, spherical and tube-in-tube model. Very few models are developed on the multi-tube based shell-and-tube type configuration.

- Most of the heat-transfer enhancement techniques such as inclusion of different geometry of fins namely, rods, plates, and disks attached to the HTF tubes were numerically modelled in basic SHS systems such as tube-in-tube configuration.

Therefore, a detailed experimental work and numerical simulation with SHS optimized embedded tube design system is required for predicting the thermal performance of the system.

In view of the above closure of literature review, the following aspects are considered in the Ph.D. thesis work.

a) To study the charging/discharging characteristics of the lab-scale SHS prototypes using high conductivity solid material i.e. cast steel and a low conductive solid medium like concrete by considering the thickness of the HTF tube.

b) To optimize the geometry of different SHS models based on the minimum charging/discharging time.

c) To develop a 3D numerical model for predicting the charging/discharging characteristics of the SHS prototype with the optimized configuration and analyze the thermal performances at different operating conditions.

d) To study different concrete mix design grades and to fabricate the concrete prototypes by choosing the suitable weight proportion of concrete design mix

e) To evaluate the mechanical and thermal properties of the selected mix-design grade in order to predict the performance characteristics.

f) To design and develop a lab-scale sensible heat storage prototype of capacity 15 MJ

g) To test the performances of charging and discharging processes of the lab-scale SHS prototype at different operating conditions.

h) Validation of the numerical results with the experimental data.

2.6 Summary

In this chapter, a detailed literature survey on the various numerical models and experimental investigations on SHS systems and proportion of the concrete mix design M30 are presented. Several heat-transfer enhancement techniques implemented in the SHS systems are reviewed. The closure of literature survey is reported clearly. Finally, the core and minor objectives of the Ph.D. thesis work are framed and presented in sequence.

Chapter 3

Lab scale SHS Prototypes – Design and Fabrication

3.1 Introduction

In this section, the design and fabrication part of the three lab scale SHS prototypes are discussed in detail. The three lab-scale SHS prototypes tested in present study are

(i) Cast steel prototype (termed as M1)
(ii) Concrete prototype with copper finned tubes (termed as M2)
(iii) Concrete prototype with mild steel finned tubes (termed as M3).

The M2/M3 prototypes were filled with the tested concrete inside the shell side region of the prototypes. Hence, before filling the concrete in the shell side region of the prototypes M2/M3, proper sieving and mixing of the aggregates is highly recommended to fill in between the matrix of HTF tubes of the prototypes M2/M3. Various mix designs of the concrete mix have been tested with the help of cube (for compression strength) and cylindrical (for split tensile strength) moulds. Compression and split tensile strength are the two major mechanical properties for concrete structural design. The concrete material withstands the maximum load under the compression load and minimum in tension load.

Estimation of the concrete to fill inside the SHS beds, type of insulation and the material for the experimental set up, location of thermocouples (K-type) for capturing the temperature distribution inside the prototypes both in axial and radial, measurement of thermo-physical properties of the selected concrete mix design and the cyclic tests performed at the operating temperature range are also discussed in the following sections.

3.2 Lab scale SHS Prototypes

The design and configuration details of the SHS prototypes are listed in Table. 3.1. Fig. 3.1(a) & (b) shows the pictorial view of the M1 prototype without and with the thermocouples. Similarly, Fig. 3.1(c) & (d) shows the pictorial views of the M2 and M3 prototypes before filling the concrete. The copper and mild steel HTF tubes were integrated with five longitudinal fins of 10 mm height and 1 mm thickness. The concrete was filled uniformly in the shell region of the prototypes with the help of a vibrator. Fig. 3.1(e) & (f) shows the pictorial views of the M2 and M3 prototypes after filling the concrete.

Totally, nine K – type thermocouples were fixed in the storage prototypes (three thermocouples were kept radially at three different axial positions). The location details of the thermocouples fixed to the storage prototypes are listed in the Table 3.2. The corresponding positions are also shown schematically in Fig. 3.2. The thermocouples were fixed with a paste of alumina and sodium silicate gel for proper thermal contact and for later removal of the thermocouple.

3.3 Design of SHS prototypes

The major criteria to be considered in the design of a SHS system are its technical properties, economics and environment issues. Technical properties are the main elements to confirm the viability of a TES system. Economics is generally associated with the technical properties, because a higher storage capacity and a good heat transfer rate can considerably decrease the storage volume and hence, the storage cost (Tian and Zhao, 2013). The design of the SHS prototypes involves fixing the diameter and length of the storage prototype. The thermo-physical properties of cast steel, copper and mild steel are already listed in Table 5.2 (refer section 5.2). The major research gap found from the literature survey is the non-existence of SHS prototypes with multiple tubes incorporating heat-transfer enhancement techniques. Hence the main focus/novelty in this work is the development of SHS prototype with multiple embedded heat transfer tubes and fins.

Before designing the prototype, the outer diameter of the prototype -was planned to have above 0.3 m to accommodate two sets/layers of heat transfer fluid (HTF) tubes. As the development is on a lab-scale, 15 MJ storage capacity was fixed. Hence, due to these constraints, length is taken as 1 m. The design procedures of the SHS prototypes are given below:

- Decide the capacity of storage (Q). The storage capacity is 15 MJ in the present case.
- Fix the storage temperature range (ΔT = 60 K for M1, ΔT = 80 K for M2 and M3).

Table 3. 1 Configuration details of the SHS prototypes.

Prototype configuration	**L (mm)**	**D (mm)**	**n**	**n_f**	**Number of tubes in different PCDs**	**PCD (mm) Inner**	**PCD (mm) Outer**
M1	1000	267	19	-	1-6-12	110	220
M2	1000	324	22	5	1-7-14	130	260
M3	1000	324	22	5	1-7-14	130	260

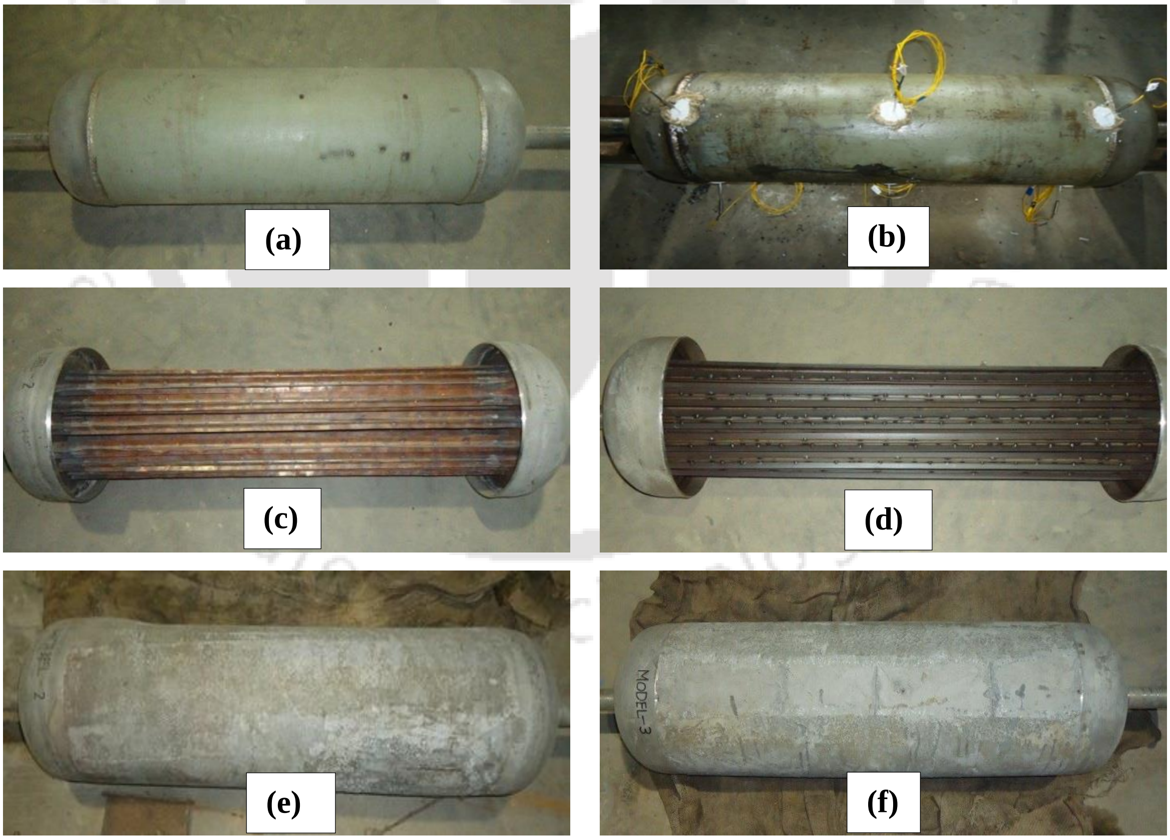

Fig.3. 1 SHS prototypes (a) M1, (b) M1 with thermocouples, (c and d) M2 and M3 before concrete filling, (e and f) M2 and M3 after concrete filling.

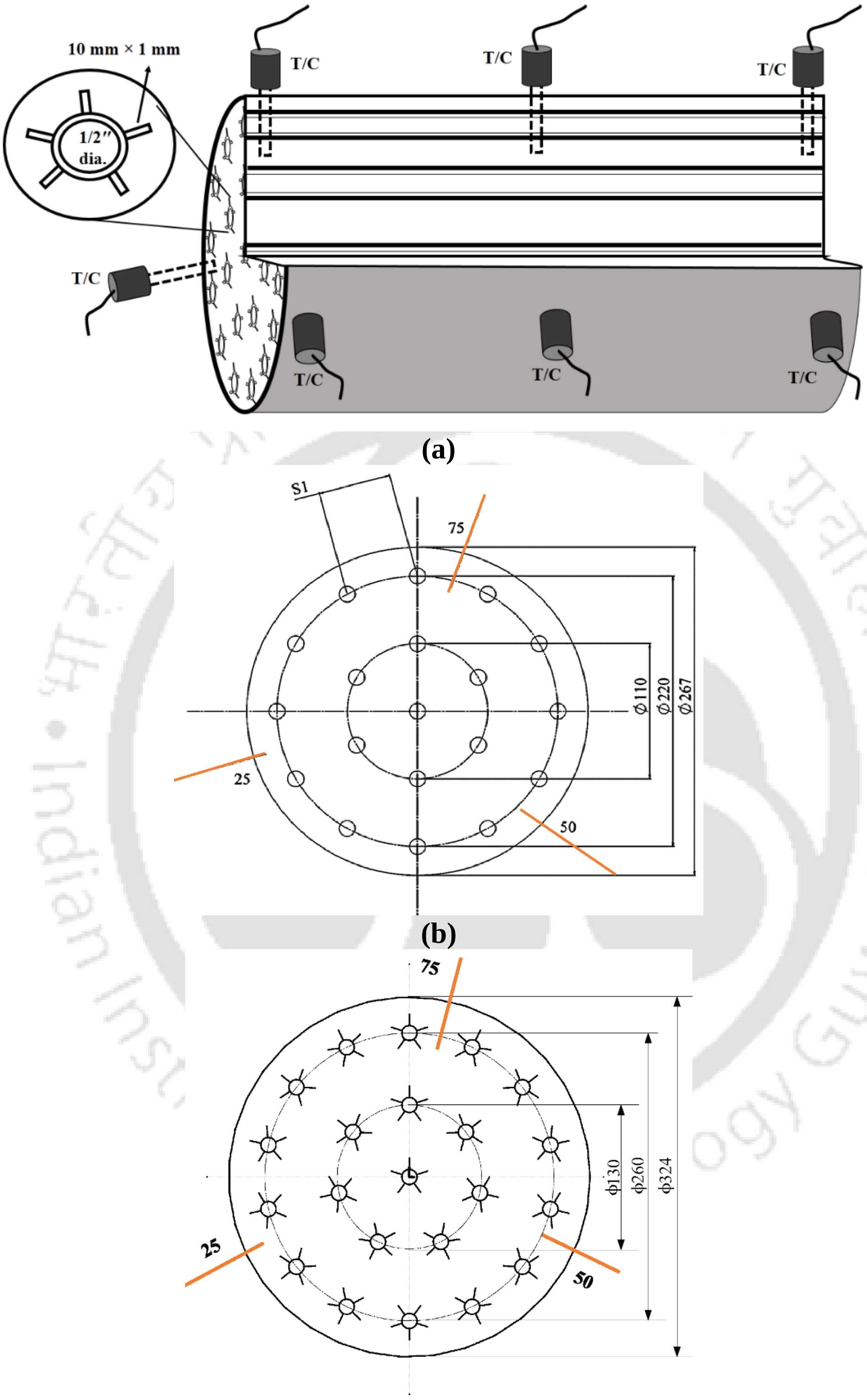

(a)

(b)

(c)

Fig.3. 2 Arrangement of the thermocouples in the storage prototype (a) isometric view of concrete, (b) cross-sectional view of tube arrangement cast steel and (c) cross-sectional view of tube arrangement concrete (all dimensions are in mm).

- Cast steel and concrete are chosen as the SHS material based on the mechanical properties, cost effectiveness (Nandi et al., 2012) and availability.
- The volume (*V*) of the SHS material needed is calculated using the Eq. (3.1).

$$Q=\rho_s V C_{ps} \Delta T \ \ (J) \qquad (3.1)$$

- Outer diameter and thickness of the HTF tubes are 0.0127 m and 1.5 mm, respectively.
- The diameter of the SHS prototypes is estimated using the Eq. (3.2).

$$V=\left[\frac{\pi}{4}(D^2-nd^2)-nn_{fin}bh\right]L \ \ (m^3) \qquad (3.2)$$

- Diameter (*D*) of the storage prototypes are found to be 0.267 m and 0.324 m for the cast steel (M1) and concrete (M2, M3) prototypes, respectively.

Table 3. 2 Thermocouples location details of the SHS prototypes.

Thermocouples	**Axial distance from any of the extreme ends (mm)**	**Distance from the periphery (mm)**
TC 1	40	25
TC 2	500	25
TC 3	960	25
TC 4	40	50
TC 5	500	50
TC 6	960	50
TC 7	40	75
TC 8	500	75
TC 9	960	75

3.4 Mix design for M2 and M3 prototypes

Many standard mix proportioning techniques are available for concrete mix designs. The mix proportioning technique adopted in the study is based on IS 10262-1982. But, addition of mineral admixtures and supplementary cementitious materials are not accounted in the present work. The concrete mix designs available as per IS 10262-1982 are named from M10 to M80 with multiples of 5. Based on the concrete characteristic strength, mix designs are graded as (i) Ordinary (M10–M20) (ii) Standard (M25–M55) and (iii) High (M60–M80) strength concrete. M10 and M15 are generally not used for structural applications. Admixtures are mostly added in the mix designs, M45–M80. Also, high strength concrete usage is limited due to the inverse variation between the strength and durability

(Reddy, 2012). Hence, five mix designs (M20–M40) were selected and test samples were prepared for the compression and tensile tests in the form of cubes and cylinders respectively.

The cost of the higher-grade concrete is generally more than the lower-grade concrete due to its higher cement content. Compressive load to cost ratio is an ideal parameter that considers both compressive strength and cost and hence, it is used for selecting the optimum mix design. The evaluated compressive strength–cost ratio of the selected mix designs are listed in Table 3.3.

Table 3. 3 Compressive strength–cost ratio of samples with different mix designs.

Mix Design	**C : FA : CA : W**	**F (kN)**				**cost $**	**F / cost kN / $**
		Trial 1	**Trial 2**	**Trial 3**	**Average**		
M 20	1 : 1.80 : 3.62 : 0.55	510	520	560	530	0.202	2623.7
M 25	1 : 1.66 : 3.42 : 0.52	600	650	670	640	0.243	2633.7
M 30	1 : 1.52 : 3.21 : 0.49	890	910	900	900	0.285	3157.8
M 35	1 : 1.38 : 3.01 : 0.46	1050	980	970	1000	0.327	3058.1
M 40	1 : 1.25 : 2.79 : 0.43	1100	1040	980	1040	0.361	2880.8

C: FA: CA: W represents the proportion of cement (C), fine aggregate (FA), coarse aggregate (CA) and water (W), respectively. From the test results, the compressive strength–cost ratio of M30 test sample was found to be the highest among the mix designs. Hence, concrete with the mix design M30 was selected to fill in M2/M3 prototypes and for further experimental study. The major parameters and the test data of the mix design M30 aggregates are given in Table 3.4. A detailed procedure of the mix design M30 followed during the preparation for the test samples and M2/M3 prototypes are given in Appendix. A.

3.5 Compression Test

Compression test was carried out by using compression testing machine by which the compressive force applied through a hydraulic actuator. Five mix designs (M20–M40 with multiples of 5) were selected and test samples were prepared in the form of cubes of side 150 mm for the compression test.

The cube is fixed in between upper and lower jaws of the compression test machine. Once the cracks are initiated in the sample, the strength values at that moment would be indicated by the rotating needle pointer and it stops its progress. The corresponding compression load tested values of the five mix designs (M20–M30) after curing in a water bath for 28 days are already listed in Table. 3.3 (see above section). The pictorial views of the concrete samples prepared for the compression test while testing is shown in Fig. 3.3. The weight of the each concrete cube after moulding is noticed about 9.92 kg of the selected Mix Design M30. Cube samples of all the respective five mix designs (M 20–M 40) after the compression test are shown in Fig.3.4.

3.6 Split tensile test

Split tensile test is conducted as per the ASTM C 496 recommended guidelines given in the procedure. ASTM C 496 is formed the basis for developing the split tensile test procedure. A diametral compressive load will be applied along the length of the cylindrical sample at a continuous rate until failure occurs. This loading induces tensile stresses on the plane containing the applied load, causing tensile failure of the sample. The samples were moulded with the dimension of 150 mm of diameter and 300 mm of height using the same proportion of mix design M30 for compression test. The pictorial views of the concrete samples prepared for the split tensile test while testing before and after 7, 28 days are shown in Fig. 3.5. From the images, it can be noticed that the plywood strips are along the length of each contact area. Each end of each plywood strip is aligned with the respective diametral line. The single-use pair of plywood with a length equal to the sample, width of 1 inch, and thickness of 1/8 inch are used in testing. The plywood strips are used to distribute the compressive load evenly at the contact surface of the sample. The load is applied through a hydraulic actuator. Once observed the pattern of fracture on the sample, the maximum load carried by the sample is recorded by the acquisition system. The tensile strength values of the four tested samples are given in Table 3.5. The splitting tensile strength will be determined by using Eq. (3.3).

$$\sigma_x = \frac{2F}{\pi DH} \tag{3.3}$$

Where, σ_x = split tensile strength (N/mm^2), F = maximum applied load at the time of failure (kN), D = diameter of the specimen (mm) and H = height of the specimen (mm).

Table 3. 4 Amount of several components of M30 concrete per cubic meter as per IS 383-1970.

Parameter	**Designed Value**
Nominal maximum size of coarse aggregate	10 mm
Water content including surface water	208 kg
Sand content with respect to absolute volume	40 %
Entrapped air with respect to absolute volume	3 %
Test data on Materials	
- Specific gravity of cement	3.02
- Specific gravity of coarse aggregate	2.72
- Specific gravity of fine aggregate	2.63
Degree of Workability	0.8 C.F

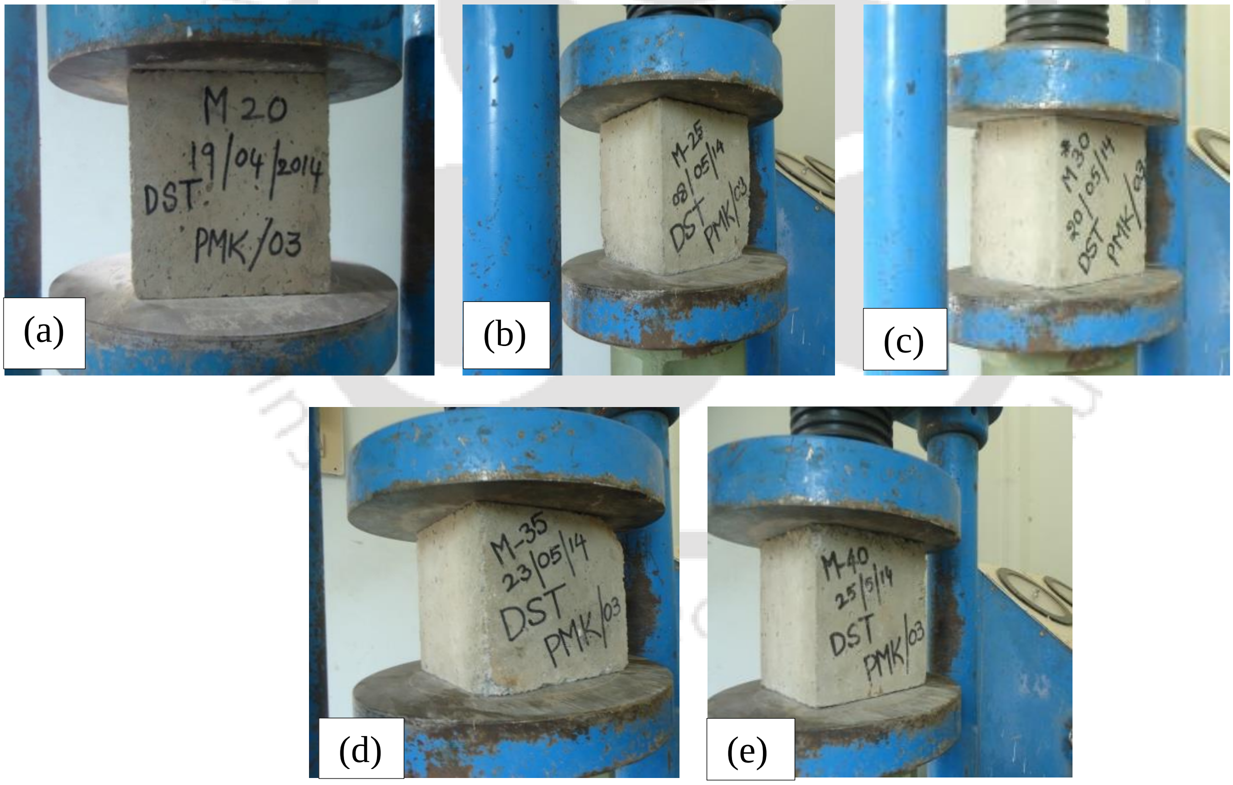

Fig.3. 3 Pictorial representation of the concrete samples under the compression test of design grades (a) M 20 (b) M 25 (c) M 30 (d) M 35 and (e) M 40

Fig.3. 4 Cube samples of five mix designs (M 20–M 40)
after the compression test

Fig.3. 5 Specimens before and after split tensile test (a & b) 7 days (c &d) 28 days

3.7 Estimation of concrete storage material for M2/M3 prototypes

Weight of the concrete components required as per IS 10262-1982, for mix design M 30 is given as follows:

- Volume of storage material with the longitudinal fins is estimated by using the eq.3.2. As per the mix design procedure followed (See Appendix. B), the estimated volume of the concrete storage material = 0.07849 m^3 (approx. 0.078 m^3)

- Weight of the concrete storage material = 230.789 kg.

3.8 Concrete filling of M2/M3 prototypes

The tube matrix design of lab scale M2/M3 prototype for the TES application is associated with optimised space to hold the storage material. Improper filling and poor contact of the concrete storage material with the HTF tube matrix will affect the storage characteristics significantly. Generally, concrete is filled in the well-designed structures easily. Hence, proper care has taken while filling the concrete ready mix. Cement, coarse and fine aggregates are mixed thoroughly in a concrete mixer as per the mix design M30 proportion listed in Table 3.3 of section 3.4. The mixed wet concrete is filled in the lab scale M2/M3 prototype. Metal sheet of galvanised iron (GI) is rolled circumferentially around the prototype so as to fill the concrete. For achieving good contact and compression between the concrete material and the HTF tube matrix, the vibrator is periodically operated. The arrangement of the concrete fill inside the M2 storage prototype is visualised in Fig.3.6.

Table 3. 5 Tensile strength of the concrete specimen

Strength after 7 days			**Strength after 28 days**		
Sample No.	Peak Load (kN)	Tensile strength (N/mm^2)	Sample No.	Peak Load (kN)	Tensile strength (N/mm^2)
S1	155.6	2.201	S3	242.8	3.434
S2	155.4	2.198	S4	255.6	3.616

3.9 Curing process of M2/M3 prototype

The basic idea behind proper curing is to allow a chemical reaction (hydration) between the finely ground cement particles and the water in the mix. While curing process, a suitable curing temperature was maintained which is usually 10°C to 30 °C. The concrete M2/M3 prototype was allowed for 28 days curing process by providing a sack over the circumference of the prototype for efficient water absorption. The concrete prototypes were kept wet continuously by wetting the surface after every 2 hours with water for 28 days. The pictorial view of the cured concrete model is shown in Fig 3.1 (e & f). A provision was made carefully for pilot holes at the time of concrete filling for inserting thermocouples inside the prototypes. This has been done to avoid drilling of the prototype after the curing process. This also avoids forming of micro cracks and poor contact between the HTF tube matrix and the concrete material.

Fig.3. 6 Arrangement of the concrete fill inside the M2 storage prototype on the Vibrator

3.10 Measurement of thermo-physical properties of concrete

The thermo-physical properties of concrete such as volumetric heat capacity and thermal conductivity were measured with the help of a thermal property analyser, Hot Disk TPS 2500 S. The thermal property analyser uses the transient plane source technique (Gustafsson, 1991; Suleiman, 2011) to measure the thermo-physical properties. The schematic representation of the thermo-physical property measurement setup and the arrangement of test specimens used are shown in Fig. 3.7(a & b).

The measurement setup consists of an isothermal bath, a monitoring unit and a power source in addition to the core TPS equipment. Silicon oil is used as the heat transfer medium in the isothermal bath. The TPS equipment is accommodated with flat double spiral sensors made of nickel enclosed by a polyimide film insulation, Kapton. Two concrete specimens of diameter 25 mm and length 20 mm were prepared for testing the thermo-physical properties at different temperatures. The pictorial view of the concrete specimens and the measuring sensor is shown in Fig. 3.8 (a&b). The Kapton sensor is kept between two test specimens in a sandwiched fashion during the experiment.

When an electrical current passes through the sensor, the temperature of the sensor increases and the heat flow from the sensor to the specimen happens at a rate depending on the thermal transport properties of the material. The thermal properties are manipulated based on the heat flow rate and it is given in the form of a thermal power output. The radius of the sensor, which is used for all the test specimens is 6.4 mm. The room temperature during the measurements was 300 K. The thermo-physical properties of the concrete specimens measured at different temperatures are listed in Table 3.6.

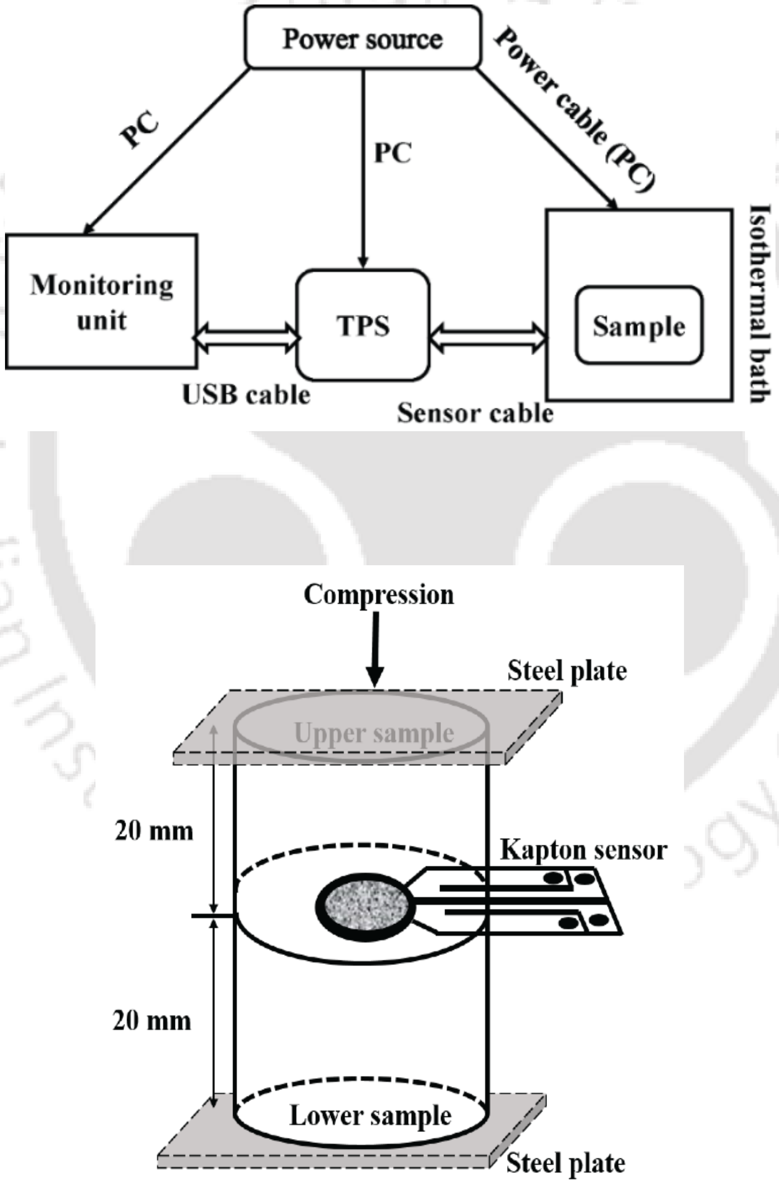

Fig.3. 7 Schematic diagram of (a) Hot Disk TPS 2500 S equipment with accessories and (b) test specimens arrangement.

Fig.3. 8 Pictorial view of (a) concrete test specimens and (b) Kapton sensor.

Table 3. 6 Thermo-physical properties of concrete at different temperatures

S. No.	**Temperature (K)**	$\boldsymbol{k_s}$ **(W m^{-1} K^{-1})**	$\boldsymbol{\rho_s \cdot C_{ps}}$ **(MJ m^{-3} K^{-1})**	$\boldsymbol{\alpha_s}$ **(mm^2 s^{-1})**
1	333	1.5193	2.352	0.646
2	353	1.4462	2.363	0.612
3	373	1.3739	2.375	0.579
4	393	1.3024	2.386	0.546
5	413	1.2309	2.398	0.513
6	433	1.1616	2.421	0.480

It is observed from Table. 3.6 that the thermal conductivity and diffusivity of concrete decreases and the volumetric heat capacity of the concrete increases with temperature. Similar trend of the property variation is also reported in the literatures Kodur and Sultan, (2003); Shin et al., (2002). The maximum uncertainty in the estimation of thermal conductivity, volumetric heat capacity and diffusivity are ±3 %, ±5% and ±3.5 % respectively.

3.11 Summary

In this section, the design and fabrication part of the three lab scale SHS prototypes are discussed in detail. Three lab-scale SHS prototypes tested in the present study are (i) cast steel prototype (termed as M1), (ii) concrete prototype with copper finned tubes (termed as M2) and (iii) concrete prototype with mild steel finned tubes (termed as M3). The following are the conclusions drawn;

- The mechanical properties of the mix design M30 (M2/M3 prototype) i.e., compression and split tensile strength are tested. From the results obtained, the compressive strength of the concrete mix design M30 specimens is acceptable, since the observed compressive strength is more than 20 MPa at 28 days. The average split tensile strength of the trails of concrete Mix Design M30 at the curing age of 28 days is increased by 60.28 % when compared to the curing age of 7 days.

- The thermo-physical properties of the concrete samples such as volumetric heat capacity and thermal conductivity were measured with the help of a thermal property analyser using the transient plane source technique. It is observed that the thermal conductivity and diffusivity of concrete decreases and the volumetric heat capacity of concrete increases with temperature.
- The maximum uncertainty in the estimation of thermal conductivity, volumetric heat capacity and diffusivity are ±3 %, ±5% and ±3.5 % respectively.

Chapter 4

Lab scale Prototype – Experimental Studies

4.1 Introduction

For any numerical model validation with the real – time experimental data is vital for the practical applicability and further refinement of the model. In this chapter, details related to the development of a shell-and-tube type lab-scale SHS prototype of 15 MJ capacity, with multiple embedded HTF tubes and the corresponding experimental results are presented. Longitudinal fins are adopted on the outer surface of HTF tubes for heat transfer enhancement. The dimensions of the longitudinal fin is 1000×10×1 of length, height and width (in mm) respectively. The novelty of the experimental work is the simultaneous implementation of two potential things considered for commercialization of storage technology: (i) higher storage capacity – multi-tube shell-and-tube type configuration and (ii) Heat transfer enhancement – longitudinal fins. Mix design of M30 grade is a mixture of cement, fine aggregate (FA), coarse aggregate (CA) and water in the weight proportion of 1:1.52:3.21:0.49. Various performance parameters such as charging, effective charging/discharging time, and energy storage/discharge rate are evaluated at different operating conditions. The axial and radial temperature variation of the storage prototypes (M1, M2 and M3) during the charging and discharging processes are also studied. These experimental results may be useful in designing the efficient industrial scale SHS systems, which have potential applications in solar thermal power plants.

4.2 Experimental setup

The schematic of the experimental setup for testing the thermal storage characteristics of the SHS prototype is shown in the Fig. 4.1. The entire system operates in a cycle, composed of a heat storage (charging) process followed by a heat removal (discharging) process. The experimental setup consists of oil storage tank, high temperature and low pressure oil circulation pump (5 HP, range: 1-2 bar), bank of electric heater (72 kW capacity), storage prototype, a positive displacement oval gear flow meter (± 0.2 % accuracy), K-type metal-sheathed thermocouples, a data acquisition system, cooling and expansion tank.

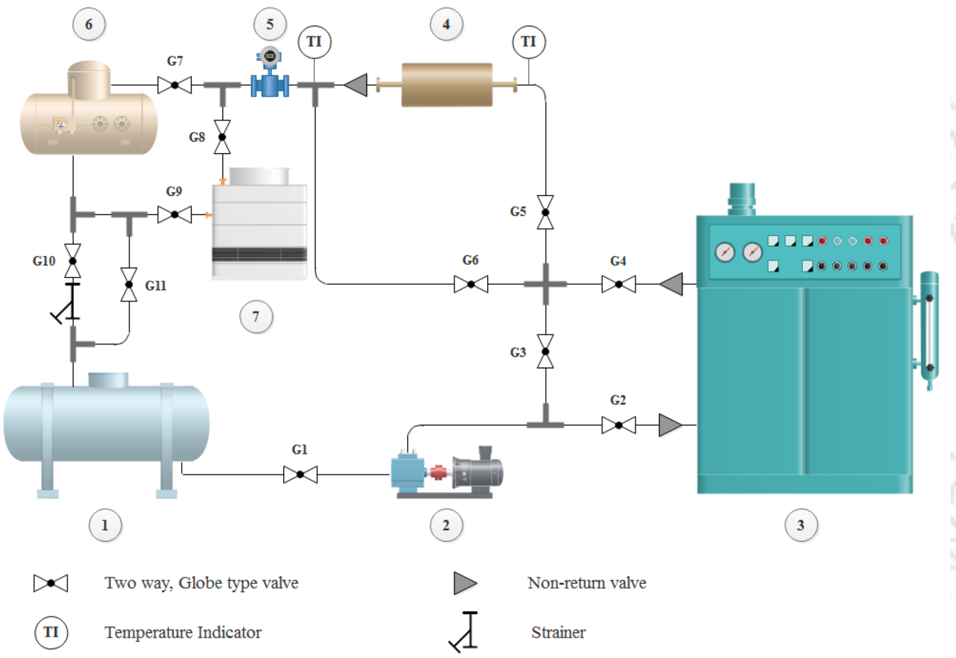

1 – Oil storage tank 2 – Thermic fluid pump 3 – Thermic fluid electric heater

4 – SHS prototype 5 – Oval gear flow meter 6 – Expansion tank 7 – Cooling tank

Fig.4 1 Schematic diagram of the experimental setup

The oil storage tank of 1000-liter capacity is utilized for storing the HTF. The huge storage capacity of the storage tank is mainly intended for storing the bulk heat, which aids in feeding a nearly constant temperature HTF to the SHS prototype. The HTF from the oil storage tank is pumped to the experimental circuit by a high-temperature thermic fluid pump of single-stage centrifugal and horizontal end suction type. The pump provides enough pressure to overcome the pressure drop across the thermic fluid heater/cooling tank, SHS prototype and pipeline. A variable speed drive (analogue frequency controller) is connected to the pump to achieve different flow velocities. The electric heater heats the HTF to the pre-set temperature during the charging cycle. The electrical load supply to the heater is tuned by a controller, based on the temperature difference between the desired HTF temperature and the heater-exit HTF temperature. The volume of thermic oil is generally increased while pre-heating/charging due to the thermal expansion. The excess volume needed to accommodate the hot oil is taken care by the expansion tank. In addition, the expansion tank de-aerates any gases if present in the thermic oil. A glass fluid level indicator connected adjacent to the expansion tank indicates the exact level of HTF present in the expansion tank.

The pilot holes were drilled at equidistant and equiangular (120°) regions from the outside surface of the prototype to fix the thermocouples. A detailed design and fabrication with the allocation of the thermocouples is explained later in the chapter 6. The SHS prototype, oil storage tank and the pipeline are insulated using glass wool of 50 mm thickness for avoiding heat loss to the ambience. The outer diameter of the fluid pipeline used in the experimental setup is about 48.3 mm (40 NB). The pictorial views of the experimental set-up before and after insulation are shown in Figs. 4.2(a) and 4.2(b), respectively.

The cooling tank used in the setup is a water based coil-type heat exchanger which is shown in Fig.4.3 (a). The cooling tank consists of 2 headers one each at bottom and top of cooling water tank with the capacity of about 1.73 m^3. The header was welded with threaded nipples of number16, based on the flow area of main pipe cross-section in coincidence with the sum of all 16 nipples flow area. These nipples are connected by half-inch flexible copper coil tubes with the help of ferrule for compression fitting. It was made sure that water cannot enter and mix with the HTF as the pressure inside the pipeline was being above the atmospheric pressure. The HTF flows through the copper tubes during the discharging process, and it is cooled down due to the heat transfer between the HTF and water. Single ported, Tee type globe valves (G1 – G11) and non-return valves are placed at the desired locations to control the HTF flow during charging and discharging processes. A strainer of Y-type is kept between the expansion tank and storage tank, to filter the circulating HTF from foreign particles if any.

The HTF used in the experiment is a synthetic oil (Hi-Tech Therm 60). The thermo-physical properties of Hi-Tech Therm 60 used for numerical as well as experimental tests at different temperatures are already given in Table 5.1 of section 5.2. Non-return valves of clapper type are used at certain locations

Fig.4 2 Experimental set-up to study the SHS prototypes (a) before insulation (b) after insulation.

of the fluid line, *viz.* inlet and outlet of the thermic fluid heater and outlet of the storage prototype, to prevent the backflow of HTF.The heating effect inside the thermic fluid heater is partitioned through three heating chambers. The heating chambers and arrangement of the heaters is shown in Fig.4.3 (b). During the experiment, temperature of the SHS prototype at various locations, HTF inlet and outlet temperatures and HTF flow rate are measured at a constant time interval of 1 s. A positive displacement flow meter of the oval gear type having an accuracy of ± 0.2 % is used to measure the HTF flow rate in the circuit. The temperature distributions with respect to time were measured with the help of specially designed metal sheathed K-type thermocouples (accuracy of ± 0.5 ºC and a time constant of 0.2 s) during the experimentation.

The temperature distribution of the storage prototype has been measured at nine locations of the SHS prototypes to account the axial and radial temperature variation. Two K-type thermocouples were fixed, each at the inlet and the outlet of the SHS prototype for measuring the HTF temperature. The thermocouples were connected to a 34970A, 20-channel multiplexer Agilent data logger (precision: ± 0.1 °C). The data acquisition system and the allied control equipment are shown in Fig. 4.3 (c). Concrete basements are made to place the oil storage tank, thermic fluid pump and heater firmly.

4.3 Experimental procedure

The entire experimental procedure can be subdivided into four processes, which should be carried out in sequence.

4.3.1 Preheating the oil – Storage prototype bypass

The HTF should be heated up to the desired HTF inlet temperature of the charging process. For achieving this, a bypass line is provided in the experimental loop so that the HTF recirculates without entering the SHS prototype. Valves G3, G6, G8 and G9 are closed during this process. Once the HTF reaches the desired inlet temperature for charging process, this process is said to be completed.

4.3.2 Charging

When HTF reaches the desired inlet temperature for charging process, the HTF is allowed to pass through the SHS prototype to initiate the charging process. Valves G4, G6, G9 and G10 are closed during this process. The process continues until the prototype is fully charged.

Fig.4 3 Experimental setup (a) water based coil-type heat exchanger, (b) the heating chambers and arrangement of the heaters and (c) model connected with thermocouple and data acquisition system.

4.3.3 Cooling the oil – Storage prototype bypass

Once the SHS prototype is fully charged, the HTF is then cooled down to the desired HTF inlet temperature for the discharging process. The HTF is made to flow through the cooling tank for achieving the same. Valves G3, G5 and G7 are closed during this process. Once the HTF reaches the desired inlet temperature for the discharging process, this process is said to be completed.

4.3.4 Discharging

When HTF reaches the desired inlet temperature for the discharging process, the HTF is passed through the prototype and thereby discharging of SHS prototype gets started. Valves G3, G5 and G6 are closed during this process. The process continues until the prototype is fully discharged.

Initially, the entire experimental setup is at room temperature (approximately 300 K). The HTF is first heated to the desired HTF inlet temperature of the charging process, which is termed here as HTF heating cycle. The charging cycle is said to be initiated when the average temperature of the prototype reaches the desired initial temperature of the charging cycle. The charging cycle is said to be stopped when the average temperature of the prototype reaches (or) 5 K lesser than the HTF inlet temperature. Now the HTF is cooled to the desired HTF inlet temperature of the discharging process, which is termed here as HTF cooling cycle. The discharging cycle is said to be initiated when the average temperature of the prototype reaches the desired initial temperature of the discharging cycle. The discharging cycle is said to be stopped when the average temperature of the prototype reaches (or) 5 K higher than the HTF inlet temperature. In order to investigate the performances of the SHS prototypes, both charging and discharging cycles are conducted at different HTF inlet temperatures and flow rates. The HTF flow patterns during the various cycles are given in Table 4.1.

Table 4. 1 HTF flow pattern during different cycles

S. No	**Cycles**	**HTF flow pattern**
1	HTF heating	G1-G2-G4-G6-G7-G10
2	Charging	G1-G2-G4-G5-G7-G10
3	HTF cooling	G1-G2-G4-G6-G8-G9-G10
4	Discharging	G1-G2-G4-G5-G8-G9-G10

4.4 Results and discussion

Charging and discharging experiments were carried out for the three SHS prototypes at different HTF flow rates and operating temperature ranges. Performance parameters such as charging/discharging time and energy stored/discharged were predicted. Except for parametric studies, the velocity of the HTF was maintained at 0.25 m/s throughout the experiments during both charging and discharging cycles. In this section, the results obtained from the experimental studies are discussed in detail. A theoretical model resembling exactly the fabricated prototype is also developed and thoroughly studied. Additional analysis made in the theoretical model is the evaluation of volumetrically averaged parameters such as temperature and energy storage/discharge rate.

The initial average temperature of the cast steel and concrete storage prototypes during the charging cycle was 353 K and comparatively higher temperature HTF at 413/433 K was allowed to pass through the tubes, which makes an initial temperature difference of 60/80 K between the cast steel/concrete prototype and the HTF inlet. The initial average temperature of the cast steel/concrete storage prototype during the discharging cycle is fixed at 413/433 K and comparatively lower temperature HTF at 353 K is allowed to pass through the tubes, which makes an initial temperature difference of 60/80 K between the cast steel/concrete prototype and the HTF inlet.

4.4.1 Charging/discharging time

The charging time of the storage prototype is one of the important parameters of performance evaluation as it is directly related to the storage characteristics of the prototype. Fig. 4.4(a) presents the variation of average temperature of the cast steel prototype. It is observed from Fig. 4.4(a) that the increase in temperature during the initial charging period (0–400 s) of the charging process is higher than the later period (400–1200 s). This is due to the availability of higher heat transfer potential during the initial period, which gets degraded over the period of time. The storage prototype is said to be fully charged when its average temperature reaches the HTF inlet temperature. The complete charging time of the M1 prototype is about 1246 s.

Discharging cycle is a vital part of the storage prototypes as the stored energy is released to the HTF. Fig. 4.4(b) presents the variation of average temperature of the cast steel prototype during the discharging cycle. It is observed from Fig. 4.4(b) that the decrease in temperature during the initial period (0–500 s) of the discharging process is higher than the later period (500–1800 s). This is due to the higher heat transfer potential available during the initial period, which gets degraded over the period of time. The storage prototype is said to be fully discharged when its average temperature reaches the HTF inlet temperature. The complete discharging time of the M1 prototype is about 1803 s.

4.4.2. Effective charging time/discharging time

Fig. 4.5(a) presents the variation of average temperature of the concrete prototypes (M2, M3). It is observed from Fig. 4.5(a) that the increase in temperature during the initial period (0–2500 s) of the charging process in both the prototypes is higher than the later period (after 2500 s). This is due to the availability of higher heat transfer potential during the initial period, which is reduced gradually over the charging period. The storage prototype is said to be effectively charged when its average temperature reaches 5 K less than the HTF inlet temperature. The effective charging time of the M2 and M3 prototypes are about 5210 s and 7160 s. It is also observed from Fig. 4.5(a) that the rise in the average temperature of the M3 prototype is slower than the M2 prototype. The effective charging time

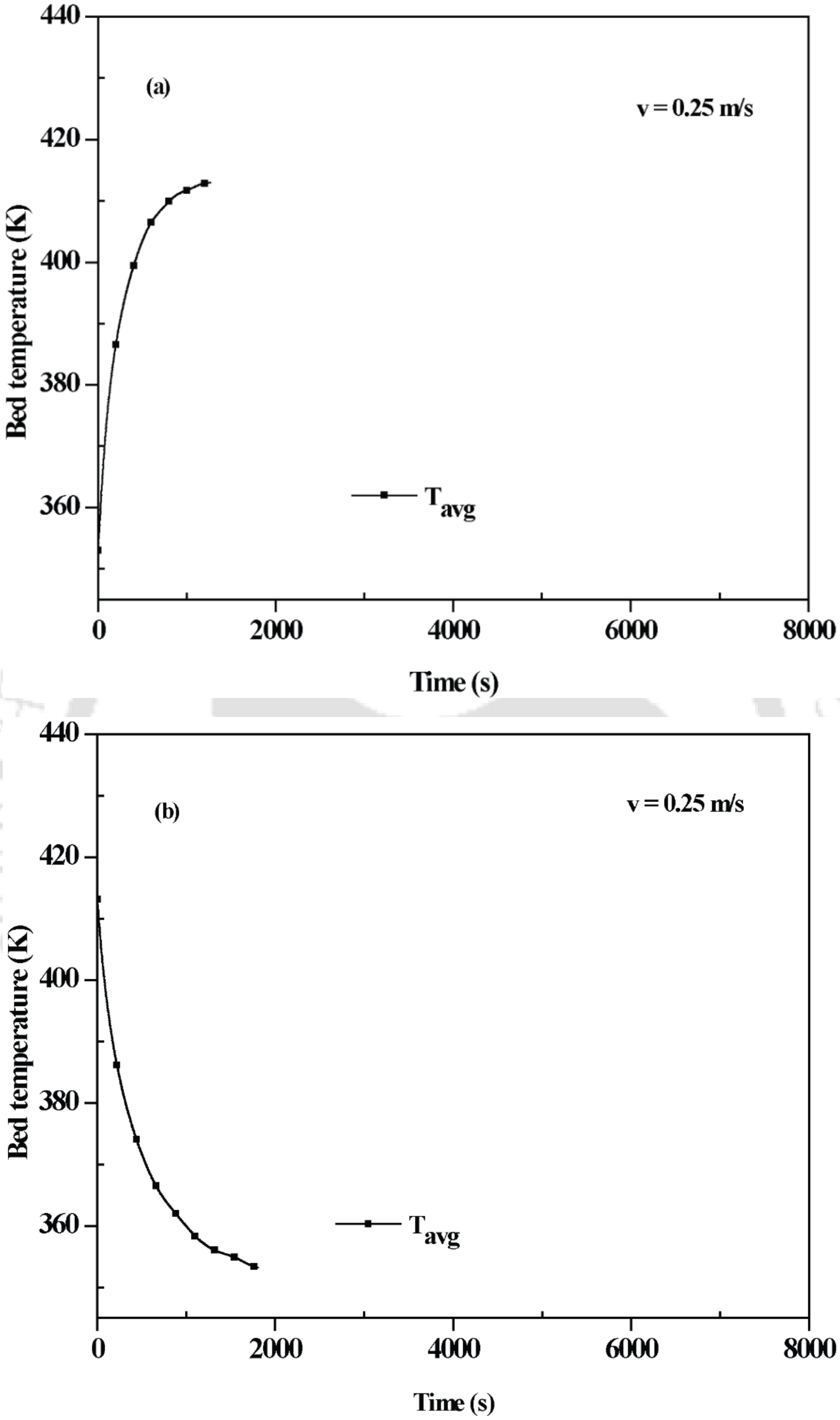

Fig.4.4 Temperature distribution of the storage bed M1 during (a) charging (b) discharging process

of the M2 prototype is lower by about 27.2 % than M3 prototype. This is mainly due to the higher thermal conductivity of the copper fins of the M2 prototype.

Fig. 4.5(b) presents the variation of average temperature of the concrete prototypes (M2, M3). It is observed from Fig. 4.5(b) that the decrease in temperature during the initial period (0–3500 s) of the discharging process in both the prototypes is higher than the later period (after 3500 s). This is due to the higher heat transfer potential available during the initial period, which is reduced over the period of time. The storage prototype is said to be effectively discharged when its average temperature reaches a temperature, which is 5 K more than the HTF inlet temperature. The effective discharging times of the M2 and M3 prototypes are about 6297 s and 7780 s. It is also observed from Fig. 4.5(b) that the decrease in the average temperature of the M3 prototype is slower than the M2 prototype. The effective discharging time of the M2 prototype is lower by about 19.1 % when compared with that of the M3 prototype. This is mainly due to the higher thermal conductivity of the copper fins of the M2 prototype.

4.4.3. Energy stored (Q_S)/discharged (Q_D)

Fig. 4.6 (a) shows the rate of thermal energy stored in the SHS prototypes. The amount of thermal energy stored in the prototypes at their respective charging time (or) effective charging time is estimated using Eq. (3.7). The amount of thermal energy stored in the M1 prototype at t_{ch} = 1246 s and T_{ch} = 413 K is 15 MJ. Whereas in the M2/M3 prototype, the amount of total energy stored at t_{ch} = 5210/7160 s and T_{ch} = 428 K is 14.06 MJ. The energy storage rate is faster for the M1 prototype, followed by M2 and M3 prototypes. This is due to the increased heat transfer dynamics of the M1 prototype when compared with the other prototypes. The uncertainties of energy stored in the cast steel and concrete prototypes are ± 0.66 MJ (± 4.43 %) and ± 0.56 MJ (± 3.98 %), respectively.

Fig. 4.6 (b) shows the rate of thermal energy discharged from the SHS prototypes. The amount of thermal energy discharged from the prototypes at its respective discharging time (or) effective discharging time is estimated using Eq. (3.8). The amount of thermal energy discharged from the M1 prototype at t_{dis} = 1803 s and T_{dis} = 363 K is 15 MJ. Whereas in the M2/M3 prototype, the amount of total energy discharged at t_{dis} = 6297/7780 s and T_{dis} = 358 K is 14.06 MJ. The uncertainties of energy discharged in the cast steel and concrete prototypes considering the uncertainties of all the independent parameters are ± 0.66 MJ (± 4.43 %) and ± 0.56 MJ (± 3.98 %), respectively.

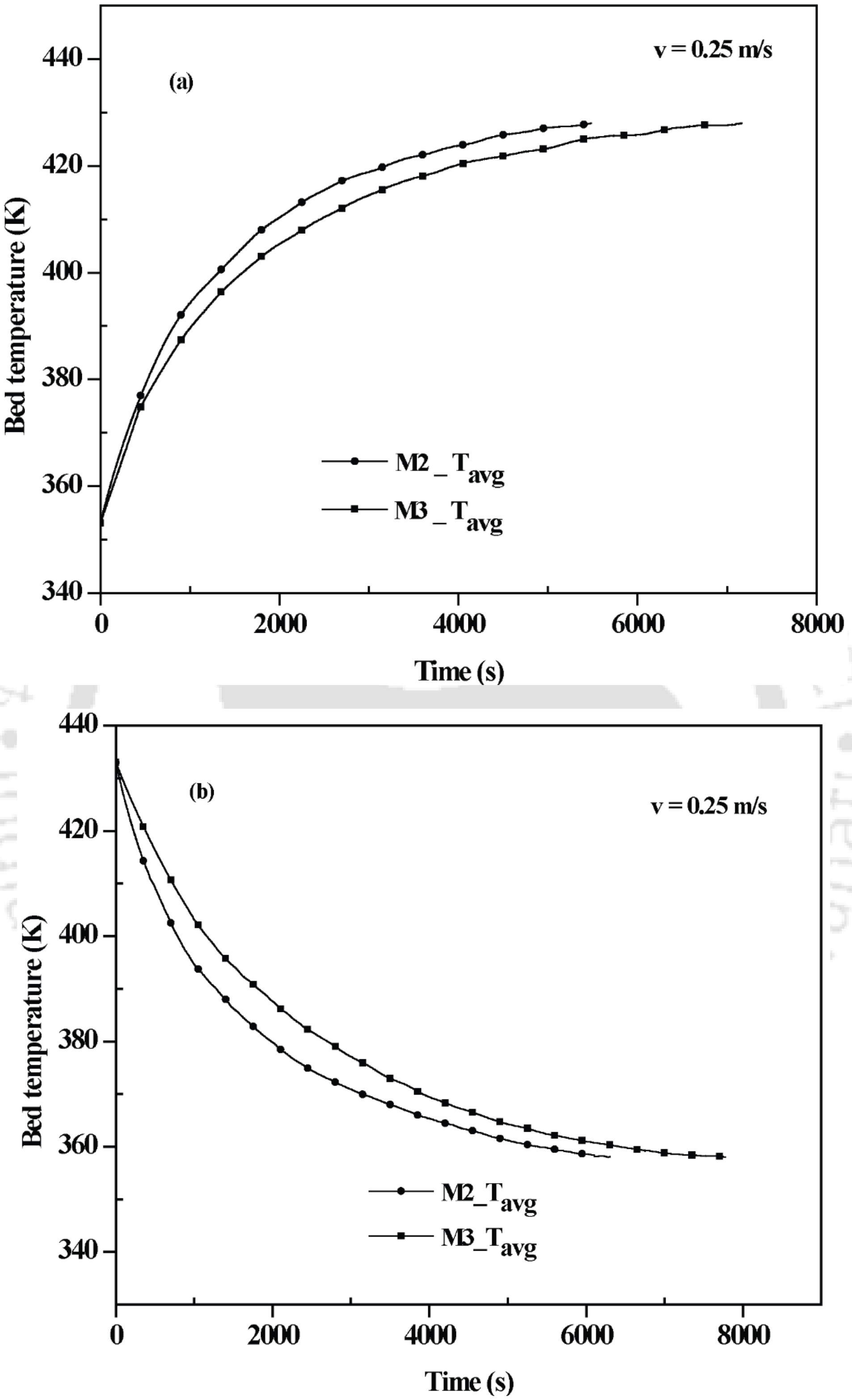

Fig.4.5 Temperature distribution of the storage bed M2 and M3 during (a) charging (b) discharging process

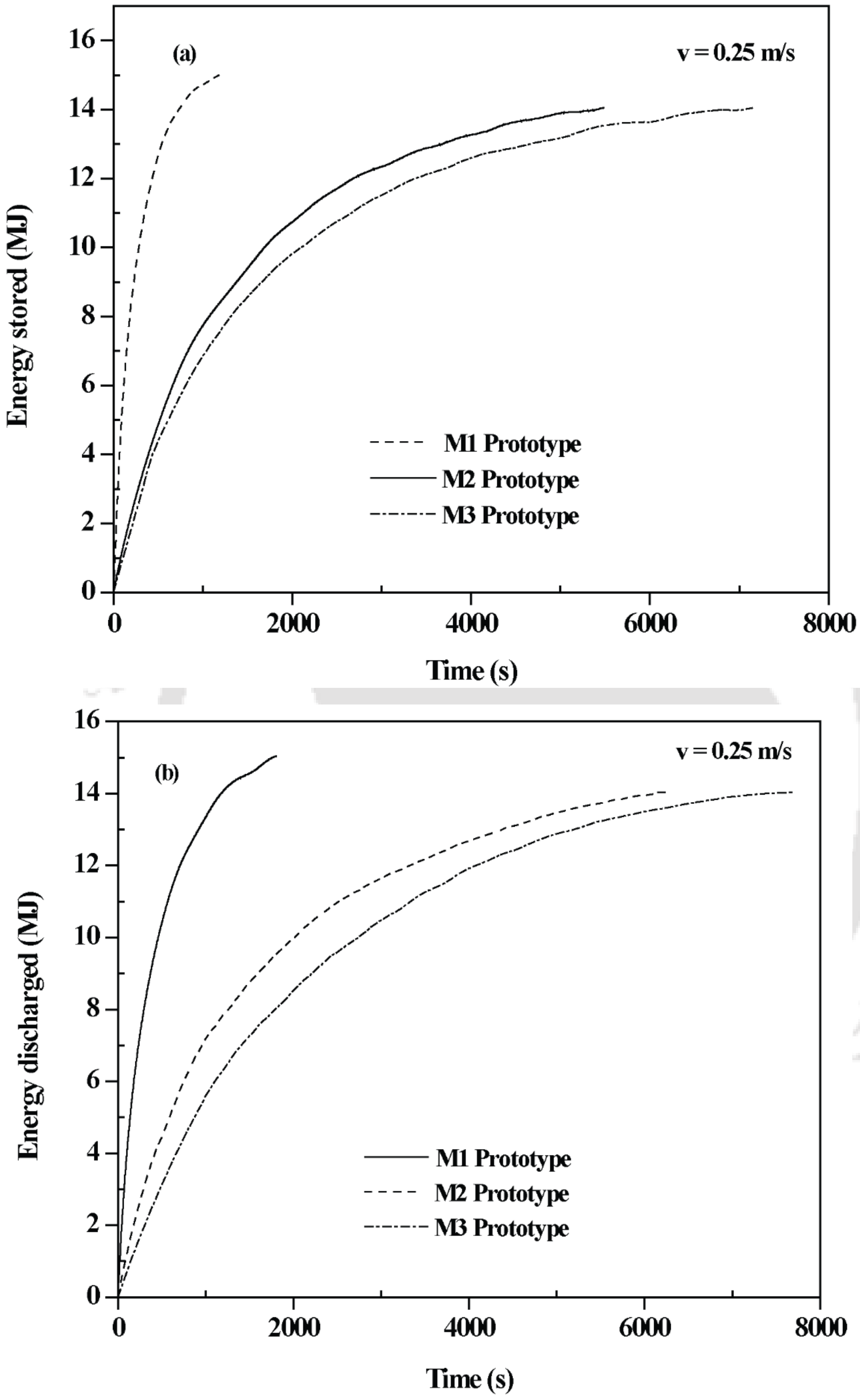

Fig.4.6 Variation of energy storage rate in M1, M2 and M3 storage prototypes during (a) charging (b) discharging process

4.4.4 Axial temperature distribution

Fig. 4.7(a) and (b) shows the axial temperature variation of the cast steel and concrete storage prototypes during the charging cycle. For showing the axial temperature variation, the temperature measured at three different axial locations (TC4, TC5, and TC6) are compared. It is observed from Fig. 4.7(a) and (b) that the temperature of the prototype in the entrance region is increasing at a faster rate than the exit region. This is due to the higher heat transfer potential available near the entrance of the prototype than the exit. It can be noted from Fig. 5.6(a) that the rate of temperature rise of TC4 is much higher than the TC5 and TC6 (M1 prototype). This is due to the high thermal conductivity of the cast steel by which a large temperature reduction is experienced by the HTF in the entry region of the prototype. However, similar effect is not observed in the concrete prototypes. It can be seen from Fig. 4.7(b) that the rate of temperature rise in TC4, TC5 and TC6 are almost similar. This is due to the low thermal conductivity of the concrete because of which the temperature reduction of HTF is low and the HTF is available at a higher potential (when compared with cast steel) in the middle and end sections of the prototype. With respect to the results obtained, the axial temperature variation recorded at three distinct axial locations is comparatively higher than the radial temperature variation (discussed in 5.4.5). In the case of prototypes having short length, the deviation between the axial temperatures would be very less. But that type of scenario is not encountered in the current analysis. Hence based on the above reason, the chosen length is also justified.

Fig. 4.8(a)-(b) shows the axial temperature variation of the cast steel and concrete storage prototypes during the discharging cycle. It is observed from Fig. 4.8(a)-(b) that the temperature of the prototype in the entrance region decreases at a faster rate than the exit region. This is due to the higher heat transfer potential available near the entrance of the prototype than the exit. It can be noted from Fig. 4.8(a) that the rate of temperature drop of TC4 is much higher than the TC5 and TC6. The reduction of HTF temperature in the entrance of the cast steel prototype is high due to the high thermal conductivity of the cast steel. However, similar effect is not observed in the concrete prototypes. It can be seen from Fig. 4.8(b) that the rate of temperature drops of TC4, TC5 and TC6 is almost similar. The HTF temperature reduction in the entrance of the concrete prototypes is low due to the lower thermal conductivity of the concrete and the HTF is available at a higher temperature (when compared with cast steel) in the middle and end portions of the prototypes.

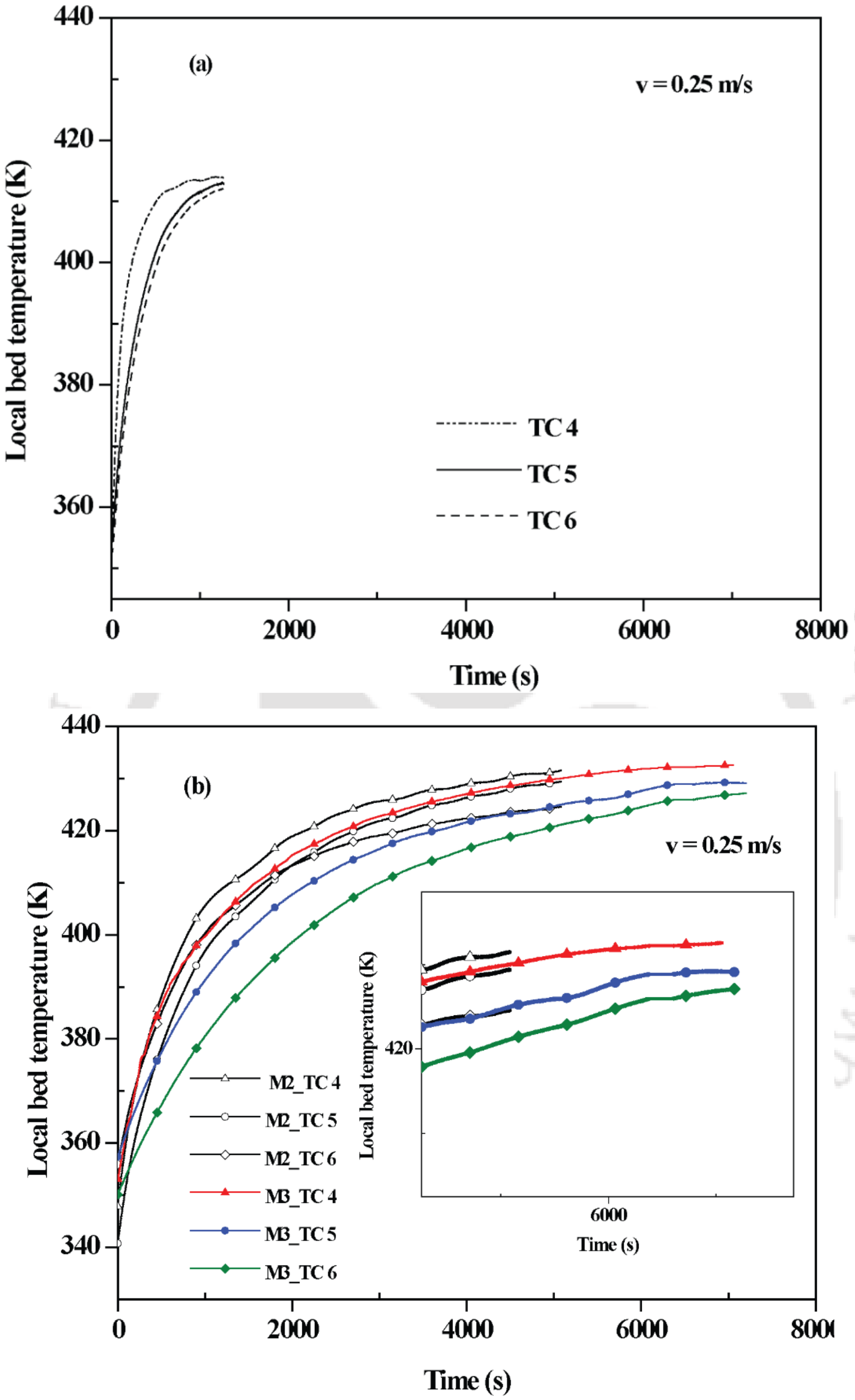

Fig.4.7 Axial temperature distribution of the storage prototypes (a) M1 (b) M2/M3 during charging process

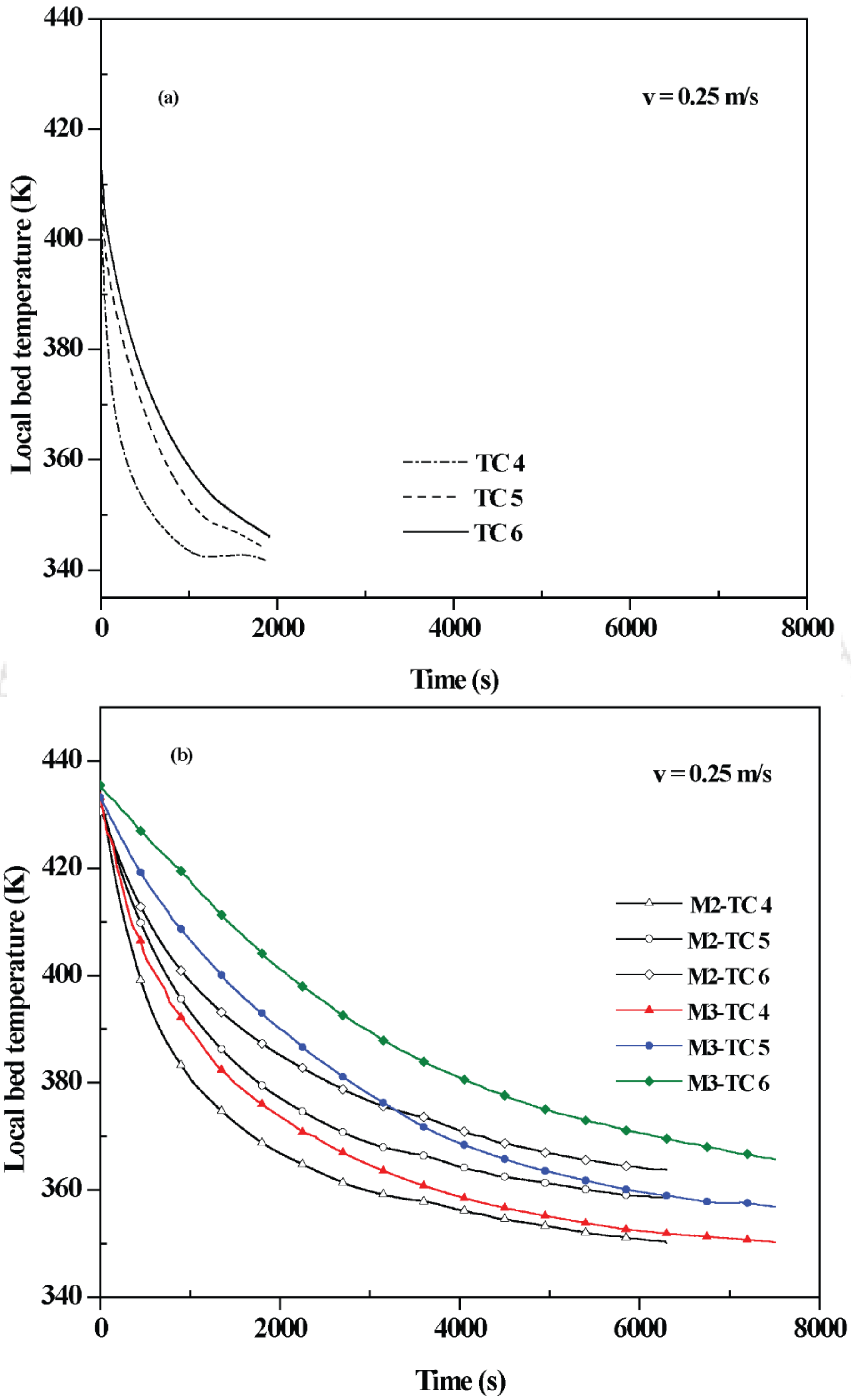

Fig.4.8 Axial temperature distribution of the storage prototypes (a) M1 (b) M2/M3 during discharging process

4.4.5 Radial temperature distribution

Fig. 4.9(a)-(b) shows the radial temperature variation of the cast steel and concrete storage prototypes during the charging cycle. For showing the radial temperature variation, the temperature measured at three different radial locations near the end of the prototypes (TC3, TC6, and TC9) are compared. Among the three thermocouples selected, TC9 is nearer to the HTF tubes/fins, followed by TC6 and TC3. It is observed from Fig. 4.9(a)-(b) that the temperature of TC9 is found to increase at a faster rate than TC6 and TC3 in all the prototypes. This is due to the higher heat transfer potential available near the HTF tubes/fins of the prototypes. It can also be noted that the difference between the temperatures measured at TC3, TC6 and TC9 is about 1/4 K in cast steel/concrete prototype. This is due to the higher thermal conductivity of the cast steel when compared to the concrete.

Fig. 4.10(a)-(b) shows the radial temperature variation of the cast steel and concrete storage prototypes during the discharging cycle. For showing the radial temperature variation, the temperature measured at three different radial locations (TC3, TC6, and TC9) are compared. It is seen from Fig. 4.10 that the temperature of TC9 decreases rapidly than TC6 and TC3 that is due to the higher heat transfer potential. It can also be noted that the difference between the temperatures measured at TC3, TC6 and TC9 is about 2.4/10 K in cast steel/concrete prototype.

4.4.6. Effect of HTF velocity

Fig. 4.11(a)-(b) shows the effect of HTF velocity on the charging rates of cast steel and concrete storage prototypes during the charging cycle. For showing the effect of HTF velocity, the average temperature of the storage prototypes for three different velocities (v = 0.1, 0.25, 0.50 m/s) are compared. It is observed from Fig. 4.11(a)-(b) that the average temperature of the prototype at higher HTF velocity increases at a faster rate than the lower HTF velocity cases. This is due to the higher convective heat transfer coefficient available in the higher HTF velocity case. The charging time of the M1 prototype for the velocities of 0.1 m/s, 0.25 m/s and 0.5 m/s are 2786 s, 1246 s and 1039 s, respectively. The decrease in charging time of the storage prototype with the HTF velocity of 0.25 m/s when compared to 0.1 m/s is 55 %. Whereas, the decrease in the charging time with HTF velocity of 0.5 m/s when compared to 0.25 m/s is 17 %. The effective charging times of the M2/M3 prototype for the velocities of 0.1 m/s, 0.25 m/s and 0.5 m/s are 5562/7820 s, 5210/7160 s and 5090/6865 s. The magnified graph inside Fig. 4.11(b) gives the clear picture about the variation of the temperature distribution of the concrete prototypes for the different velocities.

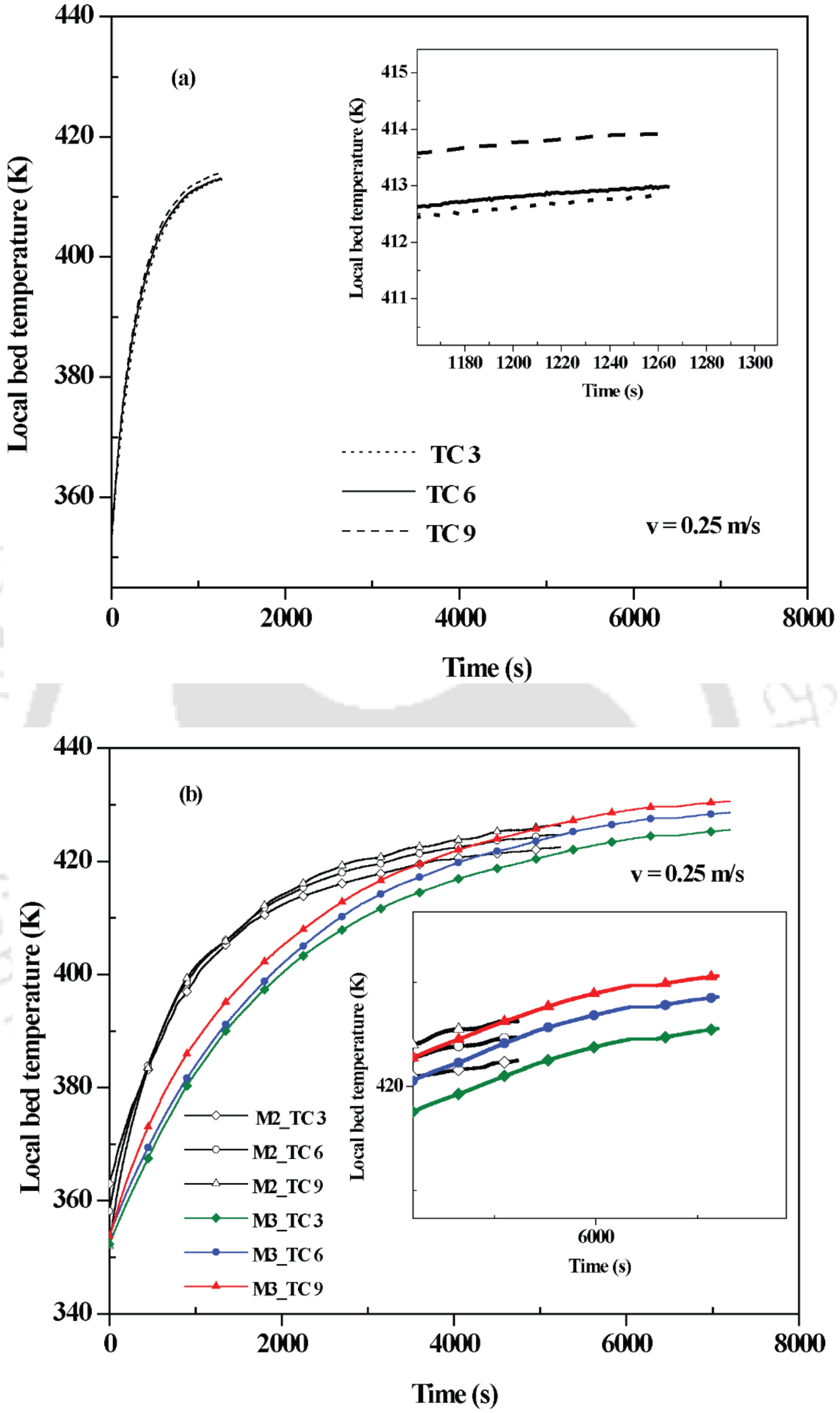

Fig.4.9 Radial temperature distribution of the storage prototypes (a) M1 (b) M2/M3 during charging process

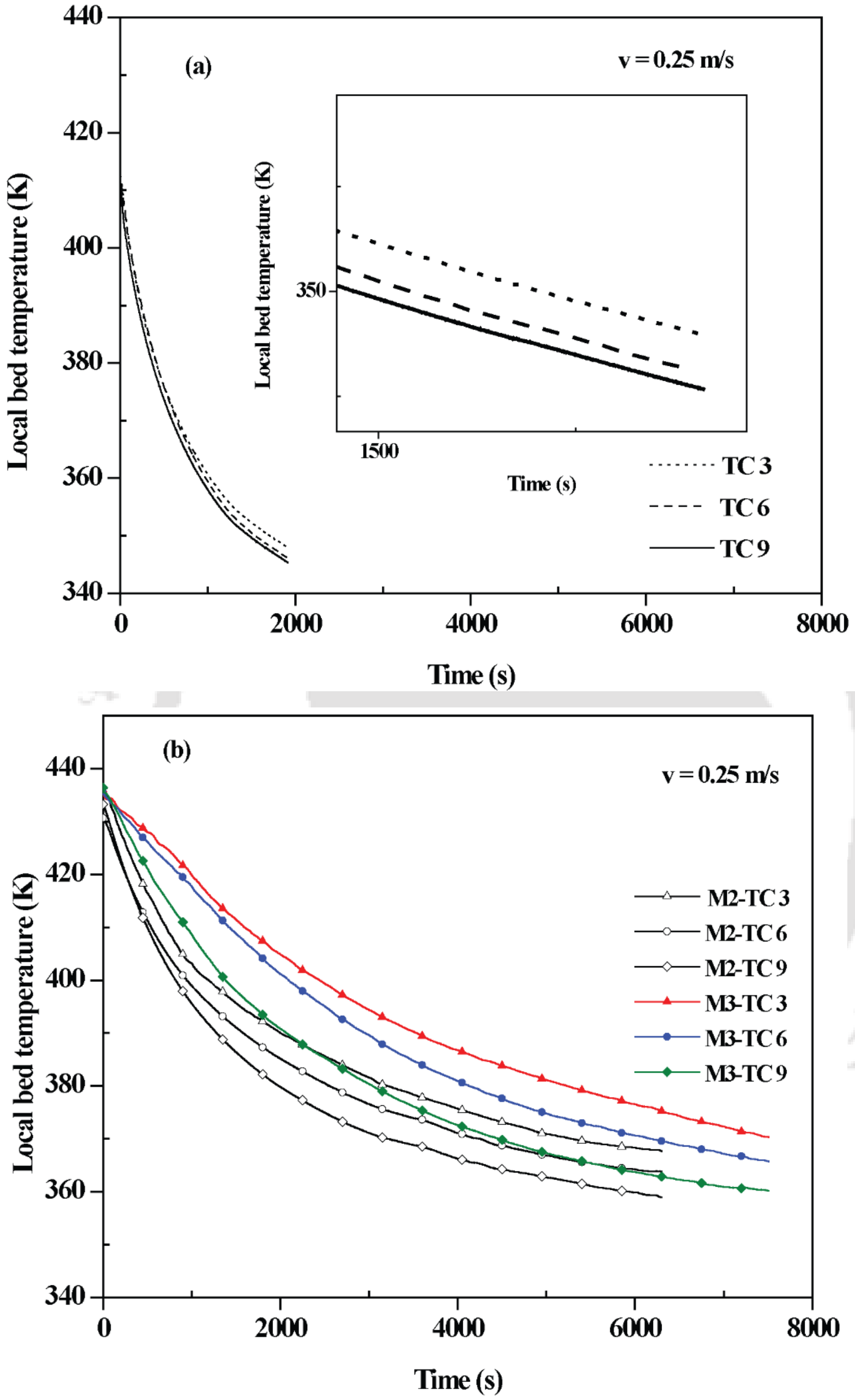

Fig.4.10 Radial temperature distribution of the storage prototypes (a) M1 (b) M2/M3 during discharging process

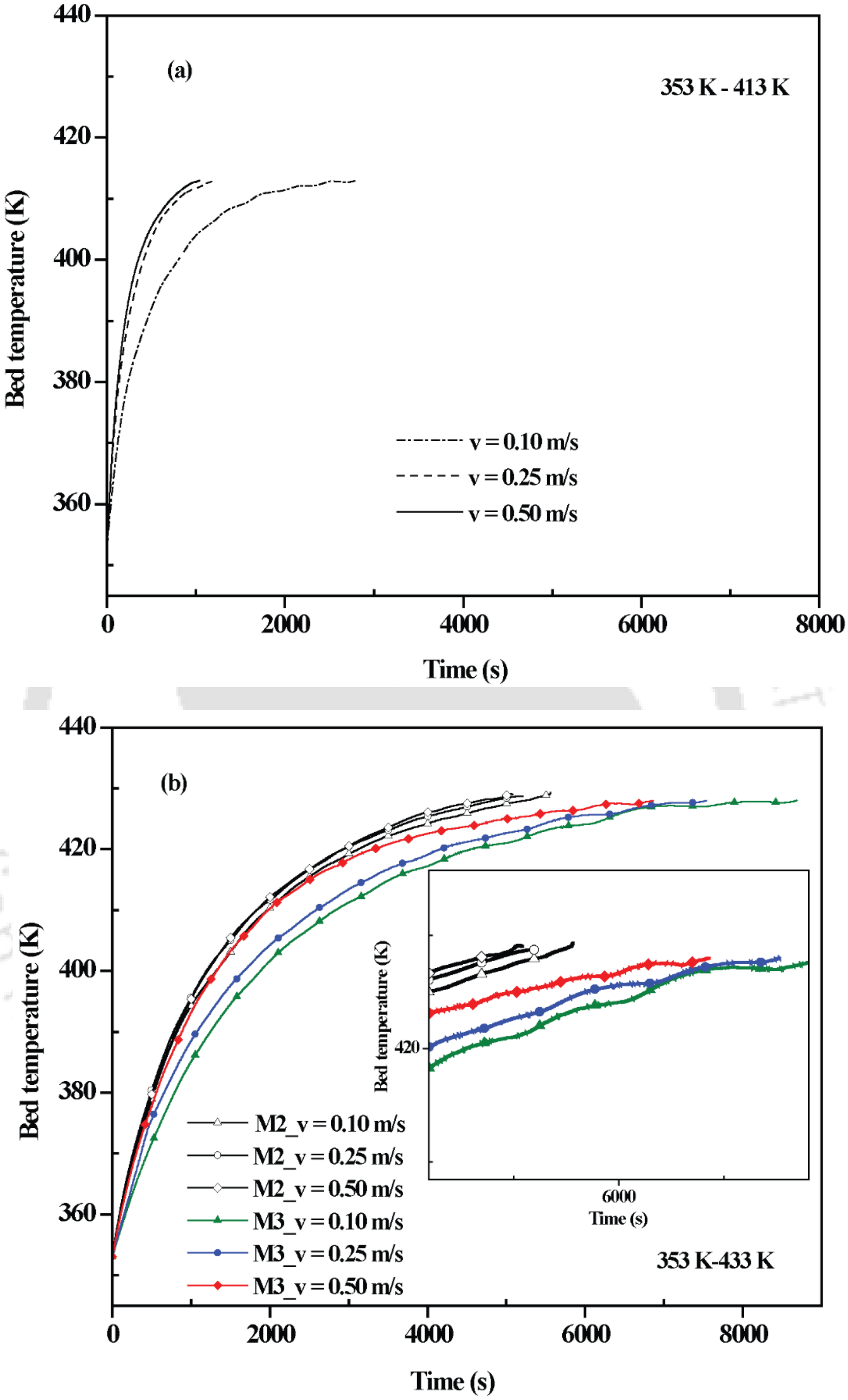

Fig.4.11 Effect of HTF velocity on the charging rate during charging cycle (a) M1, (b) M2 & M3.

Fig. 4.12(a)-(b) presents the effect of HTF velocity of the cast steel and concrete storage prototypes during the discharging cycle. It is observed from Fig. 4.12(a)-(b) that the average temperature of the prototype at higher HTF velocity decreases at a faster rate than the lower HTF velocity cases, which is due to the higher convective heat transfer coefficient available in the higher HTF velocity case. The discharging time of the M1 prototype for the velocities of 0.1 m/s, 0.25 m/s and 0.5 m/s are 3992 s, 1803 s and 1413 s, respectively. The decrease in discharging time of the storage prototype with HTF velocity of 0.25 m/s when compared to 0.1 m/s is 54.8 %. Similarly, the decrease in the discharging time of the storage prototype with HTF velocity of 0.5 m/s when compared to 0.25 m/s is 21.6 %. The effective discharging times of the M2/M3 prototype for the velocities of 0.1 m/s, 0.25 m/s and 0.5 m/s are 6722/8511 s, 6297/7780 s and 6076/7510 s.

4.4.7 Effect of operating temperature

The operating temperature range of the storage prototype also influences the performance of the system due to the temperature dependence of the thermo-physical properties of the storage prototypes and the HTF. To study the effect of the operating temperature range, three different temperature ranges (T_{ini}-T_{inlet}) are selected for the prototypes, viz., 343-403 K, 353-413 K and 363-423 K for the M1 prototype and 333-413 K, 343-423 K, and 353-433 K for the M2/M3 prototypes. Fig. 4.13(a)-(b) shows the effect of operating temperature range on the charging rate of cast steel and concrete storage prototypes. It can be observed from Fig. 4.13(a)-(b) that the charging times of all the prototypes are found to increase (about 10 %) at higher operating temperature range. The charging times of the M1 prototype in the three above-mentioned temperature ranges are 1168 s, 1246 s and 1301 s. The effective charging times of the M2/M3 prototype in the corresponding temperature ranges mentioned above are 4722/6988 s, 4950/7069 s and 5210/7160 s, respectively. This is due to the decrease in the thermal conductivity of the cast steel and concrete (see Table 6.6 in chapter 6) with the temperature and increase in heat loss to the ambient at higher operating temperature ranges.

To study the effect of the operating temperature during the discharging cycle, three different temperature ranges (T_{ini}-T_{inlet}) are selected for the prototypes, viz., 403-343 K, 413-353 K and 423-363 K for the M1 prototype and 413-333 K, 423-343 K and 433-353 K for the M2/M3 prototypes. Fig. 4.14(a)-(b) shows the effect of operating temperature of the cast steel and concrete storage prototypes on the discharging rates. It can be observed from Fig. 4.14(a)-(b) that the discharging times of the all the prototypes are found to increase at higher operating temperatures, similar to the charging process. The discharging times of the M1 prototype in the three above-mentioned temperature ranges are 1696

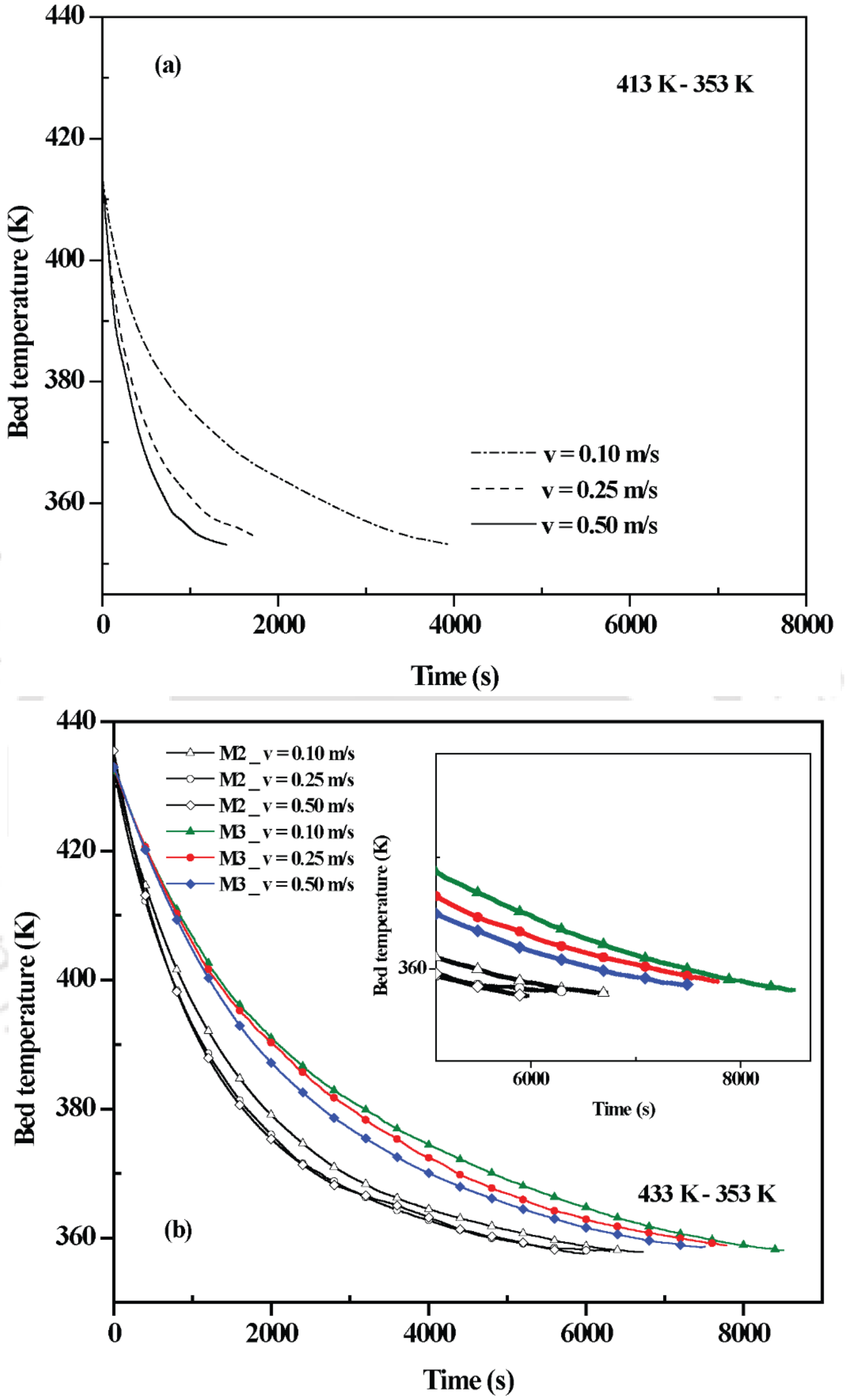

Fig.4.12 Effect of HTF velocity on the discharging rate during discharging cycle (a) M1, (b) M2 & M3.

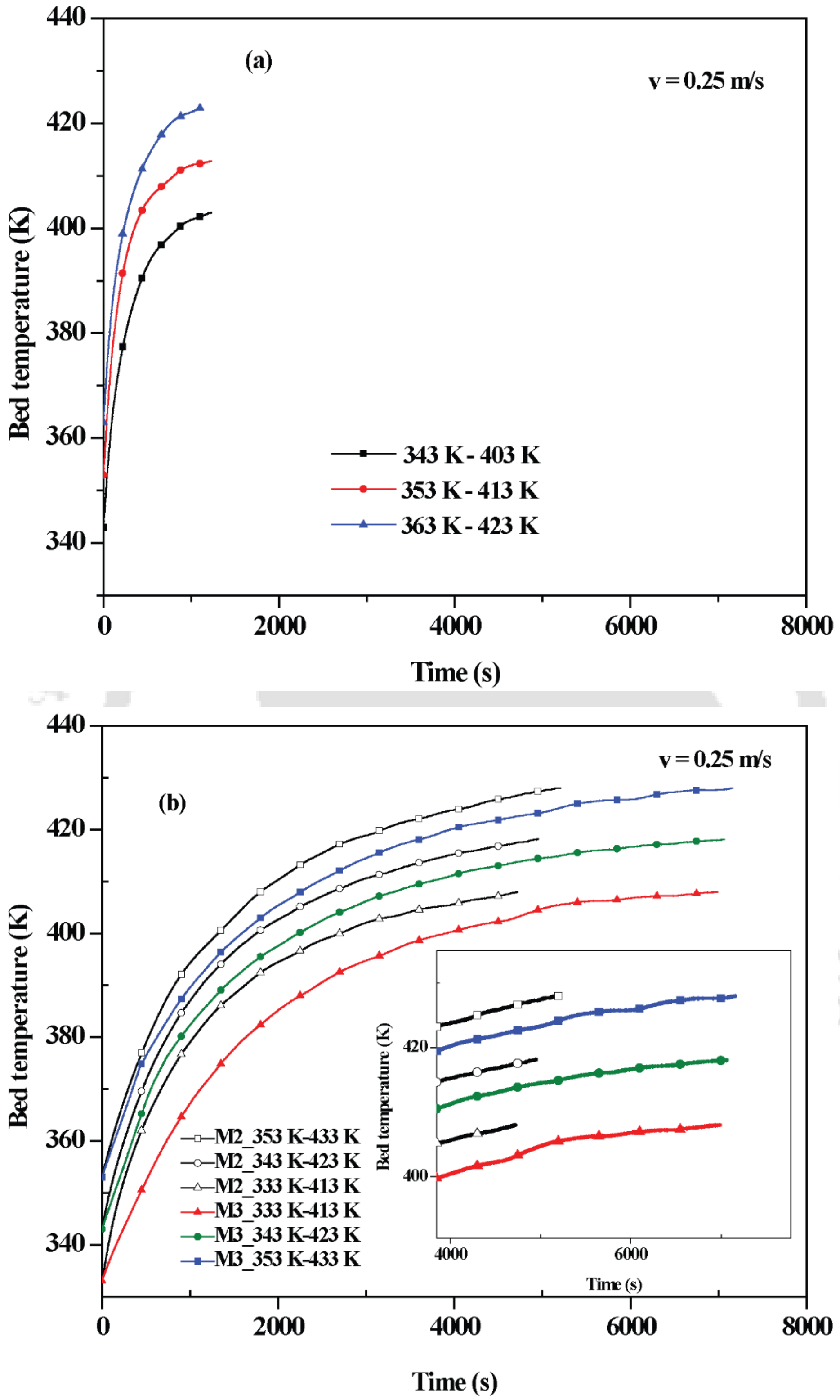

Fig.4.13 Effect of operating temperature on the charging rates (a) M1 and (b) M2, M3 during charging process.

s, 1803 s and 1912 s. The effective discharging times of the M2/M3 prototype in the corresponding temperature ranges mentioned above are 6102/7390 s, 6176/7450 s and 6297/7780 s, respectively.

4.5 Cyclic tests and limitation in operating temperature range

Extensive charging and discharging cycles have been carried out on both cast steel and concrete based sensible heat storage prototypes. It was observed that after 150 cycles, no significant performance degradation was observed in cast steel based system. However, in the case of concrete SHS prototype embedded with mild steel HTF tube, it was found that the increase in charging time was about 9 % after 100 repeated cycles. Similarly, for the discharging experiments, the increase in discharging time is about 12 %. These variations are acceptable and within the limits. Further, it was observed that after 100 cycles of charging and discharging operation, no visible crack was observed on the concrete prototype. It should be noted that trial charging experiments have been performed up to 250 °C on both the prototypes. Due to high vapour pressure and thermal expansion of thermic fluid, present experimental investigations have been limited to 180 °C. The total experimentation time for conducting a single charging-discharging cycle is about 8 hours. This includes the heating up of the oil from room temperature to the initial condition of the charging experiment, actual charging experiment, cooling of the oil from higher temperature to the discharging initial temperature and actual discharging experiment. Hence, conducting experiments continuously at higher temperature ranges of 200-250 °C is not possible due to higher vapour formation. Hence the experimental investigations have been limited to 180 °C.

4.6 Summary

Experimental investigations on the lab-scale SHS prototype were carried out during the charging and discharging cycles. Heat transfer enhancement technique was implemented by the use of longitudinally finned tubes. Performance parameters like charging/discharging time, and energy storage/discharge rate were evaluated at different operating conditions. A detailed parametric study was also conducted at various operating temperature ranges and HTF velocities. The axial and radial temperature distributions of all the prototypes tested were studied. The following conclusions are arrived from the experimental studies:

- The charging process is faster than discharging process due to the additional natural convection, which takes place after the phase change temperature.

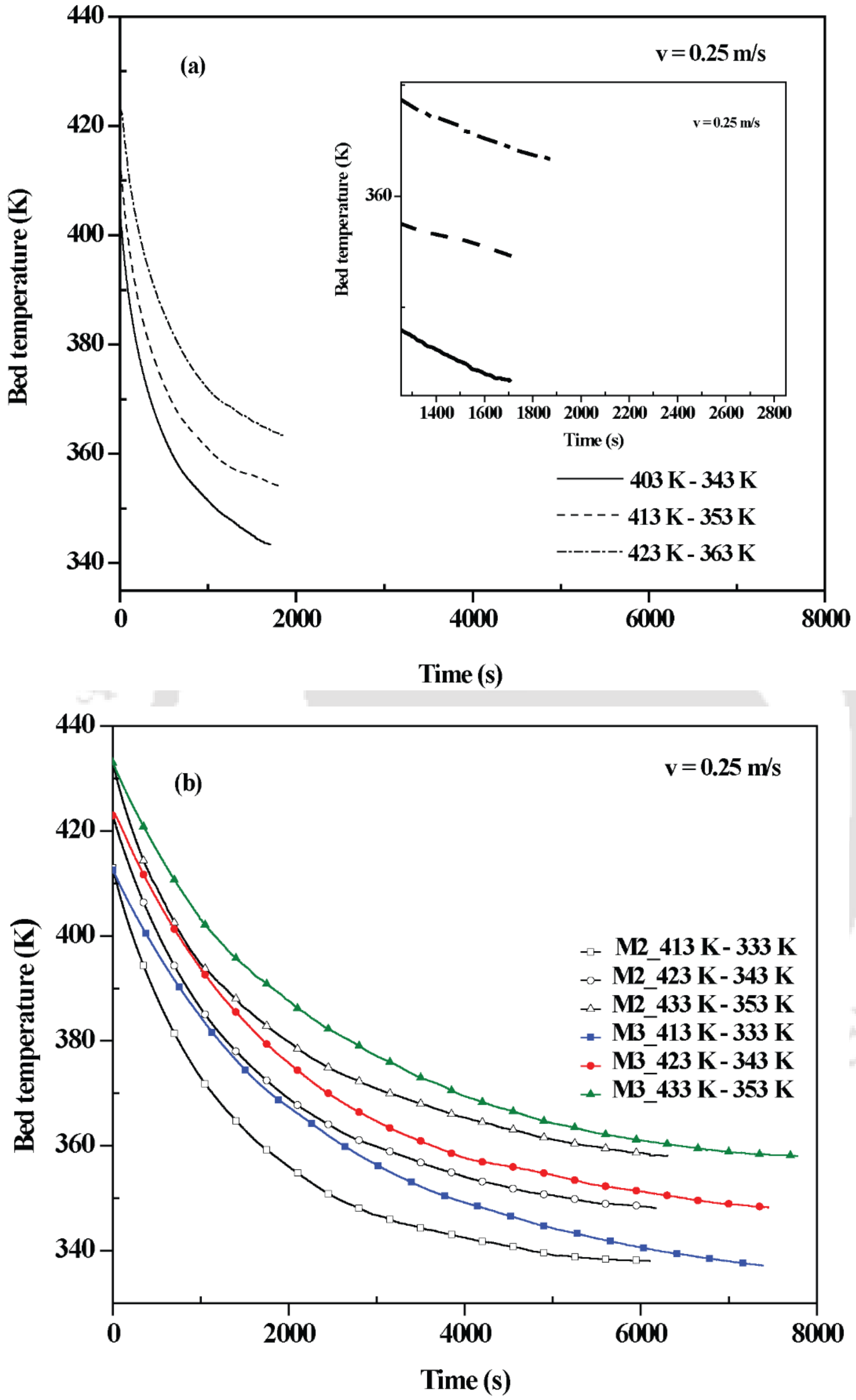

Fig.4.14 Effect of operating temperature on the discharging rates

(a) M1 and (b) M2, M3 during discharging process

- The charging/discharging time of the M1 prototype for the temperature range of 353-413 K is 1263/1803 s. The effective charging/discharging time of the M2 and M3 prototypes for the temperature range of 353-433 K are 5210/6297 s and 7160/7780 s, respectively.
- The total amount of energy stored/discharged in the M1 and M2/M3 prototypes at the respective charging/discharging times are 15 MJ and 14.06 MJ, respectively.
- The storage/discharge heat transfer dynamics is efficient in cast steel prototype than the concrete prototypes due to the higher thermal conductivity of the cast steel. Similarly, M2 prototype showed better storage/discharge performance than the M3 prototype due to the higher effective thermal conductivity of the M2 prototype.
- The storage prototypes are tested at three different velocities (v = 0.1, 0.25, 0.5 m/s) and no significant performance improvement is noticed in the case of v = 0.5 m/s when compared with v = 0.25 m/s.
- The storage performance of the system highly depends on the operating temperature range due to the temperature dependence of the thermo-physical properties of the SHS materials and the HTF. The charging and discharging times of cast steel/concrete prototype is less/more at higher operating temperatures. This is due to the increase/decrease of thermal conductivity of cast steel/concrete with the increase of temperature.

Though the experimental set up and all the prototypes have been designed to operate up to 400 °C, we could not perform continuous experiments above 250 °C (trial experiments) due to issues related to high vapor pressure the heat transfer fluid and expansion of the oil. Considering safety and other issues, operating temperate ranges have been limited to 180 °C. However, designed prototypes can be tested up to 400 °C using air as heat transfer fluid.

The experimental results of the current lab-scale SHS prototypes may be useful for the design and development of large-scale SHS units, which can be integrated in the real-time solar thermal power plants with the up gradation in the temperature range. Other potential applications are solar drying, solar driven absorption systems, etc. Additionally, the studies presented here may also be helpful in building efficient hybrid storage systems comprising of sensible and latent heat storage modules.

Chapter 5

Lab scale SHS prototype- Numerical Studies

5.1 Introduction

Design and optimization of SHS prototype require an exhaustive analysis of the heat transfer characteristics between the storage material and HTF. The number of the HTF tubes and fins on the HTF tube's outer surface play an important role while transporting the heat between them. Un-optimized model or prototype with more number of the HTF tubes and fins would lead to higher material inventory and head losses. In addition, the overall storage volume of the bed required for a given capacity will also increase proportionally. Hence, a detailed optimization study is needed to design a cost-effective SHS system. To achieve this, many experiments with different geometric configurations, number of the HTF tubes and fins, need to be conducted. This approach has two major disadvantages; (i) the development and fabrication costs of the different models to be tested is high and (ii) for up scaling, new models need to be developed for obtaining the optimized one. Development of a numerical tool for the optimization of geometric configuration and performance evaluation of SHS system is an ideal solution to overcome the above limitations.

In this section, a 3D thermal modelling to study the performance characteristics of a regenerative shell-and-tube type lab-scale SHS prototype of 15 MJ capacity is described. Selection of various parameters of the model along with initial and boundary conditions, assumptions and governing equation are explained. Heat transfer enhancement in the concrete beds is incorporated by the use of longitudinal integrated fins. Longitudinal integrated fins adopted for heat transfer enhancement in the concrete prototypes of experimental studies are also included in the numerical model including the thickness of the finned tube.

Materials used in the sensible heat storage prototypes are cast steel and concrete (Mix design M30 grade). Mix design of M30 grade is a mixture of cement, fine aggregate (sand), coarse aggregate (gravel) and water in the weight proportion of 1:1.52:3.21:0.49. The governing equations involved in the thermal model are solved using a finite element based software product, COMSOL^{TM} Multiphysics 4.3a. Hi–Tech Therm 60, a synthetic thermic oil is selected as the HTF. The thermo-physical properties of the HTF is given in Table. 5.1. Performance parameters such as charging and effective charging/discharging time and energy storage/discharge rate are evaluated at different operating conditions. A detailed parametric study is also performed at different inlet HTF flow velocities. The axial variation of temperature in the storage beds along the length during the charging/discharging processes is also presented. These numerical results will be pioneered in designing the efficient lab scale SHS systems.

5.2 TES prototype design

The design part comprising of fixing the diameter of the SHS prototype, HTF tube, number of HTF tubes, and length of the storage prototype. The major parameters considered in the design of SHS system are technical properties, cost-effectiveness and environmental impacts. The design procedures involved in the development of SHS prototypes are given below:

1. Fixing the capacity of SHS system (15 MJ for the present case)
2. Deciding the operating temperature range of the storage prototypes (80 K for concrete and 60 K for cast steel prototype)
3. Choosing the SHS material. Cast steel and concrete are selected as SHS materials based on the thermo-physical properties (Tian and Zhao, 2013) and the cost effectiveness (Nandi et al., 2012). In addition, these storage materials are easily available and modular in nature to extend any higher storage capacity.

The thermo-physical properties of cast steel and concrete of mix design 30 (M 30) are listed in Tables. 5.2 and 3.6 (refer section 3.10), respectively. The minimum volume of the SHS material required for storing 15 MJ is calculated using Eq. (3.1). Volume of SHS material with fins is estimated using Eq. (3.2) (refer chapter 3). The length of all the SHS prototypes is chosen as 1 m. The number of HTF tubes obtained through the optimization study for cast steel and concrete prototypes are 19 and 22, respectively (Prasad and Muthukumar, 2013).

The diameter and thickness of the chosen HTF tubes are 0.0125 m and 1.5 mm, respectively for all the three cases. Accordingly, the shell diameter for concrete and cast steel are found to be 0.324 m and 0.267 m, respectively.

The number of longitudinal fins over the HTF tube surface considered from the previous study is 5 (Prasad and Muthukumar, 2013).

Table 5. 1 Thermo-physical properties of Hi–Tech Therm 60 at different temperatures. (Rao, C. R. C. et al., 2018).

Temperature (K)	**ρf (kg/ m^3)**	**C_{pf} (kJ/kg K)**	**K_f (W/ m K)**	**γ (mm^2/ s)**	**μ (Pa s)**
333	844.7	2.1566	0.1289	14.61	0.012515
353	835.3	2.2314	0.1263	9.21	0.007829
373	823	2.3064	0.1238	3.82	0.003144
393	809.8	2.381	0.1213	3.00	0.002440
413	796.6	2.4558	0.1188	2.16	0.001735
433	783	2.5306	0.1164	1.58	0.001242

Table 5. 2 Thermo-physical properties of cast steel (Gil et al., 2010), copper (Tian and Zhao, 2013) and mild steel (Rohsenow et al., 1998).

Material	**k_s (W/ m K)**	**C_{ps} (J/ kg K)**	**ρ_s (kg/ m^3)**
Cast steel (1.0 % C)	40	600	7800
Copper (99.9 % purity)	401	384	8933
Mild steel (0.16-0.2 % C)	44.2	450	7800

5.3 Thermal Modelling of the TES prototype

5.3.1 Description

The SHS prototypes are modelled and analyzed using the simulation software, COMSOL Multiphysics 4.3a replicating the exact geometric and heat transfer parameters of the in-house experimental setup (as discussed in Chapter 4). Fig. 5.1 depicts the isometric view of the cast steel and concrete 3D models. The model developed is a variant of regenerative type heat exchanger, which releases/absorbs heat to/from the cold/hot HTF when the HTF is allowed to pass through the tubes. All the SHS prototypes are modelled in the form of shell-and-tube type heat exchangers. Longitudinal fins are incorporated in the concrete SHS models (can be seen in Fig. 5.1(b)). High/low temperature HTF is allowed to pass through the storage model during charging/discharging. It exchanges the heat with the tubes through convection and this heat is transferred to the solid storage material by conduction. The outer surface of the model is given adiabatic condition to replicate the insulation provided in the experimental SHS prototypes.

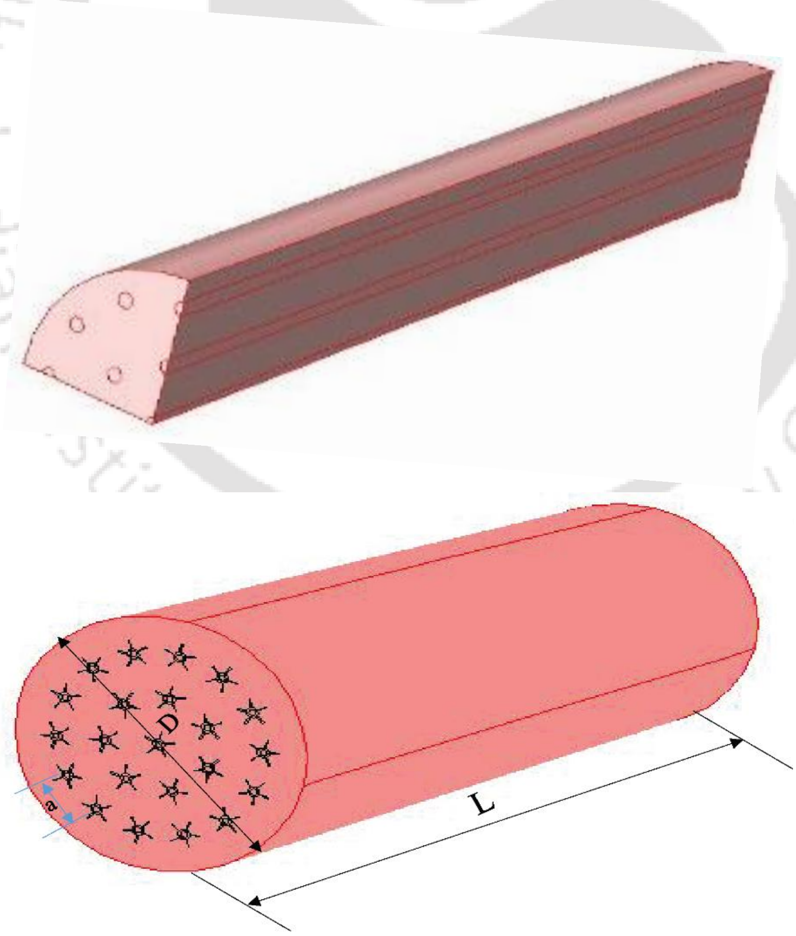

Fig.5.1 Isometric view of SHS models (a) cast steel and (b) concrete

5.3.2 Assumptions

The assumptions are made to simplify the thermal model without affecting the end outcomes. The assumptions made in the developed thermal model are:

- The fluid flow of HTF is considered as laminar. (i.e. Reynolds number is 800-2000)
- Storage material is isotropic
- HTF is incompressible, Newtonian and no viscous dissipation
- The outer surface of the SHS bed is well insulated, and thus it is adiabatic
- Neglected the radiation effect
- Contact resistance of the HTF tubes is neglected

Cast steel prototype offers zero contact resistance in the real experimental setup also as the prototype has drilled holes for allowing the HTF to pass through. This ensures direct heat transfer to take place between the HTF and cast steel. In case of concrete SHS models, the contact resistance is also neglected as the HTF tubes are buried inside the concrete prototypes (Rao et al., 2018).

5.3.3 Governing equations

In this section, a summary of the thermal model employed for simulating the transient behaviour of the SHS prototype is presented. The model developed is based on a conjugate heat transfer problem, which simultaneously solves the flow behaviour of HTF and conduction behaviour of the storage material. Accordingly, continuity, momentum, and energy equations are given in Eq. (5.1–5.4). The continuity and Navier-Stokes equations are solved concurrently to simulate the behaviour of the HTF flowing inside the charging tubes of the SHS prototype. The energy equation (Eq. 5.3) is solved using the velocities found from the solutions of Eqs. 5.1 and 5.2, to simulate the heat transfer from the HTF to the wall of the pipe. The material derivative term *DT/Dt* of Eq. 5.3 takes care the effect of convection heat transfer. The heat conduction equation (Eq. 5.4) is solved for accounting the heat transfer from the charging tubes to the SHSM. The continuity, Navier-Stokes and energy equations have been solved with an accuracy of 10^{-3} using the PARADISO solver. The three governing equations of fluid dynamics between the HTF and SHS prototype to be solved for an incompressible fluid are as follows:

Fluid flow: - The conservation of mass law applied to a fluid passing through an infinitesimally small element under consideration yields the equation of continuity and is given by Eq. (5.1)

$$\nabla \cdot \vec{v} = 0 \tag{5.1}$$

Momentum equation: - Newton’s second law applied to the fluid passing through an infinitesimally small element under consideration gives the momentum equation and is represented by Eq. (5.2).

$$\rho_f \frac{D\vec{v}}{Dt} = -\nabla P + \mu \nabla^2 \vec{v} \tag{5.2}$$

Energy equation: - First law of thermodynamics applied to a fluid/solid domain yields the energy equation. Eq. (5.3) represents the energy equation applicable to the HTF considering the convection heat transfer. Eq. (5.4) depicts the energy equation applicable to the solid SHS material and the HTF tubes, considering only the conduction heat transfer

Convection on HTF side:

$$\rho_f C_{pf} \left(\frac{DT}{Dt} \right) = \nabla.(k_f \nabla T) \tag{5.3}$$

Conduction on storage material side :

$$\rho_s C_{ps} \frac{\partial T}{\partial t} = \nabla.(k_s \nabla T) \tag{5.4}$$

5.3.4 Initial and boundary conditions

Both the stationary domain (SHS material and HTF tubes) and flow domain (HTF) are initially given a constant temperature of T_{ini}. The velocity of the HTF is set to zero initially. The charge/discharge process is initiated by specifying a constant high/low fluid inlet temperature of T_{inlet} and a constant HTF velocity. The other surfaces of the SHS models are given adiabatic boundary condition. Figure. 5.2(a)–(c) illustrates the initial and boundary conditions of the thermal model.

5.3.5 Generation of mesh

Mesh generation is the first step in solving the thermal model described in Eq. (5.3) – (5.6). In the present study, the domains and boundaries are meshed using free tetrahedral and triangular elements respectively. The free tetrahedral elements are the best to mesh curved geometry with little distortion of mesh. All three different domains (fluid domain, finned tube domain and SHS material domain) are meshed with different mesh quality parameters. It is also ensured that relatively smaller domains are meshed properly with a sufficient number of mesh elements. Domain decomposition technique is used to divide the domains. Special meshing features of COMSOL Multiphysics such as boundary layers, corner refinement and distribution are used to have a finer mesh near the critical zones i.e. near the wall. The total number of grids or mesh elements of the storage model vary with the configuration of the prototypes. The meshed view of cast steel and concrete storage models are shown in Fig. 5.3(a) and (b), respectively.

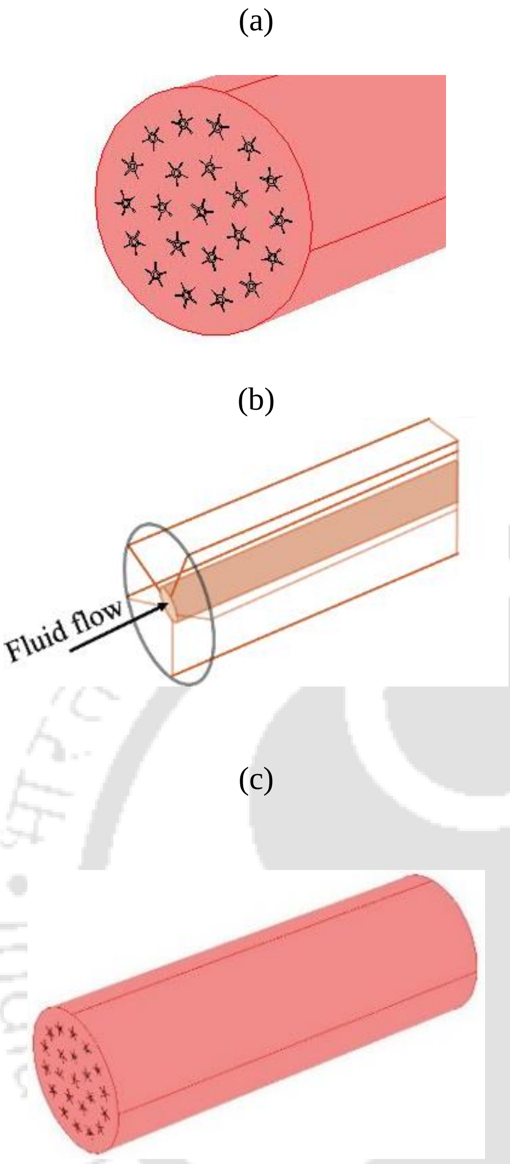

Inlet:

At (t = 0): $\vec{v} = 0$; T = T_{ini}

At (t > 0) : $\vec{v} \neq 0$; T = T_{inlet}

Interface:

No slip $(\vec{v} = 0)$

At the solid-liquid Interfaces.

Thermal insulation:

$n.(k\nabla T) = 0;$

Where, *n* is the normal vector.

Fig.5. 2 Initial and boundary conditions (a) at inlet, (b) no-slip boundary condition at the interface of a tube and (c) thermal insulation boundary condition.

5.3.6 Numerical treatment

The governing equations described in the sub-section 5.3.3 are solved by the FEM based solver, COMSOL Multiphysics 4.3a. The finite element discretization method used in the software is the Galerkin method. A linear time-dependent solver, PARDISO (Schenk and Gartner, 2004) is used to solve the governing equations. Backward difference formula is adopted to handle the time stepping. The time stepping value changes for every step based on the error value of the previous iteration. In the current simulation, the minimum and maximum time steps are set to 0.001 s and 0.1 s, respectively. The convergence criterion for the relative and absolute tolerance is set to 10^{-2} and 10^{-3} respectively.

The simulations are performed with the help of a workstation having Intel Xeon E5-2650 v2 processors and 64 GB 1866 MHz RAM. In the present study, the simulations are conducted using COMSOL Multiphysics 4.3a. which mainly uses implicit methods.

5.4 Performance parameters

Performance parameters considered in the present study are charging/discharging time (for cast steel), effective charging/discharging time (for concrete), and energy stored/recovered. These parameters are used to assess the transient performances of the storage prototypes during the charging/discharging processes.

5.4.1 Charging/discharging time

Charging/discharging time is defined as the time taken by the storage prototype's volume average temperature from its initial temperature to reach the HTF inlet temperature. When the volume average temperature of the storage prototype reaches the HTF inlet temperature, the storage prototype is said to be fully charged.

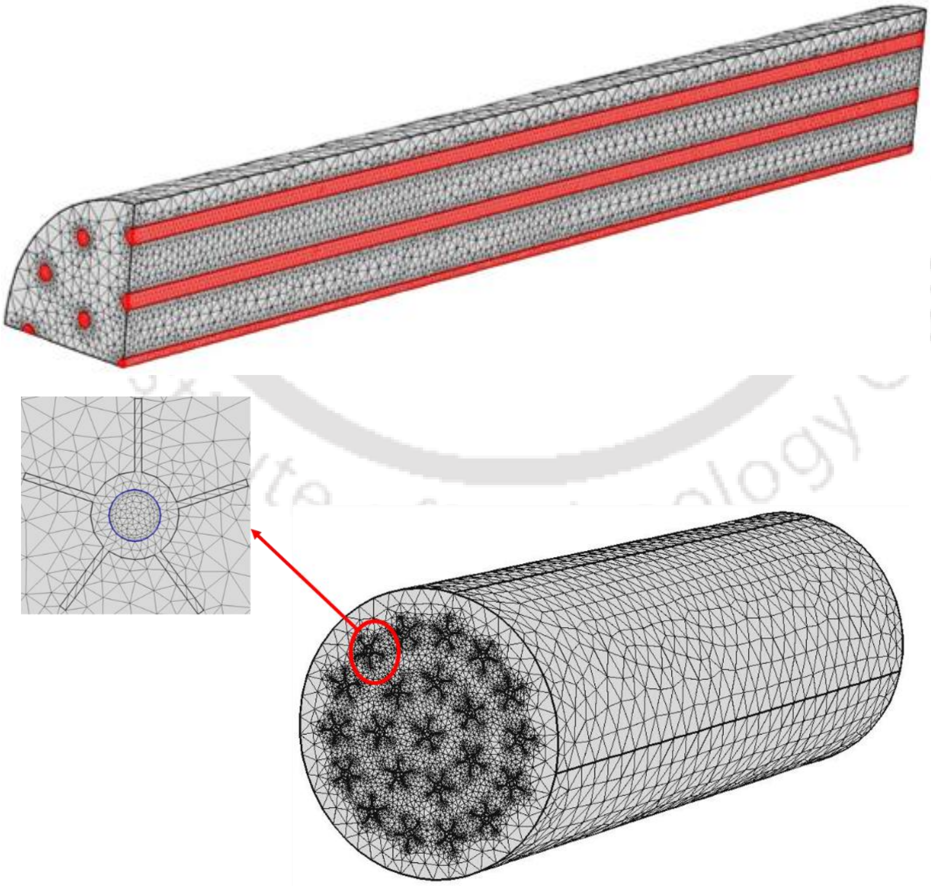

Fig.5. 3 Volumetric mesh of the SHS models (a) cast steel and (b) concrete

5.4.2 Effective charging/discharging time

SHS materials having a low thermal conductivity such as concrete, ceramic, rock, etc., take more time to completely charge/discharge due to the poor heat transfer rate between the SHS materials and the HTF. Hence, partial charging/discharging is better in these cases and this is addressed using a new parameter namely, effective charging/discharging time. Effective charging/discharging time is the time taken by the storage prototype's volume average temperature from its initial temperature to reach a temperature which is 5 K lower/higher than the HTF inlet temperature during the charging/discharging process (Rao et al., 2018).

5.4.3 Energy stored/discharged (Q_S/Q_D)

The amount of thermal energy stored/discharged from the storage prototype of different materials at their respective charging/discharging time is calculated using Eqs. (5.7) and (5.8). It is observed from Eqs. (5.7) and (5.8) that the amount of thermal energy stored/discharged depends primarily on the instantaneous temperature of the prototypes during the charging/discharging process.

$$Q_S = \rho_s V C_{ps} \left(T(t) - T_{ini} \right) \; (J) \tag{5.7}$$

$$Q_D = \rho_s V C_{ps} \left(T_{ini} - T(t) \right) \; (J) \tag{5.8}$$

5.5 Results and discussion

Charging and discharging simulations are carried out for the three SHS prototypes at different HTF flow rates and operating temperature ranges. Performance parameters such as complete/effective charging/discharging time and energy stored/discharged are assessed. Except the parametric study carried out with different velocities, an HTF velocity of 0.25 m/s is used throughout the current study in both the charging and discharging processes.

5.5.1 Grid Independence test

Numerical results obtained from different mesh densities are compared for the concrete prototype configuration to make sure that the results are mesh independent. Fig. 5.4 shows the average temperature variation of the concrete prototype with a different range of mesh elements viz. 11, 88,698, 12, 92,379 and 14, 57,466 for the charging process. It is observed from Fig. 5.4 that the average prototype temperature predicted for the cases having 12, 92,379 and 14, 57,466 elements matches closely. Hence, grid size with 12, 92,379 elements is chosen for further study.

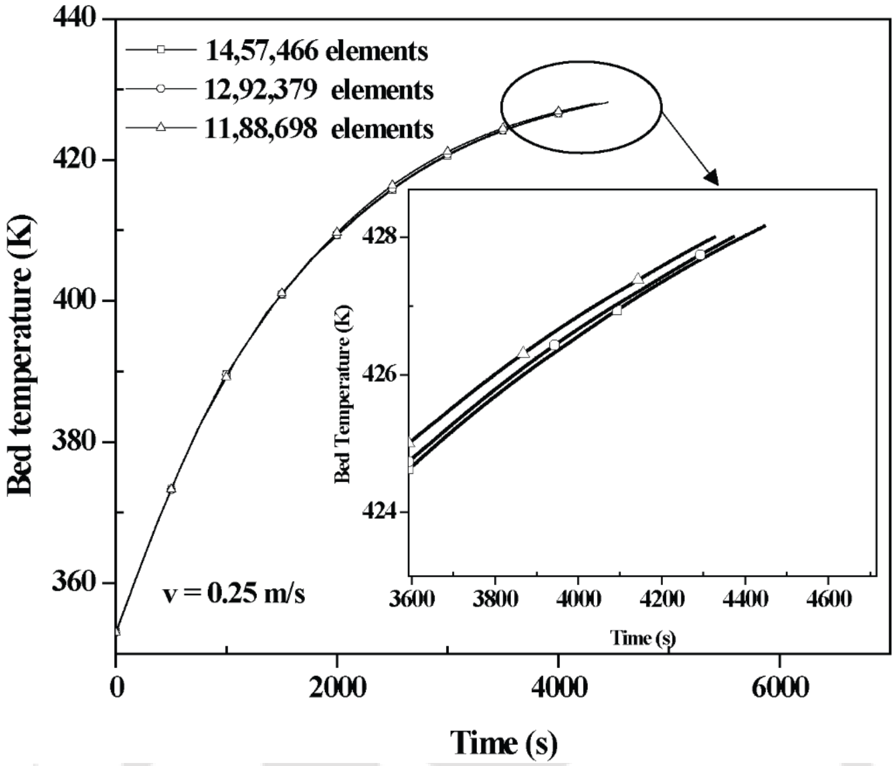

Fig.5. 4 Grid independence test of the concrete prototype.

5.5.2 Validation

In order to validate the developed numerical model, the simulation results of the charging process (temperature values at specific locations of the model) are compared with the temperature values obtained at different thermocouple locations in the lab-scale SHS prototypes (refer chapter 3) as shown in Fig. 5.5 (a) and (b). It is evident from Fig. 5.5 (a) and (b) that the current numerical results showed a good agreement with the experimental results reported in chapter 4. Figure 5.5 (a) shows the variation of temperature with respect to time along the axial length of cast steel prototype (M1). Similarly, Fig.5.5 (b) shows the variation of temperature with respect to time along the radial direction of concrete prototype (M2).

However, a small deviation in temperature of TC 4 is observed during the middle of the charging period. This might be due to the reason that more heat is lost to the surroundings as TC 4 is exposed to the highest temperature compared with the other thermocouples (TCs 5 & 6). The cast steel prototype is considered to show the axial temperature variation as the rate of charging is faster because of the high thermal conductivity of the prototype due to which negligible temperature difference is noted in the radial direction.

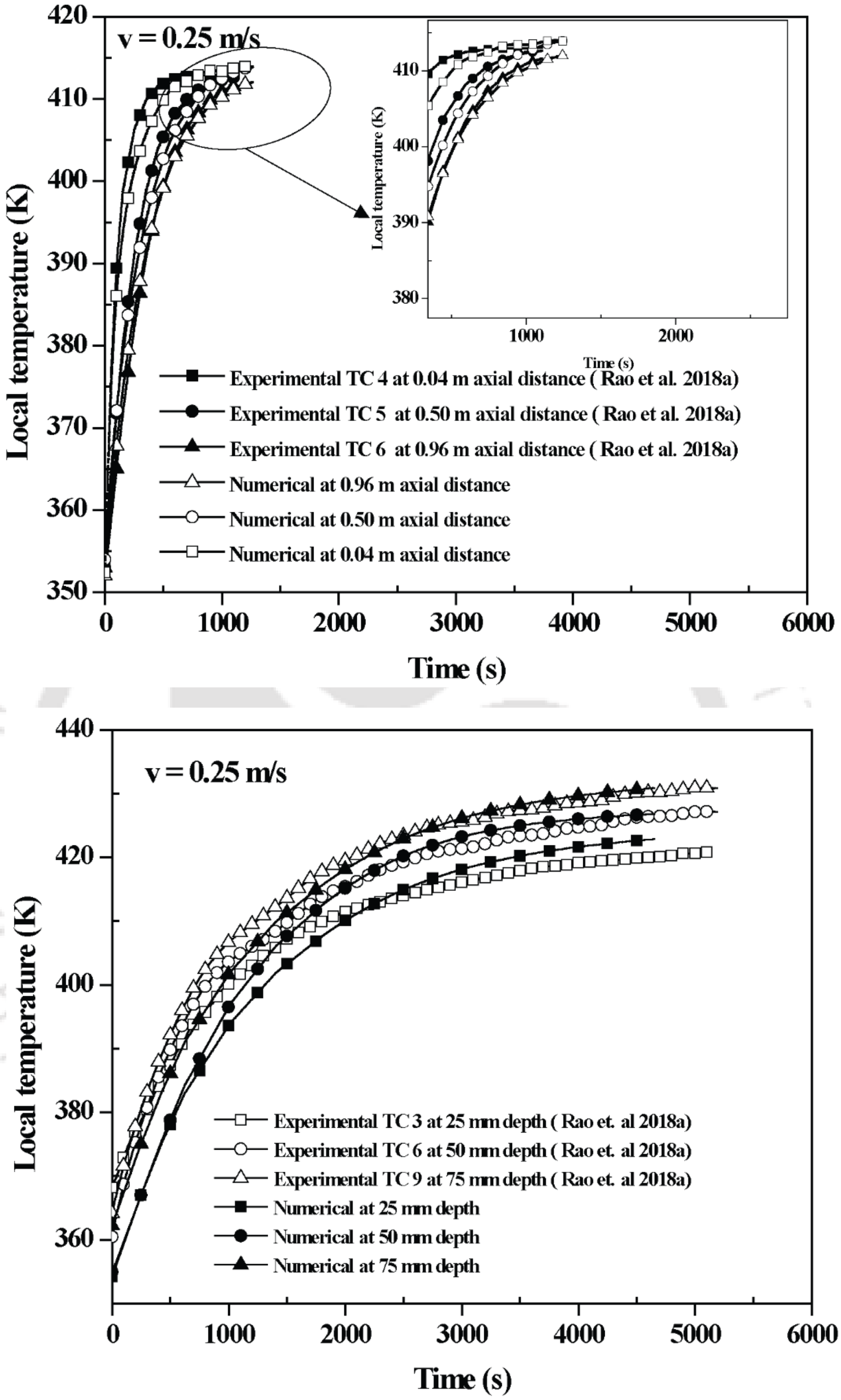

Fig.5. 5 Validation of the numerical models with the experimental results during the charging process (a) M1 – axial variation and (b) M2 – radial variation.

The axial temperature variation is considered at the linear distances of 0.04 m, 0.50 m and 0.96 m along the length of the cast steel prototype. But the numerical results of the concrete prototype are validated by considering the radial temperature variation at different radial depths i.e., at 0.025 m, 0.050 m and 0.075 m distances from outer surface of the concrete M2 prototype.

5.5.3 Charging and effective charging times

The initial average temperature of the cast steel and concrete storage prototypes during the charging process is set at 353 K and comparatively higher temperature HTF at 413/433 K is allowed to pass through the HTF tubes, which makes an initial ΔT of 60/80 K between the cast steel/concrete prototype and the HTF inlet temperature.

The charging time of the SHS prototype is one of the key parameters of performance assessment as it is directly related to the heat storage characteristic of the prototype. Figure. 5.6 presents the variation of volume average temperature of M1, M2 and M3 storage prototypes. It is observed from Fig. 5.6 that the rate of rise in temperature of M1 storage prototype during the initial charging period (0–250 s) of the charging process is higher than the later period (250–1100 s). This is due to the higher heat transfer potential present during the initial period, which is degraded over the period of time. This decrease in the HTF temperature gradient is mainly due to the rise in the average temperature of the storage prototype. The storage prototype is said to be fully charged when its average temperature reaches the HTF inlet temperature. The complete charging time of the M1 prototype is about 1106 s. Similarly, the rate of increase in temperature of the concrete prototypes (M2, M3) during the initial period (0–1700 s) of the charging process in both the prototypes is higher than the later period (after 1700 s). This is also due to the higher heat transfer potential available during the initial period. The effective charging time of M2 and M3 prototypes are about 4371 s and 6155 s. It is also observed from Fig. 3.6 that the rise in the average temperature of the M3 prototype is slower than the M2 prototype. The effective charging time of the M2 prototype is lower by about 29 % when compared to M3 prototype due to the higher thermal conductivity of the copper fins of the M2 prototype. It is also observed that, after t = 1700 s, the rate of heat diffusion becomes slower and the concrete prototypes took a longer time to achieve the previous temperature rise.

To visualize the temperature distributions inside the storage prototype, the temperature contours at different time intervals are taken. Figure. 5.7 (a)–(g) presents the sliced temperature contours at different intervals of time inside the M2 storage prototype during the charging process. Each slice unit is parted by a constant axial distance of 25 cm. At t = 0 s, there is no HTF flow and the entire storage volume is at a uniform temperature of T_{ini}. As soon as the charging process is initiated, the HTF starts giving the heat to the nearby portions of the storage material which are in direct contact with the tube surface. Since the fins on charging tube surface have higher thermal conductivity, the storage prototype is heated quickly. The temperature contours at different intervals of time viz., 60 s, 120 s, 300 s, 600 s, 1200 s 2400 s and 4200 s are shown in Fig. 5.7 (a)–(g).

5.5.4 Discharging and effective discharging times

Figure. 5.8 presents the variation of the average temperature (T_avg) of the cast steel prototype M1 and the concrete prototypes M2/M3 during the discharging process. It is observed from Fig. 5.8 that the decrease in temperature during the initial period (0–400 s) of the discharging process is higher than the later period (400–1500 s). This is due to the higher heat transfer potential present during the initial period, which is reduced over the period of time. This reduction in the heat transfer potential is mainly due to the reduction in the average temperature of the storage prototype. The storage prototype is said to be fully discharged when its average temperature reaches the HTF inlet temperature. The complete discharging time of the M1 prototype is about 1572 s.

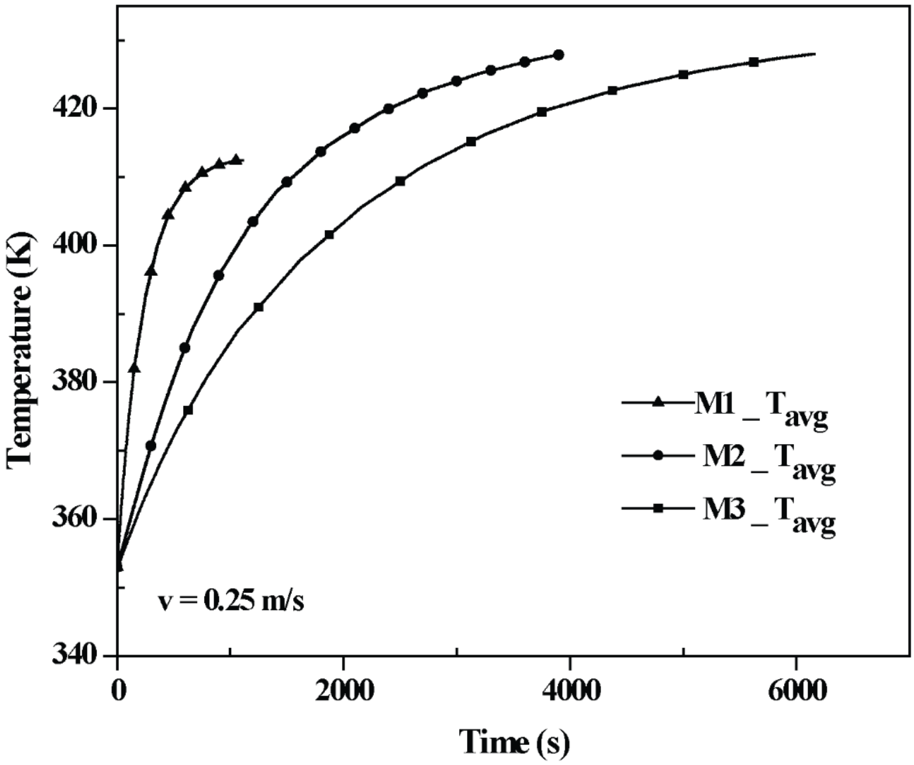

Fig.5. 6 Temperature distribution of the storage prototypes during the charging process.

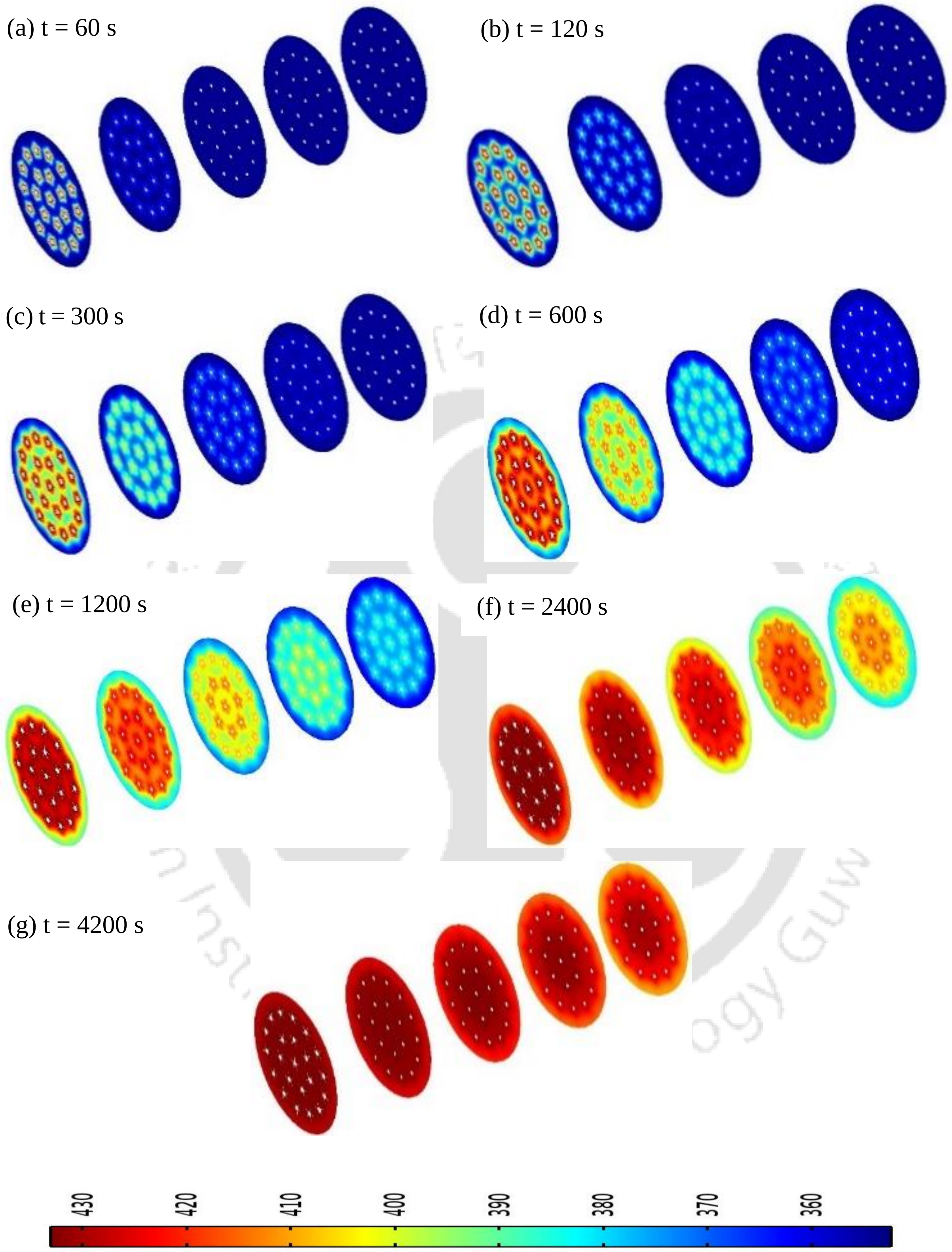

Fig.5. 7 Temperature contours of concrete prototype at time, t = 60s, 120s, 300s, 600s,1200s, 2400s and 4200s, respectively during the charging process.

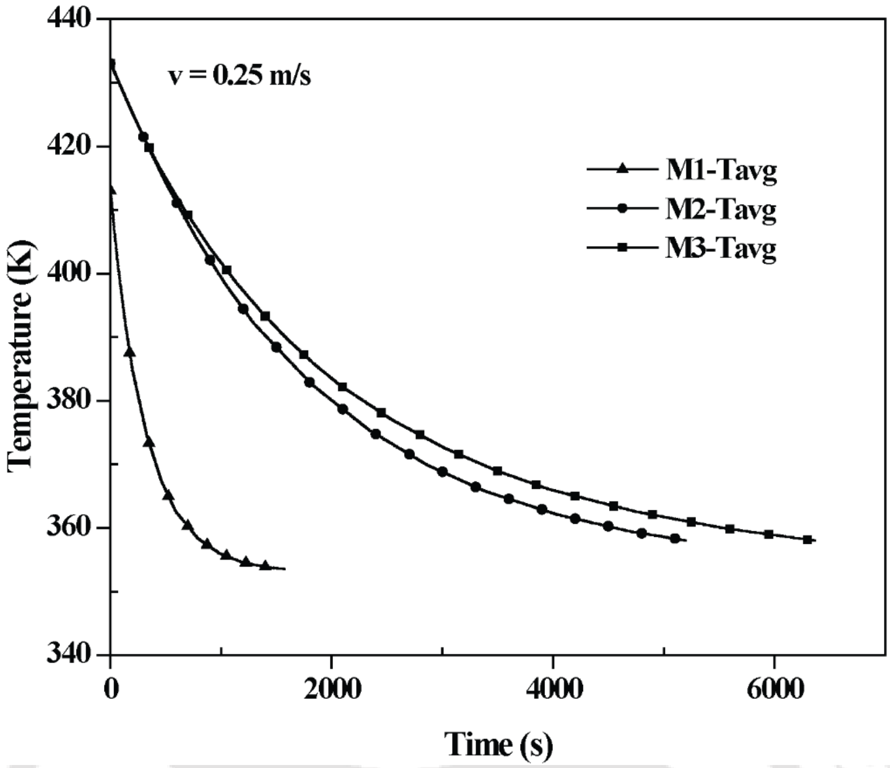

Fig.5.8 Temperature distribution of the storage prototypes during the discharging process.

It is also observed in Fig.5.8 that the decrease in temperature during the initial period (0–2800 s) of the discharging process in both the prototypes is higher than the later period (after 2800 s). This is also due to the very same reason (presence of higher heat transfer potential) mentioned for cast steel prototype.

The effective discharging times of the M2 and M3 prototypes are about 5196 s and 6360 s. It is also observed that the decrease in the average temperature of the M3 prototype is slower than the M2 prototype. The effective discharging time of the M2 prototype is lower by about 18.4 % when compared with that of the M3 prototype. This is mainly due to the higher thermal conductivity of the copper HTF tubes and fins of the M2 prototype.

Figure. 5.9 (a)–(g) presents the sliced temperature contours at different intervals of time inside the M2 storage prototype during the discharging process. It is observed from Fig. 5.9 that at time, t = 60 s, the reduction in the temperature is noticeable only in the entry region of the prototype, which is due to the higher heat transfer potential. The concentric fashion of temperature distribution confirms that the heat transfer is only due to conduction. It is also observed from Fig. 5.9 that the outer periphery of the prototype is taking more time to discharge the heat when compared to the portion near to the HTF tubes. This is due to the higher heat transfer resistance available in the outer periphery of the prototype.

5.5.5 Energy stored (Q_s)/retrieved (Q_r)

Figure. 5.10(a) shows the rate of thermal energy stored in the SHS prototypes. The amount of thermal energy stored in the prototypes at their respective charging time (or) effective charging time is estimated using Eq. (5.7). The amount of thermal energy stored in the M1 prototype at t_{ch} = 1106 s and T_{ch} = 413 K is almost 15 MJ. But in the M2/M3 prototype, the amount of total energy stored at t_{ch} = 4371/6155 s and T_{ch} = 428 K is about 14.06 MJ. The energy storage rate is faster for the M1 prototype, followed by M2 and M3 prototypes. This is due to the improved heat transfer dynamics of the M1 prototype when compared to other prototypes.

Figure. 5.10(b) shows the rate of thermal energy discharged from the SHS prototypes. The amount of thermal energy discharged from the prototypes at its respective discharging time (or) effective discharging time is estimated using Eq. (5.8). The amount of thermal energy discharged from the M1 prototype at tdis = 1572 s and Tdis = 363 K is 15 MJ. However, in the M2/M3 prototype, the amount of total energy discharged at tdis = 5196/6360 s and Tdis = 358 K is 14.06 MJ. The trend of the energy discharge rate curve is similar to the average temperature curve as the amount of energy discharged primarily depends on the average temperature of the storage prototype.

5.5.6 Axial variation of the temperature in the storage bed

(a) Charging process

Figure. 5.11 depicts the axial temperature variation of storage prototypes during the charging process. The temperature variation along the length (x-direction) with respect to a fixed reference point (15 cm, 30 cm) in y and z directions is plotted at different time intervals. When the high temperature HTF is allowed to pass through the prototypes, the temperature of the storage prototype increases by absorbing the energy from the HTF. As the HTF flows along the length of the prototype, the heat transfer rate between the HTF and the storage prototype along the length decreases. As a result, the rate of increase in temperature of the storage prototype decreases along the length. It is observed from Fig. 5.11 that the temperature difference between the entry and exit region in the storage prototype is significant during the initial period. During the end of the charging process, there exists less or zero temperature difference between the HTF and the storage prototype, which results in approaching less or zero temperature difference between the entry and exit regions of the prototypes.

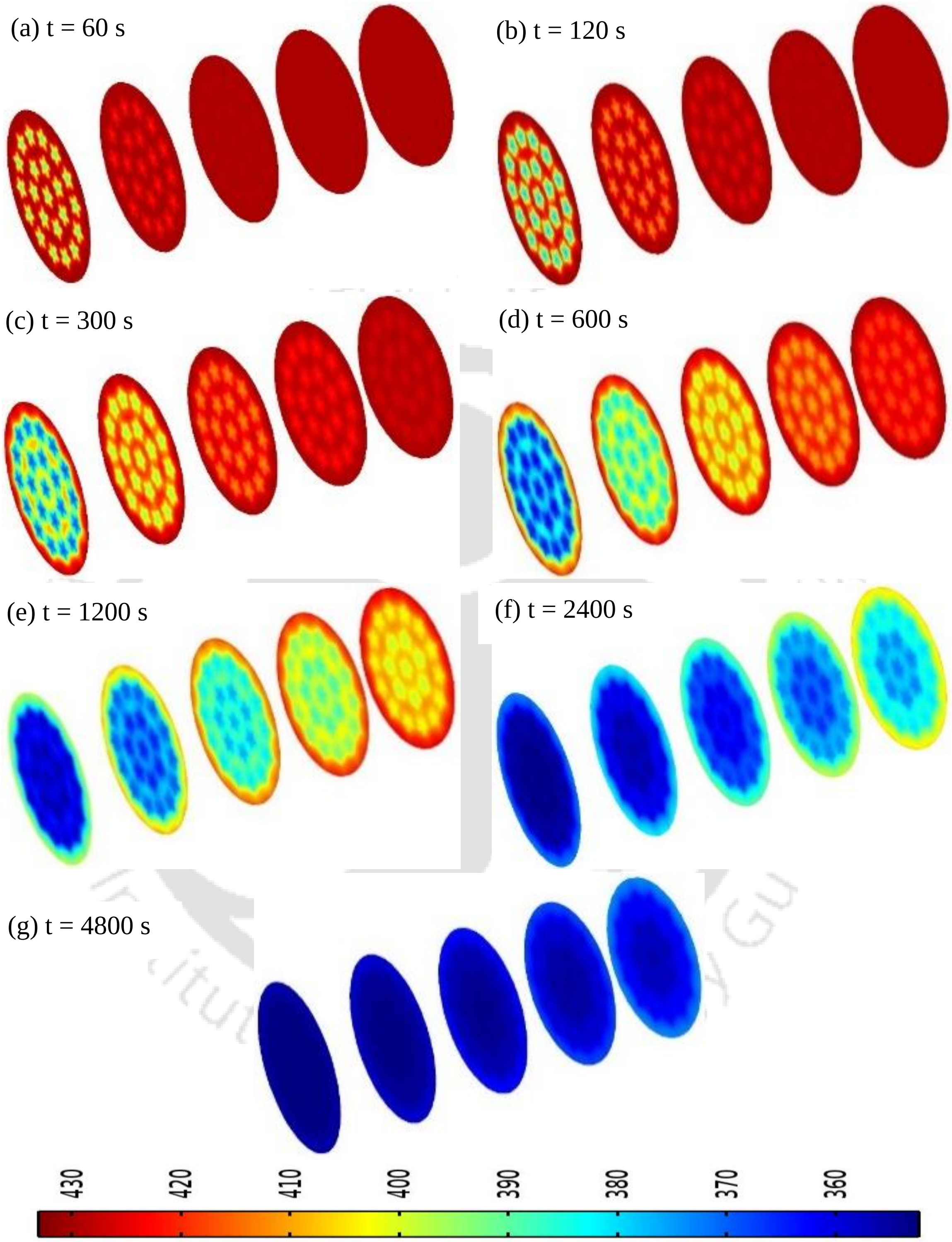

Fig.5. 9 Temperature distribution of the M2 prototype at time, t = 60s, 120s, 300s, 600s,1200s, 2400s and 4800s, respectively during the discharging process.

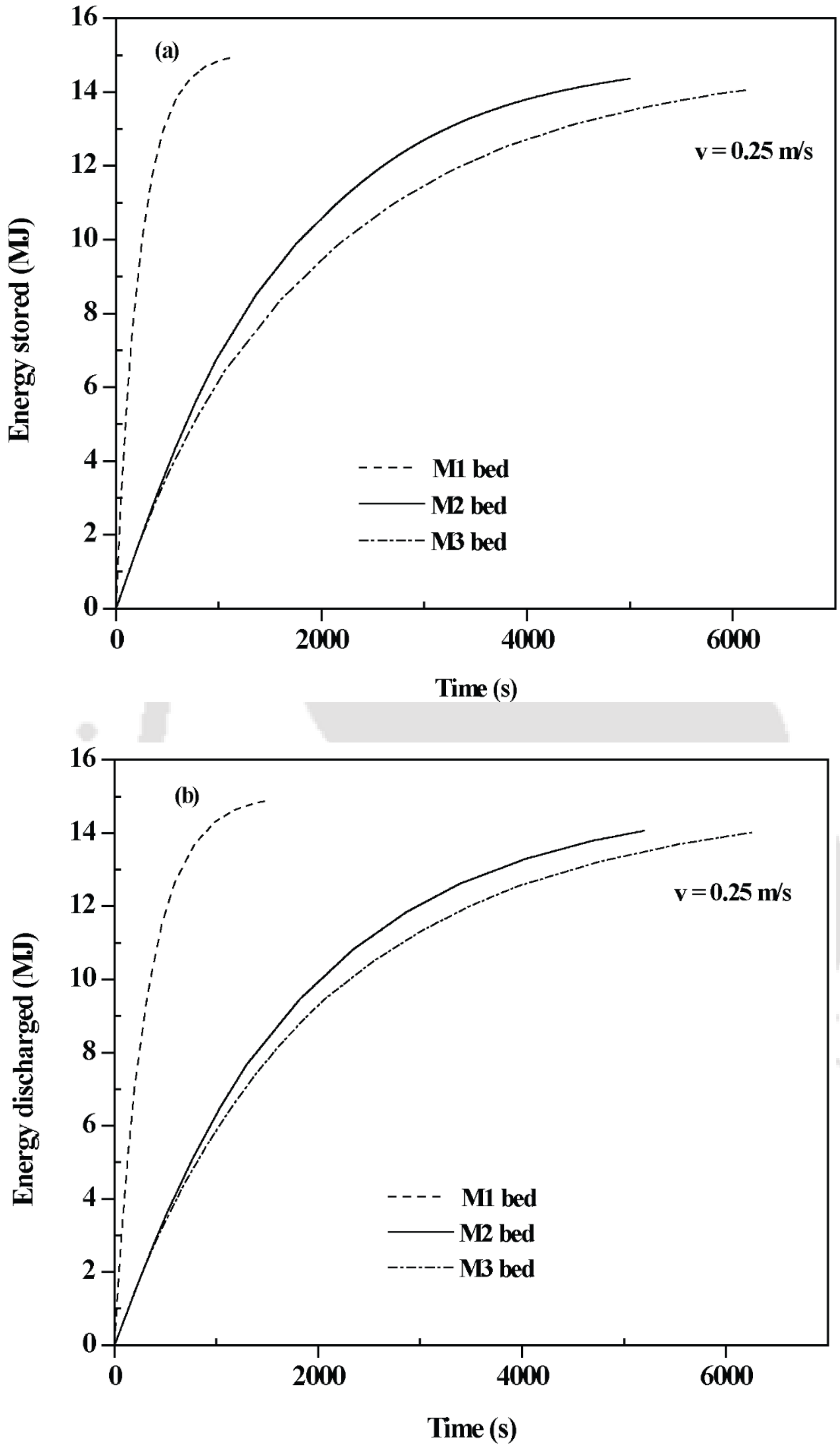

Fig.5. 10 Variation of energy (a) storage and (b) discharge rate in the storage prototypes.

At time t = 1 min, the temperature difference between the entry and exit regions of all the prototypes, viz., M1, M2 and M3 are 30 K, 5 K and 1.4 K, respectively. This temperature difference is lowered on further charging. Within 20 min from the start of the charging process, the difference between the HTF temperature at inlet and outlet for M1 prototype became 0.9 K, whereas it is 8.6 K/11 K for M2/M3 prototypes only after 70 min. For M1 prototype, the temperature difference along its length is significant only up to 10 min and after 20 min, the temperature of the prototype approaches the HTF inlet temperature. For M2/M3 prototypes, the temperature rise is significant up to 70 min and approaches the HTF inlet temperature only after 70 min. This difference that exists between the cast steel and concrete prototypes confirms the fact that the thermal conductivity and heat capacity of the SHS materials are the controlling parameters for heat transfer between the storage prototype and the HTF. The oscillatory behaviour of the temperature along the length of the M2/M3 prototypes during the initial period is observed due to the fluctuations in diffusion rates caused by higher heat transfer potential near to entry region. However, the similar behaviour is not observed in the M1 prototype due to higher diffusion rates.

(b) Discharging process

In order to show the temperature variation along the length of the storage prototype during the discharging process, temperature at specific locations is predicted along the length at fixed reference points exactly same as in the charging process. As soon as the discharging process is started, the heat is transported from the storage prototype to the HTF and due to this, the temperature of the storage prototype decreases. This decrease in temperature is phenomenal near the entry region of the prototype than the exit region due to the available higher heat transfer potential. In course of time, the difference between the temperature of the prototype at the entry and exit regions reduces. This is mainly attributed to the development of higher heat transfer potential near the exit region at a later period.

It is observed from Fig.5.12 that at time t = 1 min, the temperature difference between the entry and exit regions of the storage prototype is high. As the time progresses, this temperature difference reduces. At time t = 1 min, the temperature difference between the entry and exit regions of all the prototypes, viz., M1, M2 and M3 are 23.3 K, 3.8 K and 1.3 K, respectively. After 20 min, the difference between the HTF temperatures at inlet and outlet for M1 prototype is 3.4 K whereas it is 11/13 K for M2/M3 prototypes after 70 min. For the M1 prototype, the temperature difference between the entry and exit regions of the prototype is significant up to 10 min. After 30 min, storage prototype approached the HTF inlet conditions. For M2 and M3 prototypes, the corresponding temperature difference is significant up to 70 min and the storage prototype approached the HTF inlet conditions only after 70 min.

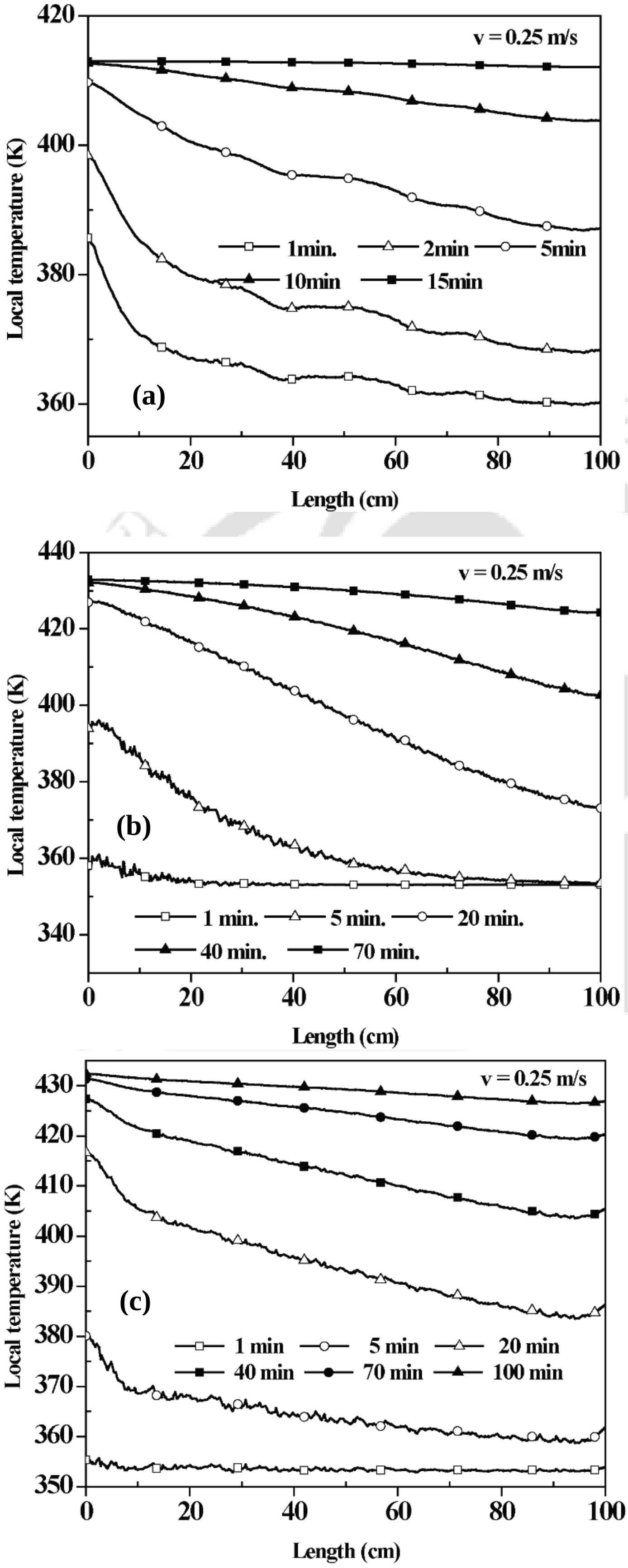

Fig.5. 11 Axial temperature variation of the prototypes (a) M1, (b) M2 and (c) M3.

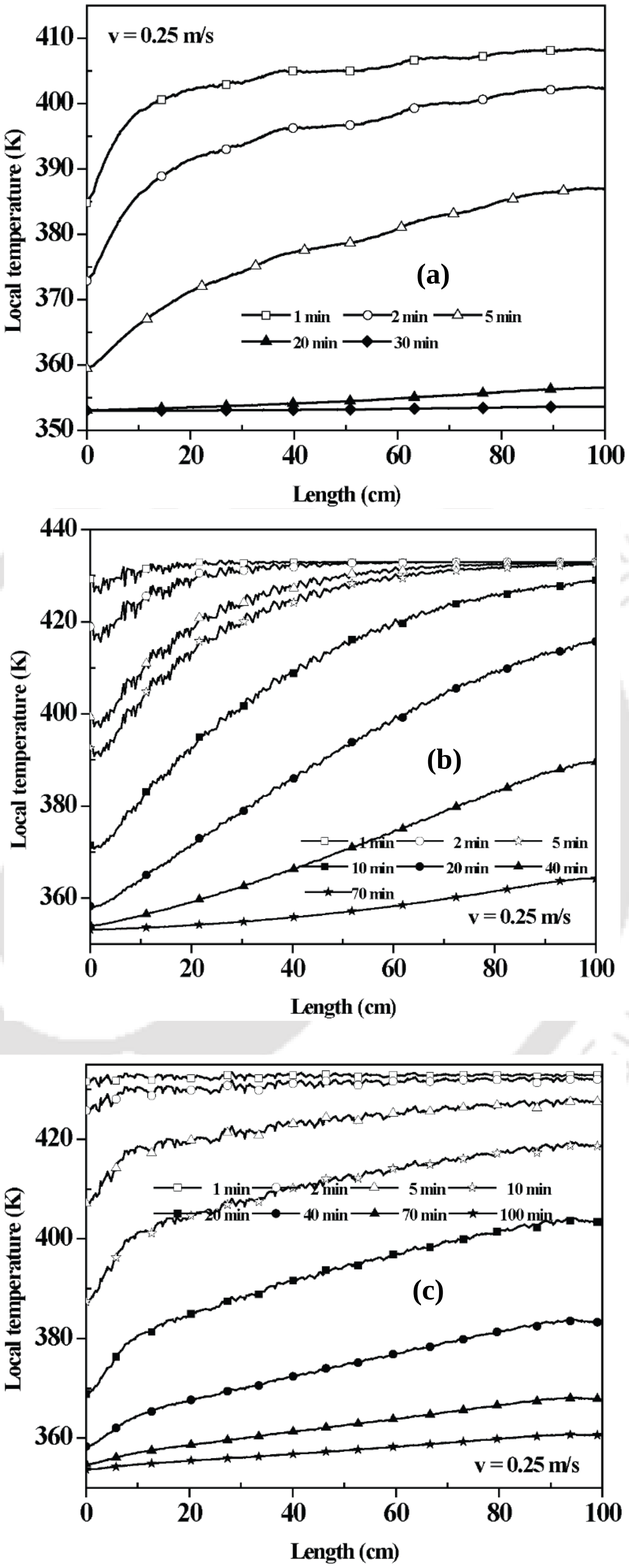

Fig.5. 12 Axial temperature variation of the prototypes (a) M1, (b) M2 and (c) M3.

It is also observed from both the figures 5.11 and 5.12 that the oscillatory nature of local temperature (K) for M2/M3 prototypes for a length L < 60 cm, which is unlike M1 prototype showing smooth increase in temperature. This intermittent appearance is due to inadequate mesh. Generating a perfect mesh of complex geometry involving multiple tubes and fins in M2/M3 prototypes is difficult. Hence, the oscillatory behaviour of the temperature time curve for the concrete SHS beds is oscillatory in nature.

5.5.7 Effect of HTF velocity

(a) Charging process

Figure. 5.13(a) and (b) shows the effect of HTF velocity on the charging rates of the cast steel and concrete prototypes. For understanding the impact of HTF velocity on the charging rate, the average temperature of the storage prototypes for three different velocities (v = 0.1, 0.25, 0.50 m/s) are compared. It is observed from Fig. 5.13(a) and (b) that the average temperature of the prototype at higher HTF velocity is increasing at a faster rate than the lower HTF velocity cases. This is because of the availability of higher convective heat transfer coefficient at higher HTF velocity. The charging times of the M1 prototype for the velocities of 0.1 m/s, 0.25 m/s and 0.5 m/s are 2296 s, 1106 s and 957 s, respectively. The reduction in charging time of the M1 prototype with 0.25 m/s as compared to 0.1 m/s is 52 %. Whereas, the reduction in the charging time of the M1 prototype with 0.5 m/s as compared to 0.25 m/s is only 15 %. The effective charging time of the M2/M3 prototype for the velocities of 0.1 m/s, 0.25 m/s and 0.5 m/s are 4606/6680 s, 4371/6155 s and 4276/6010 s, respectively. The magnified graph inside Fig. 5.13(b) gives a better clarity about the variation of the temperature distribution of the concrete prototypes at different velocities of the HTF.

(b) Discharging process

Figure. 5.14(a) and (b) shows the effect of HTF velocity on the discharging rates of cast steel and concrete storage prototypes. It is observed from Fig. 3.14(a) and (b) that the average temperature of the prototype for higher HTF velocity case is decreasing at a faster rate than the lower HTF velocity case. This is because of the increased forced convection present in the higher HTF velocity case. The discharging time of the M1 prototype for the velocities of 0.1 m/s, 0.25 m/s and 0.5 m/s are 3182 s, 1572 s and 1187 s, respectively. The reduction in discharging time of the storage prototype with 0.25 m/s as compared to 0.1 m/s is 50.6 %. Similarly, the reduction in the discharging time of the storage prototype with 0.5 m/s as compared to 0.25 m/s is 24.5 %. The effective discharging times of the M2/M3 prototype for the velocities of 0.1 m/s, 0.25 m/s and 0.5 m/s are 5447/6988 s, 5196/6360 s and 5058/6138 s, respectively.

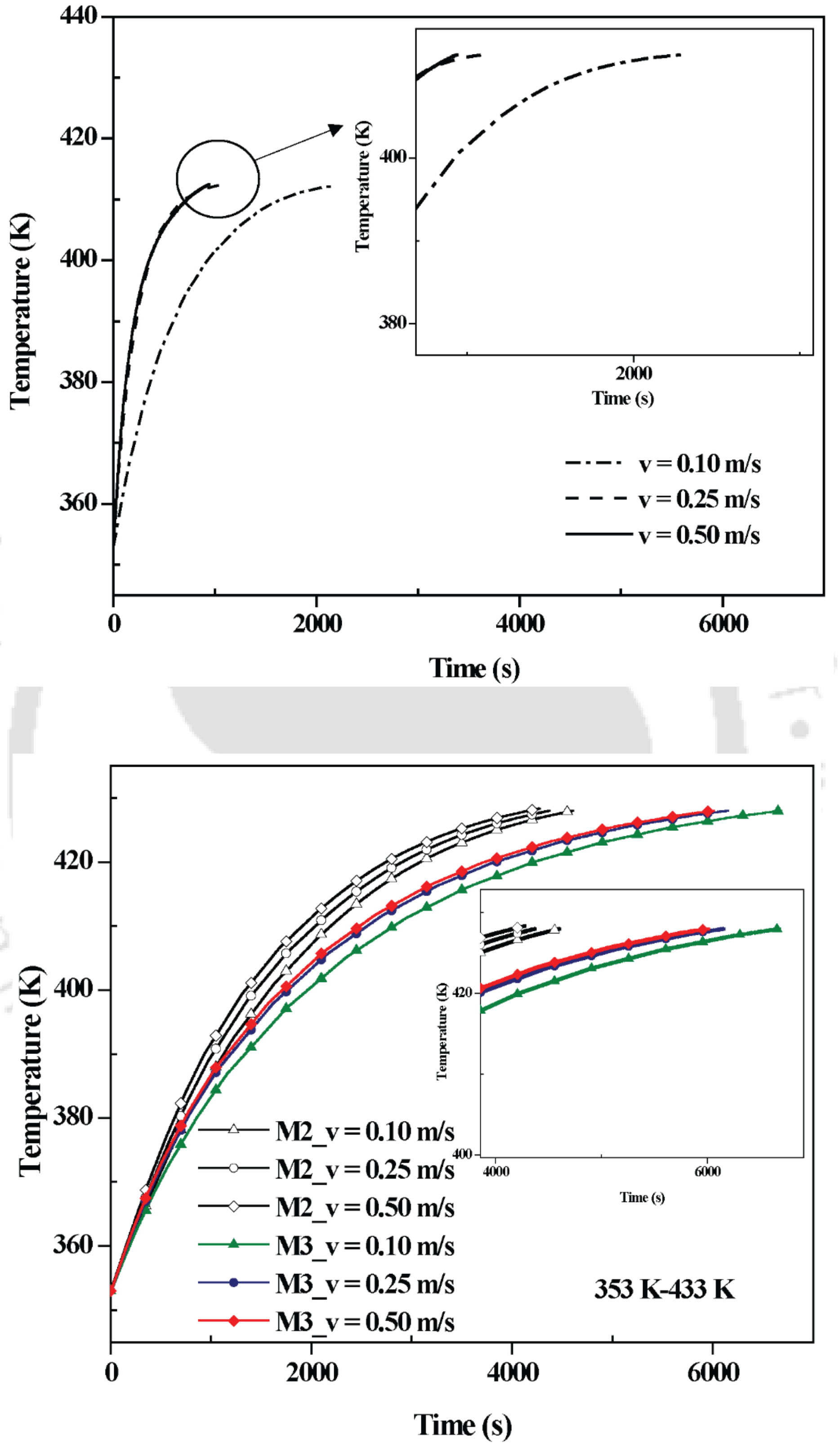

Fig.5. 13 Effect of HTF velocity on the charging rate of (a) M1, (b) M2 and M3.

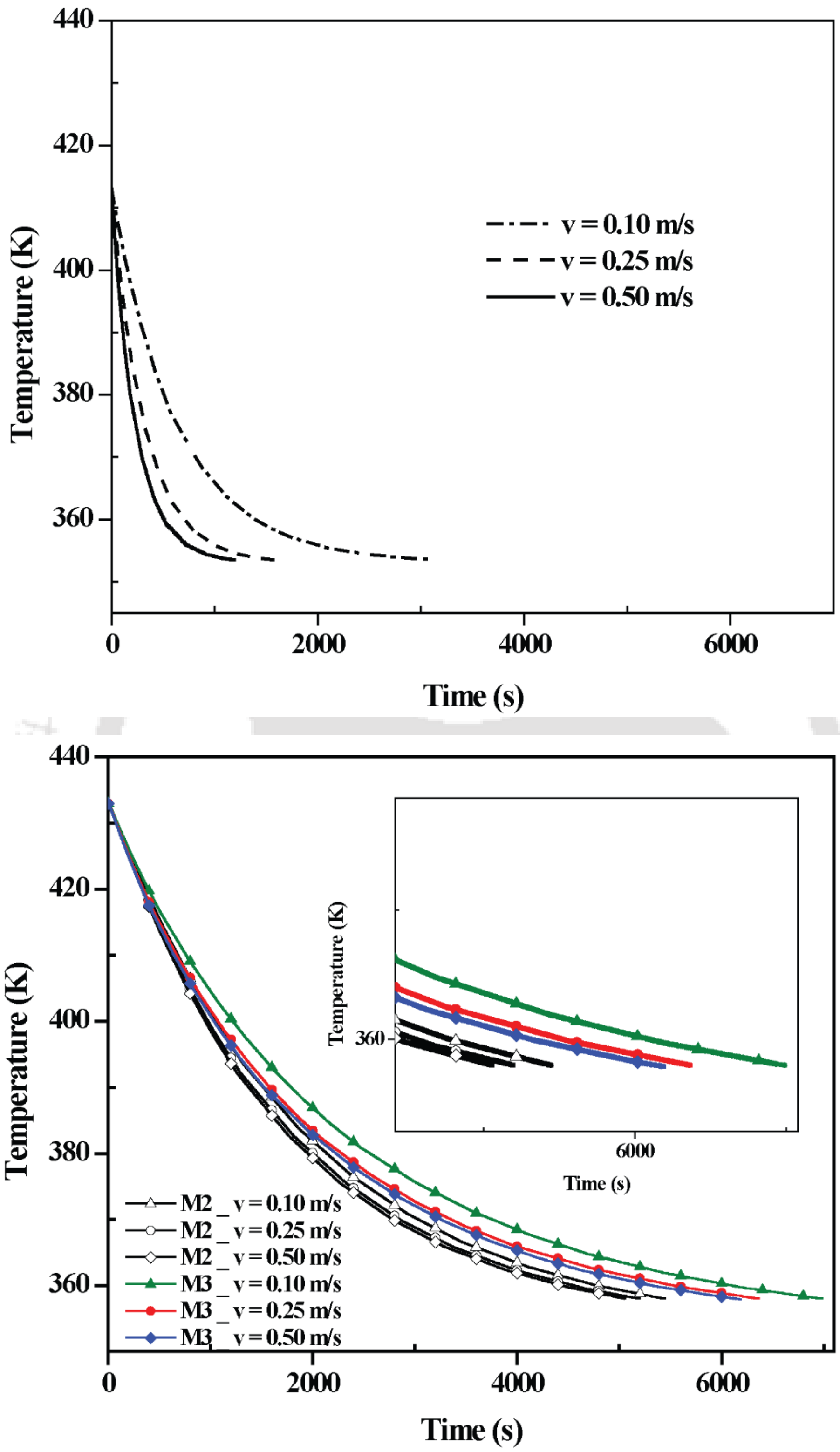

Fig.5. 14 Effect of HTF velocity on the discharging rate of (a) M1, (b) M2 and M3.

5.6 Summary

Numerical investigations on the lab-scale cast steel and concrete SHS prototypes are carried out during the charging and discharging processes. Heat transfer enhancement in the concrete prototypes is achieved by the use of longitudinal fins. Performance parameters such as complete and effective charging/discharging times and energy storage/discharge rate are evaluated. A detailed parametric study is also performed at different HTF inlet flow velocities. The axial temperature variation of the storage prototypes along their length is also studied. The following points gives a brief summary of the results of the numerical study:

- The charging/discharging time of the M1 prototype for the temperature range of 353-413 K is 1106/1572 s.
- The effective charging/discharging time of the M2 and M3 prototypes for the temperature range of 353-433 K are 4371/5196 s and 6155/6360 s, respectively.
- The total amount of energy stored/discharged in the M1 and M2/M3 prototypes at the respective charging/discharging times are 15 MJ and 14.06 MJ, respectively.
- The performances of three prototypes are evaluated at three different velocities (v = 0.1, 0.25, 0.5 m/s) and no significant performance improvement is noticed in the case of v = 0.5 m/s as compared with v = 0.25 m/s.
- The charging/discharging time of cast steel/concrete prototype is less/more at higher operating temperatures. This is due to the increase/decrease of thermal conductivity of cast steel/concrete with the increase of temperature.
- The storage/discharge heat transfer dynamics is efficient in cast steel prototype than the concrete prototypes due to the higher thermal conductivity of the cast steel. Similarly, M2 prototype showed better thermal performance than the M3 prototype due to higher effective thermal conductivity of embedded copper tubes.

The simulation results of the current lab-scale SHS prototypes may be useful in the design and development of large-scale SHS units, which can be integrated with the real-time STPPs with the upgradation in the temperature range. Additionally, results presented here may also be helpful in building an efficient hybrid storage system comprising of sensible and latent heat storage systems.

Chapter 6

High temperature Lab scale SHS bed configurations - Comparison

6.1 Introduction

In this chapter, a numerical investigation on transient behaviour and heat storage capability of the lab scale SHS beds designed for solar thermal power plant application of different configurations is presented. A three dimensional (3D) thermal model has been developed using COMSOL Multiphysics 4.3. Employing concrete, cast steel and cast iron heat storage beds, numerical investigations have been carried out for different geometrical configurations viz., square, circular and hexagonal. Thermal storage performances in terms of heat storage capacity and charging time have been investigated. The storage volume and heat transfer area of the beds are maintained constant in thermal modelling for the different configurations. Numerical results are validated with the experimental data and a good agreement is obtained. Important results obtained from the parametric studies during the charging cycle have been presented. Simulations have been carried out in laminar flow regime of HTF at temperature range of 523 K–583 K for cast iron & cast steel, and 523–593 K for concrete respectively.

6.2 Design of Lab scale SHS bed

The cost of a solar TES system mainly depends on the three components i.e., storage material, heat exchanger and land cost. Optimum design of heat exchanger is important for building the cost effective storage systems. The sequence of the steps followed in the design of SHS model is given below.

- Fix the storage capacity (10 MJ for present case).
- Fix the temperature difference considered for different SHS materials: ΔT_{ch} = 60 K - for cast steel, cast iron and ΔT_{ch} = 70 K - for concrete storage beds.
- Calculate the minimum volume (V_{min}) of SHS material required to store 10 MJ by using the reference Eq. (3.1).
- Fix the diameters of the storage bed (D): 0.27 m is selected for cast iron and cast steel and for concrete is 0.325 m. Number of HTF tube /drills (n = 20) and HTF tube diameter (d) of 0.0125 *m* are fixed for all three geometries and materials (Prasad and Muthukumar, 2013).
- Calculate the length of the SHS system (L) using Eq. (3.2). The length of the concrete storage bed is found to be 1 m and 0.8 m for cast steel and cast iron beds respectively.
- For a given SHS material, different geometries (circular, hexagonal and square) are considered by maintaining the cross sectional area constant and varying their length.

Two-dimensional cross-sectional views of the three selected bed geometric configurations for the present numerical investigations are represented in Fig.6.1.

6.3 Model description

The isometric view of the SHS concrete bed with embedded HTF tube passages (or) charging tubes is shown in Fig. 6.2. The storage module is a regenerative type heat exchanger which absorbs / releases heat energy by flow of the hot /cold HTF, respectively through the charging tubes. It consists of a cylindrical bed with charging tubes embedded into it. HTF at high temperature is supplied to the storage bed from the left end and it exits from the right end exchanging the heat with tube interface through convection and this heat is further conducted to the solid storage bed. The outer surface of bed is assumed well insulated to avoid heat losses to surrounding.

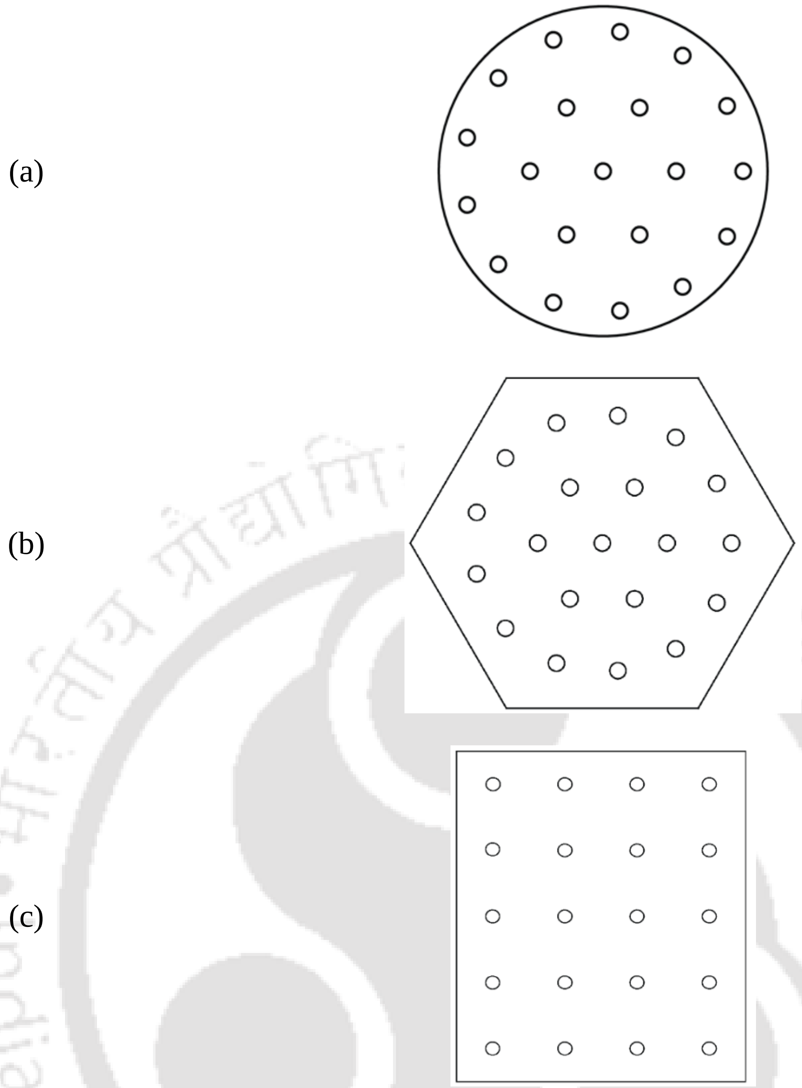

Fig.6. 1 Cross sectional views of (a) circular, (b) hexagonal and (c) square geometries.

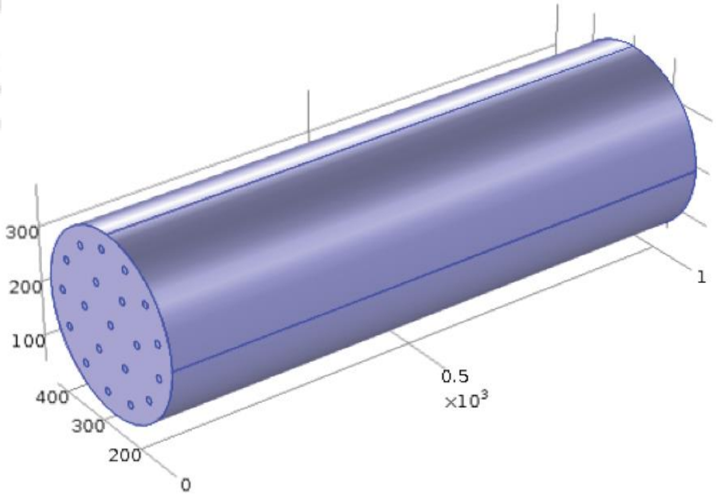

Fig.6. 2 Isometric view of concrete bed

6.4 Mesh Generation

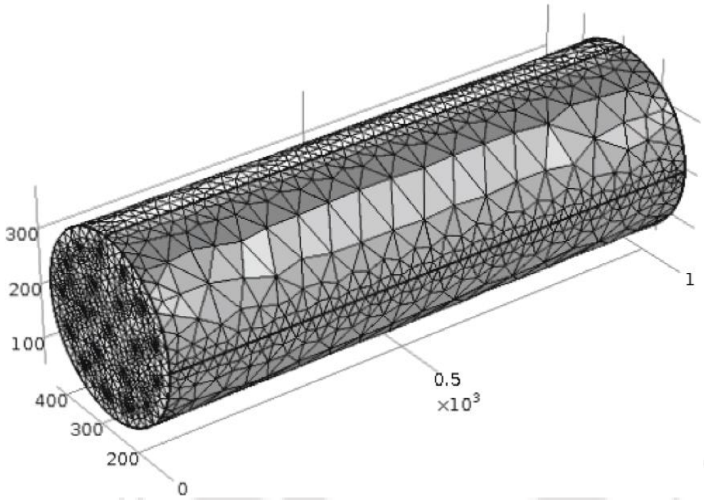

Fig.6. 3 Computational mesh of concrete bed.

Free tetrahedral (unstructured triangular) mesh has been used to ensure that relatively smaller geometries are also discretized with sufficient number of elements. The total number of elements of complete storage bed model varies with the type of geometry configuration of the bed selected. A 3D model meshed circular geometry of SHS concrete bed is shown in Fig.6.3. Thermo-physical properties of the various SHS materials considered for the present analysis are given in Table 6.1 and respective charging times of various geometries are given in Table 6.2.

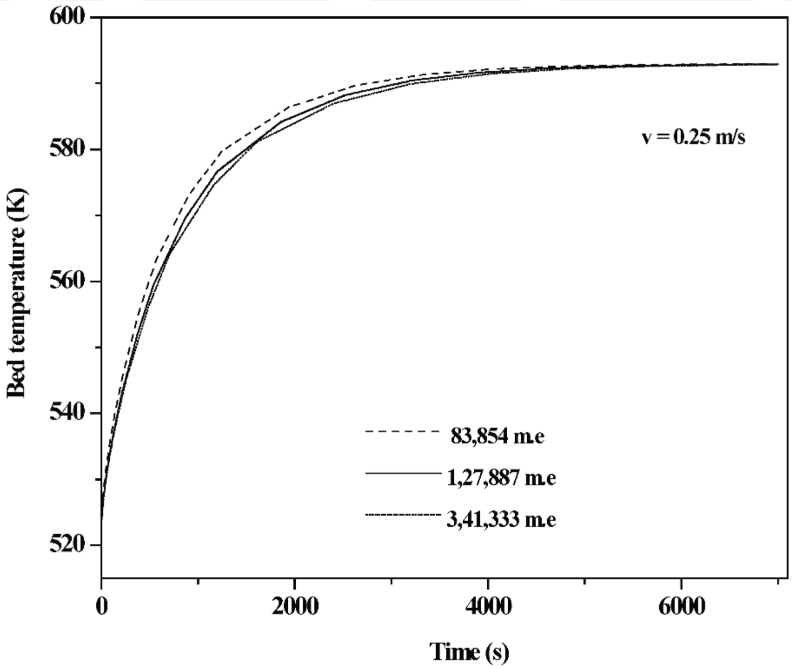

Fig.6. 4 Grid independence test

6.5 Grid Independence Test

For concrete bed, the number of mesh elements (m.e) is varied from 85,854(extremely coarse) to 3, 41,333(coarse). As illustrated in Fig. 6.4, the average bed temperature predicted for the mesh sizes of 1, 27,887(extra coarse) and 3, 41,333 (coarse) matches closely. It is also noted that increasing the mesh element beyond coarse mesh (fine mesh 58, 98,939) leads to increase in computational time by about 62-86 hours for a single run. In order to reduce the computational time, mesh size of 85,854 (extremely coarse) has been chosen for further analysis.

6.6 Results and Discussion

Numerical simulations are carried out employing various storage materials (cast steel, cast iron and concrete) for different geometrical configurations viz., circular, hexagonal and square. Performance parameters such as effective charging time, energy storage rate and charging energy efficiency are predicted by varying HTF flow rates (or velocities).

6.6.1 Charging time

The charging times for three geometries of cast steel (CS), cast iron (CI) and concrete are shown in Fig.6.5 (a-c), respectively. The storage bed is said to be fully charged when its volume average temperature reaches to 583 K. It is observed that the time required for fully charging the cylindrical bed is relatively less compared to hexagonal and square prism geometries. This is due to the fact that the outer surface in circular geometry is smooth and curved. In case of rectangular and hexagonal configurations, due to the sharp corners and edges formed by the intersection of lateral faces, there will be limitation in the symmetric heat transfer. As a result, the charging time will be more for the rectangular and hexagonal configurations, which is a major parameter in the energy storage systems. It is also observed that the charging time increases as the number of corners and edges in the outer periphery of geometry increase. This is clearly illustrated in Table 6.2. As it is difficult to differentiate charging times, a magnified view is presented inside the respective Figs. 6.5 (a-c) to capture the variation in charging time. It is also observed that for a given heat storage capacity of 10 MJ, the cylindrical bed configuration of cast iron is taking less time to charge when compared to cast steel cylindrical bed and the difference in charging time is 195 s. This is due to the fact that cast steel is having 1.6 % higher volumetric heat capacity than cast iron. Therefore, cast steel bed requires more heat to increase its temperature than cast iron. As illustrated in Fig.6.5, for a given storage capacity and storage volume, circular geometry performance is better than the other two geometries. Therefore, circular geometry is chosen for the further investigation.

In order to visualize the temperature distributions inside the storage bed during the charging process, the temperature contours of the concrete bed are taken and illustrated in Fig. 6.6(a) at different intervals of charging cycle viz., 0 s, 2400 s and 6200 s. It is noticed from Fig.6.6 (b) (i) that, at t = 0 s when there is no HFT flow, the entire storage volume is at uniform temperature of T_{ini}. As soon as the charging of the storage bed is initiated by supplying HTF inside the charging tubes at a temperature, T_{inlet}, it starts heating the surrounding storage material and the portions of storage material which are in direct contact with tube surface. It is also noticed from the temperature contours that the left end of storage bed is getting charged first then followed by the right end although the HTF enters at constant inlet temperature. This is because of temperature drop of HTF as it proceeds toward right end. In order to capture the radial and axial variation of temperature of SHS bed during the charging, sliced views are presented in Fig. 6.6(d-e) for different intervals (viz., 0 s, 2400 s and 6200 s) of charging process. Each slice section is separated by a constant axial of 20 cm and it has been observed that inlet slice section is charged rapidly as compared to other slice sections.

Table 6. 1 Thermo-physical properties and estimated mass of SHS storage beds and thermo-physical properties of HTF.

Storage bed	ρ	C_p	k_s	V^*_a	**m**
(circular)	**kg/m^3**	**J/kg-K**	**W/m-K**	**m^3**	**kg**
cast steel	7800	600	40	0.053	413
cast iron	7200	560	37	0.053	382
concrete	2200	850	1.5	0.097	213
HTF	816.4	2343.6	0.123	----	----

Table 6. 2 Charging times for different geometries

SHSM	**Geometry configuration**	**Charging time(s)**
cast steel	Square	1,688
	Hexagonal	1,790
	Circular	1,552
cast iron	Square	1,457
	Hexagonal	1,488
	Circular	1,357
concrete	Square	6,667
	Hexagonal	6,755
	Circular	6,183

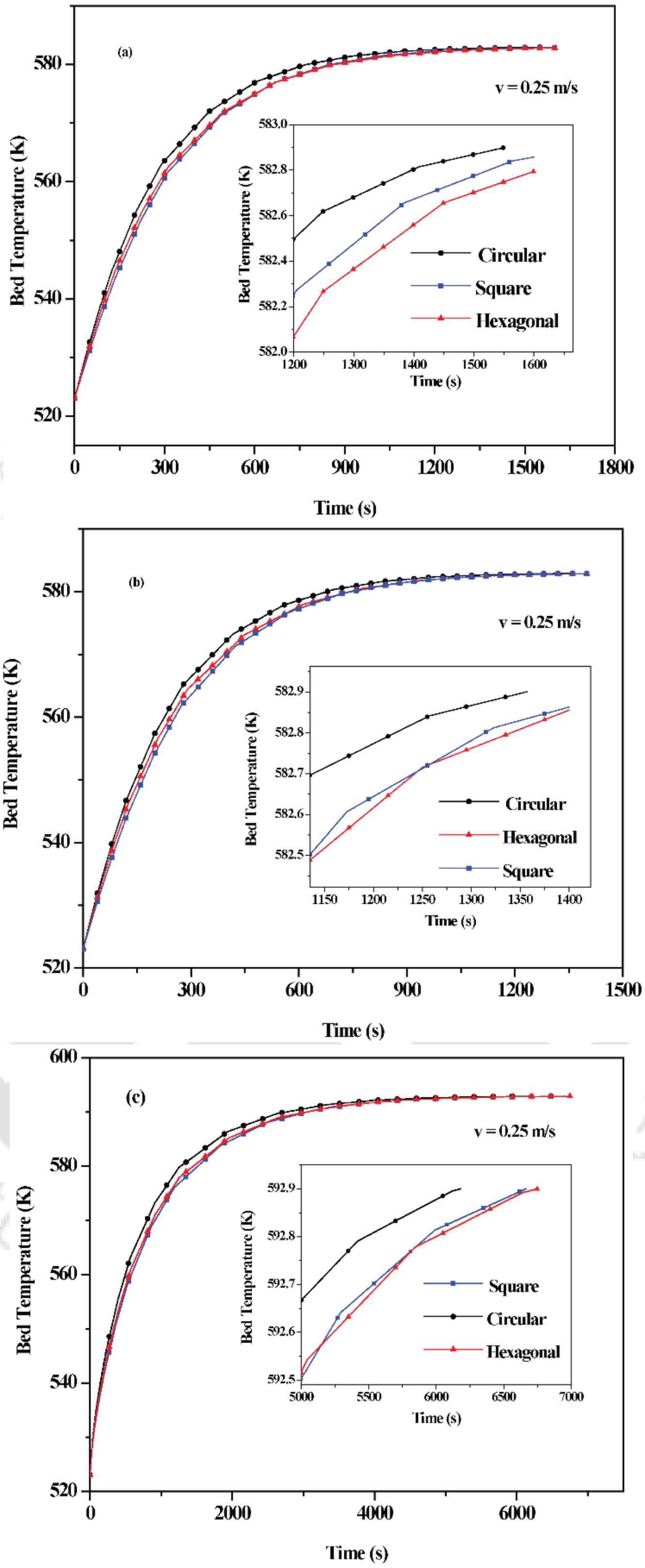

Fig.6. 5 Charging time for (a) cast steel (b) cast iron (c) concrete bed

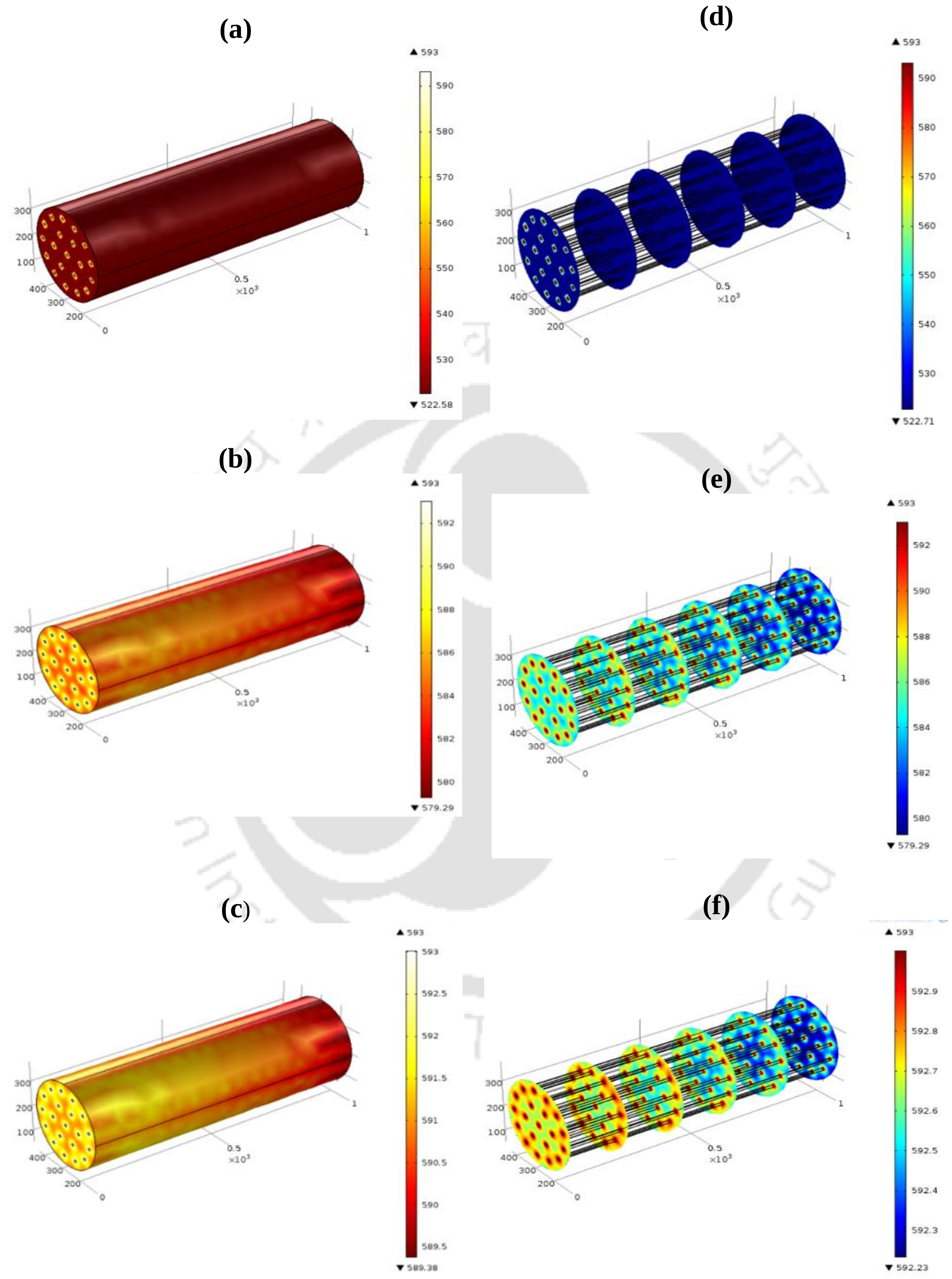

Fig.6. 6 Solid (a-c) and sliced (d-f) views of the temperature distributions inside the concrete bed (a, d) at t = 0 s, (b, e) 2400 s and (c, f) 6200 s during the charging cycle respectively.

6.6.2 Energy stored

The rate of thermal energy stored for the three SHS materials is shown in Fig.6.7 (a-c). For each SHS material, numerical simulation has been performed for three geometrical configurations. The amount of thermal energy stored in different geometries and materials during their respective charging times is estimated by using Eq. (1). For a circular configuration, the amount of thermal energy stored in concrete, cast iron and cast steel beds are 12.63 MJ, 12.7 MJ and 14.74 MJ respectively. It is also observed that the minimum required amount heat (10 MJ) is stored within 302 s for cast steel, 367 s for cast iron and 1177 s for concrete beds. In case of cast steel, increasing the charging time from 302 s to 1552 s, improves the storage capacity by 47.4 %. Similarly, for cast iron and concrete bed, increasing the charging times respectively 367 to 1357 and from 1177 to 6183 improves the storage capacity by 27 % and 26.3 %.

Table 6. 3 Effect of HTF velocity on charging time

SHS material	**HTF velocity (m/s)**	**Charging time(s)**
cast steel	0.25	1552
	0.5	1049
	1	798
cast iron	0.25	1357
	0.5	941
	1	697
concrete	0.25	6183
	0.5	5830
	1	5569

6.6.3 Effect of HTF velocity on charging time

Effect of HTF velocity on charging time for cast steel, cast iron and concrete are presented in Fig.6.8 (a-c), respectively. It is observed that the remarkable reductions in charging times occur due to increase in velocity which in turn increases convective heat transfer, thereby higher energy storage rates are obtained. Charging time of all type of storage beds and SHS materials are given in Table 6.3.

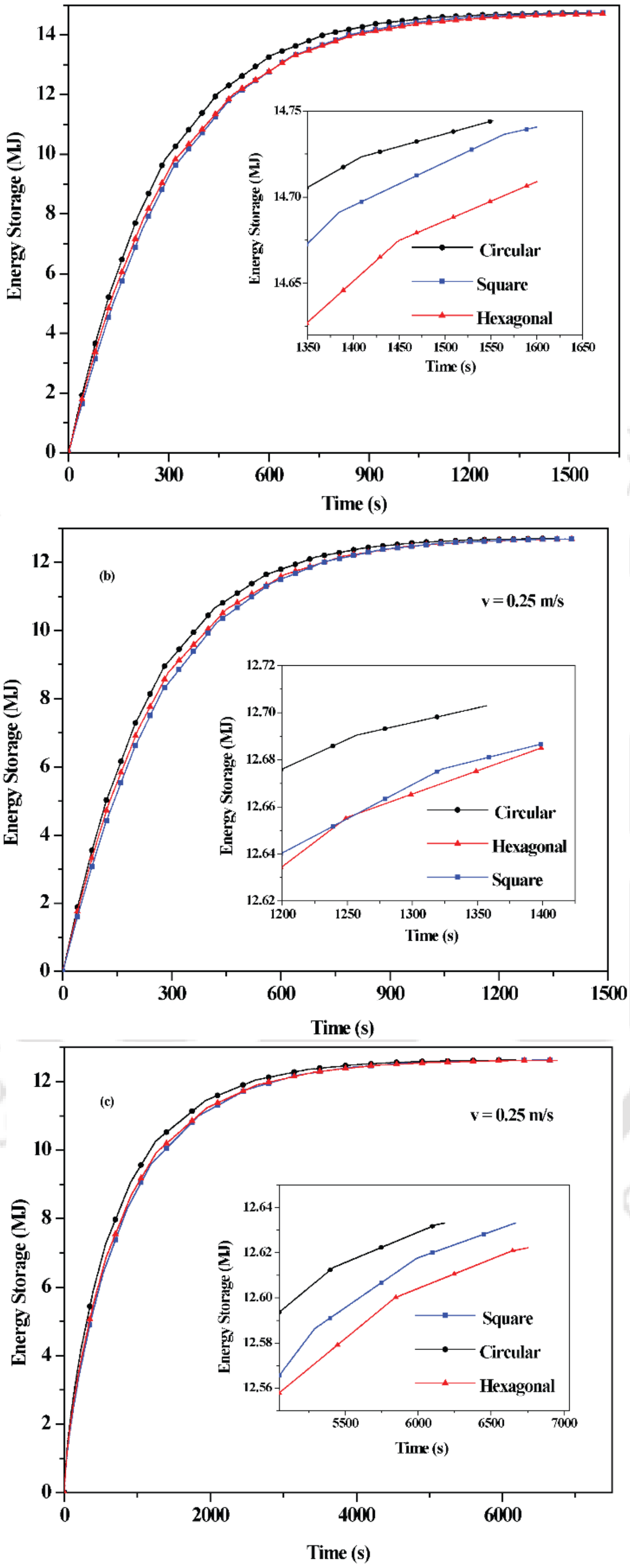

Fig.6. 7 Variation in energy storage rate (a) cast steel (b) cast iron and (c) concrete bed.

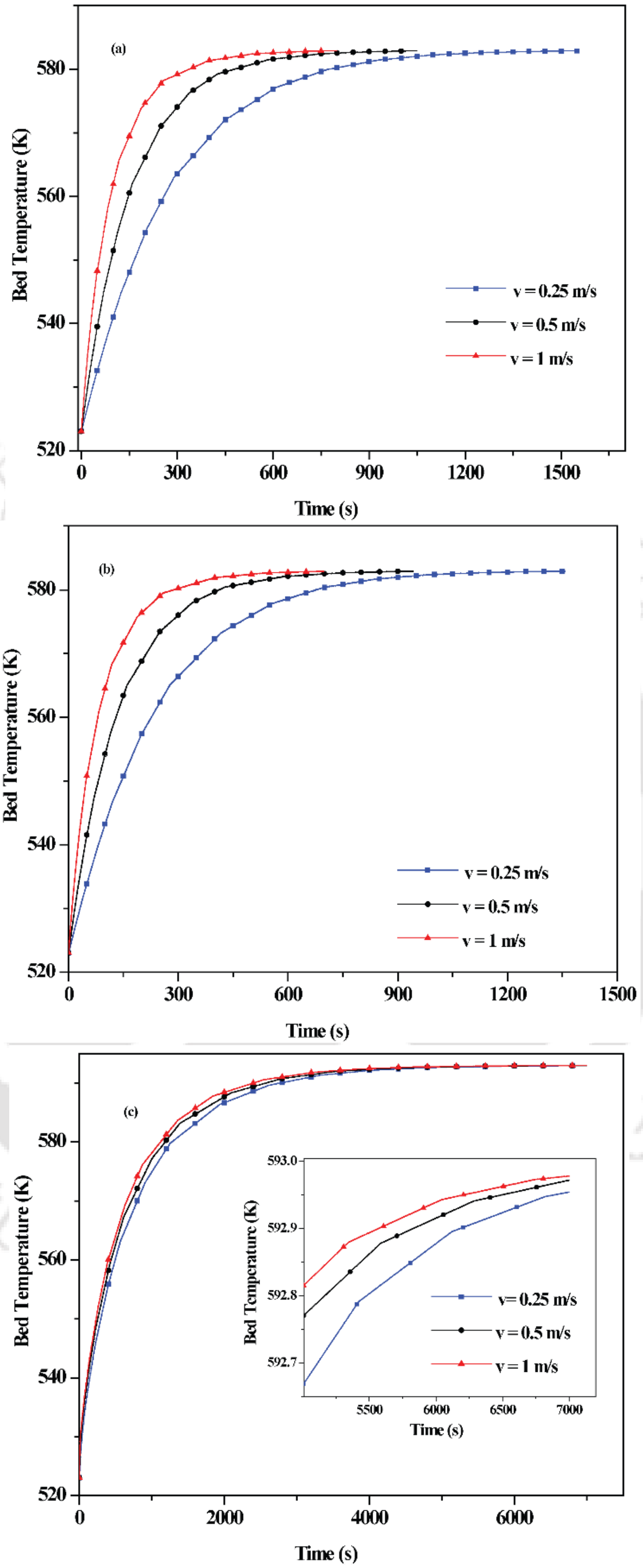

Fig.6. 8 (a-c) Effect of HTF velocity on charging time of cast steel, cast iron and concrete bed respectively.

For metallic storage beds (cast steel & cast iron) the increase in velocity significantly reduces the charging time by almost the same factor while this effect is less for concrete due to low thermal conductivity. For cast steel and cast iron, increasing the HTF velocity from 0.25 to 0.5, reduces the charging time by about 34.41 % and 30.66 %, respectively.

6.7 Summary

The transient behaviour of high temperature lab-scale SHS beds of various geometrical configurations (circular, hexagonal and square) employing three storage materials viz., concrete, cast iron and cast steel has been simulated. The performance parameters such as charging time and amount of heat stored by various geometries have been estimated for selecting a suitable geometrical configuration. It was found that the circular bed is storing the required heat in the least time when compared with other geometries.

- Charging time of cast iron (1357 s) and cast steel (1552 s) are much less than that of concrete bed (6183 s) in circular bed designs.
- Charging time of circular concrete bed (6183 s) is less when compared to its hexagonal (6755 s) and square (6667 s) configurations.
- The effect of HTF velocity on charging time has been presented. For cast iron and cast steel beds, the increase in velocity causes reduction in charging time by almost the same factor while this effect is less in concrete due to low thermal conductivity.

All the materials chosen for the present study such as cast steel, cast iron and concrete are suitable for solid media SHS systems. Among these materials, concrete seems to be most favourable material due to low cost, ease of handling, fabrication and maintenance, provided if the concrete bed yields a minimum charging time.

Chapter 7

Conclusions and Scope for Future Work

The major conclusions drawn from the numerical and experimental studies on the lab-scale SHS prototype are presented in this chapter. A summary of the key outcomes arrived from the numerical studies on different lab scale bed configurations are presented in this chapter. In addition, the thermo-physical properties of the concrete storage material attained during the experimental trails are also presented.

7.1 Measurement of the Thermo-physical Properties

In this section, the measured properties of the test samples of the concrete storage material (Mix design M30), especially the mechanical and thermo-physical properties are discussed. The following are the conclusions drawn from the test samples;

- The mechanical properties of the Mix design M30 (M2/M3 prototypes) i.e., compression and split tensile strength are tested. From the results obtained, the compressive strength of the concrete mix design M30 specimens is acceptable since the observed compressive strength is more than 20 MPa at 28 days. The average split tensile strength of the trails of concrete Mix design M30 at the curing age of 28 days is increased by 60.28 % when compared to the curing age of 7 days.

- The thermo-physical properties of the concrete samples such as volumetric heat capacity and thermal conductivity were measured with the help of a thermal property analyser using the transient plane source technique. It is observed that the thermal conductivity and diffusivity of concrete decreases and the volumetric heat capacity of concrete increases with temperature.

- The maximum uncertainty in the estimation of thermal conductivity, volumetric heat capacity and diffusivity are ±3 %, ±5% and ±3.5 % respectively.

7.2 Experimental Studies

Experimental investigations on the lab-scale SHS prototype was carried out during the charging and discharging cycles. Heat transfer enhancement technique was implemented by the use of longitudinally finned tubes. Performance parameters like charging/discharging time, and energy storage/discharge rate were evaluated at different operating conditions. A detailed parametric study was also conducted at various operating temperature ranges and HTF velocities. The axial and radial temperature distributions of all the prototypes tested were studied. The following conclusions are arrived from the experimental studies:

- Though the experimental set up and all the prototypes have been designed to operate up to 400°C, we could not perform continuous experiments above 250°C during trial experiments because of high vapour pressure and expansion of the HTF. Considering safety issues, operating temperate ranges have been limited to 180°C. However, designed prototypes could be tested up to 400°C using air as heat transfer fluid.
- From experimental studies, the charging/discharging time of the M1 prototype for the temperature range of 353-413 K was found to be 1263/1803 s. The effective charging/discharging time of the M2 and M3 prototypes for the temperature range of 353-433 K were 5210/6297 s and 7160/7780 s, respectively.
- The total amount of energy stored/discharged in the M1 and M2/M3 prototypes at the respective charging/discharging times are 15 MJ and 14.06 MJ, respectively. Maximum uncertainty in the temperature measurement is estimated to be ± 0.5 °C. Similarly, the uncertainty in density/volume/specific heat are estimated / assumed as ± 2% /1 % /2 %. The uncertainties of energy stored/discharged in the cast steel and concrete prototypes are ± 0.66 MJ (± 4.43 %) and ± 0.56 MJ (± 3.98 %), respectively.
- The storage prototypes were tested at three different velocities (v = 0.1, 0.25, 0.5 m/s) and no significant performance improvement is noticed in the case of v = 0.5 m/s when compared with v = 0.25 m/s.

- The storage performance of the system highly depends on the operating temperature range due to the temperature dependence of the thermo-physical properties of the SHS materials and the HTF. The charging and discharging times of cast steel/concrete prototype is less/more at higher operating temperatures. This is due to the increase/decrease of thermal conductivity of cast steel/concrete with the increase of temperature.
- Charging and discharging cycles have been carried out on both cast steel and concrete based SHS prototypes. It was observed that after 150 cycles, no significant performance degradation was observed in cast steel based system.
- However, in the case of concrete SHS prototype embedded with mild steel HTF tube, it was found that the increase in charging time was about 9 % after 100 repeated cycles. Similarly, the respective increase in discharging time was found to be about 12 %. These variations are acceptable and within the limits. Further, it was observed that after 100 cycles of continuous charging and discharging operation, no visible crack was observed on the concrete prototype.

7.3 Numerical studies

The performance of a lab-scale SHS prototype during charging and discharging processes were analysed numerically both at high and intermediate temperatures. Based on the optimizing the number of HTF tubes and fins, a 3D numerical model had been developed. The 3D model developed was based on a conjugate heat transfer problem, which simultaneously solves the behaviour of HTF flow and heat transfer of cast steel (M1) and concrete (M2/M3) storage material. The governing equations of the numerical model were solved using COMSOL Multiphysics 4.3a. The developed model is validated with the experimentally measured temperature data extracted from the in-house lab scale experimental prototype and a close agreement was found between them. Performance parameters such as charging and effective charging / discharging time, energy storage / discharge rate were evaluated at different operating conditions. Heat transfer enhancement technique was implemented by the use of longitudinally finned tubes. A detailed parametric investigation was also conducted at various operating temperature ranges and HTF velocities. The axial and radial temperature distributions of all the prototypes tested were analyzed. The major conclusions deduced from the numerical studies are listed below:

- The transient behaviour of high temperature lab-scale SHS beds of various geometrical configurations (circular, hexagonal and square) employing three storage materials viz., concrete, cast iron and cast steel has been simulated for selecting a suitable geometrical configuration. It was found that the circular bed is storing the required heat in the least time when compared with other geometries.

- From numerical investigation, the charging/discharging time of the M1 bed (cast steel) for the temperature range of 353-413 K is 1106/1572 s. The effective charging/discharging time of the M2 and M3 beds (concrete) for the temperature range of 353-433 K are 4371/5196 s and 6155/6360 s, respectively.

- The storage/discharge heat transfer dynamics is efficient in cast steel prototype than the concrete prototypes due to the higher thermal conductivity of the cast steel. Similarly, M2 prototype showed better storage/discharge performance than the M3 prototype due to the higher effective thermal conductivity of the M2 prototype.

- Though addition of tubes and fins increases the conduction heat transfer during the charging and discharging processes, it slightly retards the convection heat transfer. This necessitates optimizing number of tubes and fins of any storage system.

- It is further observed that, partial charging/discharging process is efficient than complete charging/discharging process for the less thermal conductive SHS materials like concrete ceramic, rock, etc., They take more time to completely charge/discharge due to reduced heat transfer rate between the SHS materials and the HTF. Hence, partial charging/discharging is addressed using a parameter named, effective charging/discharging time.

- With the help of the experimental results obtained, the axial temperature variation at three distinct axial locations recorded is comparatively higher than the radial temperature variation. In the case of prototypes having short length, the deviation between the axial temperatures would be very less.

7.4 Scope for future work from numerical and experimental studies

The works presented in this thesis offer several opportunities to broaden the research work on the SHS systems. Some of them are given below:

- The flow regime of HTF considered in the present numerical study is laminar. Several advantages in the heat transfer rate could be achieved if the study is extended to turbulent regime.

- Storage performance is evaluated for the intermediate temperature range i.e., between 353 K–423 K. Numerical and experimental studies could be carried out at high temperatures using air as the HTF.

- The experimental results of the current lab-scale SHS prototypes may be useful for the design and development of large-scale SHS units, which can be integrated in the real-time solar thermal power plants with the up gradation in the temperature range. Other potential applications are solar drying, solar driven absorption systems, etc. Additionally, the studies presented here may also be helpful in building efficient hybrid storage systems comprising of sensible and latent heat storage modules.

- The storage prototypes of concrete (M2/M3) are filled with the Mix Design M30 in the present study. One can upgrade the Mix Designs by adding the admixtures and filler materials to increase the thermal conductivity of the concrete.

- It is concluded that, the performance of the M1 prototype (cast steel) is advantageous where there is a need for thermal stability, less thermal degradation and higher number of thermal cycles. Similarly, the prototypes M2/M3 are preferred where cost reduction is the prime criteria and also compatible with the locally available cheap resources.

Additionally, the studies presented here facilitate in building efficient hybrid and combined storage systems comprising of sensible and latent heat storage modules.

List of Publications

International Journal Papers

1. Chilaka Ravichandra Rao, Niyas H, P. Muthukumar, Performance Tests on Lab–scale Sensible Heat Storage Prototypes, **Applied Thermal Engineering,** Vol. 129, January 2018, pages 953-967.
2. Niyas H, Chilaka Ravi Chandra Rao, P. Muthukumar, "Performance Investigation of a lab–scale latent heat storage prototype - Experimental results", **Solar Energy**, Vol. 155, October 2017, pages 971-984.
3. Chilaka Ravi Chandra Rao, K. Vigneshwaran, Niyas H., P. Muthukumar, Performance investigation of lab-scale sensible heat storage prototypes (manuscript submitted to **Journal of Energy Storage**).

Book Chapter

1. Chilaka Ravichandra Rao, Hakeem N, Likhendra P and Muthukumar P. Performance Investigation of Lab-Scale Sensible Heat Storage System. Chapter 16, Concentrated Solar Thermal Energy Technologies, Springer Proceedings in Energy, DOI 10.1007/978-981-10-4576-9_16.

International/national Conference Papers

1. Chilaka Ravichandra Rao, P. Muthukumar and C.M.Somayaji (2015) "Performance Comparison of Sensible Heat Storage Beds for Solar Thermal Power Plant Applications", **4th International conference on Polygeneration: Technologies and perspectives**, Anna university, Chennai, India, 18-20 February 2015.

2. Chilaka Ravichandra Rao, Likendra Prasad, P. Muthukumar, and C.M.Somayaji (2016) "Performance Investigation of Lab-Scale Sensible Heat Storage System", **National Conference on Solar Thermal Energy Technologies**, Indian Institute of Technology Jodhpur, Rajasthan, India, 26-28 February 2016.

3. K. Vigneshwaran, Chilaka Ravichandra Rao, P. Muthukumar and S. Senthilmurugan, Sensible Heat Thermal Energy Storage System: Modelling and Simulation, **24th National and 2nd International ISHMT-ASTFE Heat and Mass Transfer Conference (IHMTC-2017)**, IIT Hyderabad and BITS Pilani Hyderabad (Jointly), 27-30 December 201.

References

Al-Nimr, M., Abu-qudais, M.K., Mashaqi, M.D., 1996. Dynamic behaviour of a packed bed energy storage system. *Energy and Conversion Management,* 37(1), 23-30.

Alva, G., Lin, Y.X., Fang, G.Y., 2018. An overview of thermal energy storage systems. *Energy,* 144, 341-378.

Aly, S.L., Elsharkawy, A.I., 1990. Effect of Storage Medium on Thermal-Properties of Packed-Beds. *Heat Recovery Systems and CHP*, 10(5-6), 509-517.

Ammar, A.S.A., Ghoneim, A.A., 1991. Optimization of a sensible heat storage unit packed with spheres of a local material. *Renewable Energy*, 1(1), 91-95.

Andreu-Cabedo, P., Mondragon, R., Hernandez, L., Martinez-Cuenca, R., Cabedo, L., Julia, J.E., 2014. Increment of specific heat capacity of solar salt with SiO2 nanoparticles. *Nanoscale Research Letters*, 9.

Audi, M.S., 1992. Experimental study of a solar space heating model using Jordanian rocks for storage. *Energy and Conversion Management,* 33(9), 833-842.

Bai, F., Xu, C., 2011. Performance analysis of a two-stage thermal energy storage system using concrete and steam accumulator. *Applied Thermal Engineering,* 31(14), 2764-2771.

Beasley, D.E., Clark, J.A., 1984. Transient response of a packed bed for thermal energy storage. *International Journal of Heat and Mass Transfer*, 27(9), 1659-1669.

Beasley, D.E., Clark, J.A., Holstege, M.J., 1985. Observations on the Decay of a Thermocline in a Rock Bed with No Net Fluid-Flow. *Journal of Solar Energy Engineering-Transactions of the ASME,* 107(1), 50-53.

Bejan, A., 1978. Two Thermodynamic Optima in the Design of Sensible Heat Units for Energy Storage. *Journal of Heat Transfer,* 100, 708-712.

Bergan, P.G., Greiner, C.J., 2014. A New Type of Large Scale Thermal Energy Storage. *Energy Procedia,* 58, 152-159.

Bindra, H., Bueno, P., Morris, J.F., Shinnar, R., 2013. Thermal analysis and exergy evaluation of packed bed thermal storage systems. *Applied Thermal Engineering*, 52(2), 255-263.

Birnbaum, J., Eck, M., Fichtner, M., Hirsch, T., Lehmann, D., Zimmermann, G., 2010. A Direct Steam Generation Solar Power Plant With Integrated Thermal Storage. *Journal of Solar Energy Engineering-Transactions of the ASME,* 132(3).

Bradshaw, R.W., Dawson, D.B., De La Rosa, W., Gilbert, R., Goods, S.H., Hale, M.J., Jacobs, P., Jones, S.A., Kolb, G.J., Pacheco, J.E., Prairie, M.R., Reilly, H.E., Showalter, S.K., Vant-Hull, L.L., 2002. *Final Test and Evaluation Results from the Solar Two Project. Sandia National Laboratories.*

Brosseau, D., Kelton, J.W., Ray, D., Edgar, M., Chisman, K., Emms, B., 2005. Testing of thermocline filler materials and molten-salt heat transfer fluids for thermal energy storage systems in parabolic trough power plants. *Journal of Solar Energy Engineering-Transactions of the ASME*, 127(1), 109-116.

Cabeza, L.F., 2012. Thermal energy storage. In: Sayigh, A. (ed.) *Comprehensive Renewable Energy Oxford: Elsevier*, 211–253.

Cascetta, M., Cau, G., Puddu, P., Serra, F., 2014. Numerical Investigation of a Packed Bed Thermal Energy Storage System with Different Heat Transfer Fluids. *Energy Procedia,* 45, 598-607.

Castro, M., Presa, J.L., Diaz, J., Peire, J., Baker, A.F., Faas, S.E., Radosevich, L.G., Skinrood, A.C., 1991. Crs Receiver and Storage-Systems Evaluation. *Solar Energy*, 47(3), 197-207.

Chandra, P., Willits, D.H., 1981. Pressure drop and heat transfer characteristics of air-rockbed thermal storage systems. *Solar Energy*, 27(6), 547-553.

Colburn, A.P., 1931. Heat Transfer and Pressure Drop in Empty, Baffled, and Packed Tubes1. *Industrial & Engineering Chemistry,* 23(8), 910-913.

Coutier, J.P., Farber, E.A., 1982. Two applications of a numerical approach of heat transfer process within rock beds. *Solar Energy,* 29(6), 451-462.

Dersch, J., Vogel, T., Polklas, T., Tümmers, C., 2014. Solar-only Parabolic Trough Plants with High Steam Parameters. *Energy Procedia,* 49, 1117-1126.

Dincer I, Rosen,M.A., 2002. Thermal energy storage (TES) methods. In: Dincer, I. and Rosen, M.A. (eds) *Thermal Energy Storage: Systems and Applications*, New York: John Wiley & Sons. 93–212.

Dinter, F., Geyer, M., Tamme, R., 1990. Thermal Energy Storage for Commercial Applications. *Springer-Verlag, New York.*

Domanski, R., Fellah, G., 1996. Exergy analysis for the evaluation of a thermal storage system employing PCMs with different melting temperatures. *Applied Thermal Engineering*, 16(11), 907-919.

Dreissigacker, V., Muller-Steinhagen, H., Zunft, S., 2010. Thermo-mechanical analysis of packed beds for large-scale storage of high temperature heat. *Heat Mass Transfer,* 46(10), 1199-1207.

Eames, P.C., Norton, B., 1998. The effect of tank geometry on thermally stratified sensible heat storage subject to low Reynolds number flows. *International Journal of Heat and Mass Transfer,* 41(14), 2131-2142.

Eck, M., Zarza, E., Eickhoff, M., Rheinlander, J., Valenzuela, L., 2003. Applied research concerning the direct steam generation in parabolic troughs. *Solar Energy,* 74(4), 341-351.

El-Kassaby, M.M., Ghoneim, A.A., 1993. Comparison of measured and predicted performance of different heat storage systems. *Renewable Energy,* 3(8), 849-856.

Elsayed, M.M., Megahed, E., El-Refaee, M.M., 1988. Experimental testing of fluidized bed thermal storage. *Solar & Wind Technology,* 5(1), 15-25.

Fernandes, D., Pitie, F., Caceres, G., Baeyens, J., 2012. Thermal energy storage: "How previous findings determine current research priorities". *Energy,* 39(1), 246-257.

Fernandez, A.I., Martinez, M., Segarra, M., Martorell, I., Cabeza, L.F., 2010. Selection of materials with potential in sensible thermal energy storage. *Solar Energy Materials and Solar Cells*, 94(10), 1723-1729.

Fricker, H.W., 1991. High-Temperature Heat-Storage Using Natural Rock. *Solar Energy Materials and Solar Cells,* 24(1-4), 249-254.

Furnas, C.G., 1930. Heat Transfer from a gas Stream to bed of Broken Solids. *Industrial & Engineering Chemistry,* 22(1), 26-31.

Garg, H.P., Mullick, S.C., Bhargava, A.K., 1985. Solar thermal energy storage. *Springer, New York.*

Gil, A., Medrano, M., Martorell, I., Lazaro, A., Dolado, P., Zalba, B., Cabeza, L.F., 2010. State of the art on high temperature thermal energy storage for power generation. Part 1-Concepts, materials and modellization. *Renewable & Sustainable Energy Reviews*, 14(1), 31-55.

Gluck, A., Tamme, R., Kalfa, H., Streuber, C., 1991. Investigation of high temperature storage materials in a technical scale test facility. *Solar Energy Materials and Solar Cells*, 24(1), 240-248.

Grirate, H., Agalit, H., Zari, N., Elmchaouri, A., Molina, S., Couturier, R., 2016. Experimental and numerical investigation of potential filler materials for thermal oil thermocline storage. *Solar Energy*, 131, 260-274.

Guo, C., Zhu, J., Zhou, W., Chen, W., 2010. Fabrication and thermal properties of a new heat storage concrete material. *Journal of Wuhan University of Technology-Material Science*, 25(4), 628-630.

Guo, Z.Y., 2001. Mechanism and control of convective heat transfer - Coordination of velocity and heat flow fields. *Chinese Science Bulletin*, 46(1), 596-599.

Gustafsson, S.E., 1991. Transient Plane Source Techniques for Thermal-Conductivity and Thermal-Diffusivity Measurements of Solid Materials. *Review of Science Instruments*, 62(3), 797-804.

Hanchen, M., Bruckner, S., Steinfeld, A., 2011. High-temperature thermal storage using a packed bed of rocks - Heat transfer analysis and experimental validation. *Applied Thermal Engineering*, 31(10), 1798-1806.

Handley, D., Heggs, P.J., 1969. The effect of thermal conductivity of the packing material on transient heat transfer in a fixed bed. *International Journal of Heat and Mass Transfer*, 12, 549-570.

Hasnain, S.M., 1998. Review on sustainable thermal energy storage technologies, part I: Heat storage materials and techniques. *Energy and Conversion Management*, 39(11), 1127 1138.

Herrmann, U., Kearney, D.W., 2002. Survey of thermal energy storage for parabolic trough power plants. *Journal of Solar Energy Engineering-Transactions of the ASME*, 124(2), 145-152.

Herrmann, U., Kelly, B., Price, H., 2004. Two-tank molten salt storage for parabolic trough solar power plants. *Energy*, 29(5-6), 883-893.

Hill, J.E., Kelly, G.E., Peavy, B.A., 1977. A method of testing for rating thermal storage devices based on thermal performance. *Solar Energy*, 19(6), 721-732.

Hollands, K.G.T., Sullivan, H.F., 1984. Pressure drops across rock bed thermal storage systems. *Solar Energy*, 33(2), 221-225.

Horn, M., Führing, H., Rheinländer, J., 2004. Economic analysis of integrated solar combined cycle power plants: A sample case: The economic feasibility of an ISCCS power plant in Egypt. *Energy*, 29(5), 935-945.

Hosseini, R., Soltani, M., Valizadeh, G., 2005. Technical and economic assessment of the integrated solar combined cycle power plants in Iran. *Renewable Energy*, 30(10), 1541-1555.

Ismail, K.A.R., Stuginsky, R., 1999. A parametric study on possible fixed bed models for pcm and sensible heat storage. *Applied Thermal Engineering* , 19(7), 757-788.

Jalalzadeh-Azar A., Steele, W., Adebiyi, G., 1997. Performance comparison of high-temperature packed bed operation with PCM and sensible-heat pellets. *International Journal of Energy Research*, 21,1039-1052.

Jemmal, Y., Zari, N., Maaroufi, M., 2016. Thermophysical and chemical analysis of gneiss rock as low cost candidate material for thermal energy storage in concentrated solar power plants. *Solar Energy Materials and Solar Cells*, 157, 377-382.

Jemmal, Y., Zari, N., Maaroufi, M., 2017. Experimental characterization of siliceous rocks to be used as filler materials for air-rock packed beds thermal energy storage systems in concentrated solar power plants. *Solar Energy Materials and Solar Cells*, 171, 33-42.

Jian, Y., Bai, F., Falcoz, Q., Wang, Z., 2015. Control Strategy of the Module Concrete Thermal Energy Storage for Parabolic Trough Power Plants. *Energy Procedia*, 69, 891-899.

John, E., Hale, M., Selvam, R.P., 2010. Effect of High Temperatures and Heating Rates on High Strength Concrete for Use as Thermal Energy Storage. *Proceedings of the ASME 2010 4th International Conference on Energy Sustainability, Phoenix, Arizona, USA.* ES2010-90096, 709-713.

John, E.E., Hale, W.M., Selvam, R.P., 2011. Development of a High-Performance Concrete to Store Thermal Energy for Concentrating Solar Power Plants. *In: Proceedings of ASME 2011 5th International Conference on Energy Sustainability, Washington, DC.* ES2011-54177, 523-529.

John, E., Hale, M., Selvam, R.P., 2013. Concrete as a thermal energy storage medium for thermocline solar energy storage systems. *Solar Energy*, 96, 194-204.

Kandari, A.M., 1990. Thermal Stratification in Hot Storage-Tanks. *Applied Energy*, 35(4), 299-315.

Kearney, D., Herrmann, U., Nava, P., Kelly, P., Mahoney, R., Pacheco, J., Cable, R., Potrovitza, N., Blake, D., Price, H., 2003. Assessment of a molten salt heat transfer fluid in a parabolic trough solar field. *Journal of Solar Energy Engineering-Transactions of the ASME*, 125(2), 170-176.

Kearney, D., Kelly, B., Herrmann, U., Cable, R., Pacheco, J., Mahoney, R., Price, H., Blake, D., Nava, P., Potrovitza, N., 2004. Engineering aspects of a molten salt heat transfer fluid in a trough solar field. *Energy*, 29(5-6), 861-870.

Kelly, B.D., Herrmann, U., 2000. ‘‘Evaluation and Performance Modeling for Integrated Solar Combined Cycle Systems and Thermal Storage System,’’ *Final Report Prepared for NREL, Contract Number* RAR-9-29442-05.

Khare, S., Dell'Amico, M., Knight, C., McGarry, S., 2013. Selection of materials for high temperature sensible energy storage. *Solar Energy Materials and Solar Cells*, 115, 114-122.

Kline, S.J., McClintock, F.A., 1953. Describing uncertainties in single-sample experiments. *Mechanical Engineering*, 3-12.

Klein, P., Roos, T.H., Sheer, T.J., 2014. Experimental Investigation into a Packed Bed Thermal Storage Solution for Solar Gas Turbine Systems. *Energy Procedia*, 49, 840-849.

Kodur, V.K.R., Sultan, M.A., 2003. Effect of temperature on thermal properties of high-strength concrete. *Journal of Materials in Civil Engineering*, 15(2), 101-107.

Krane, R.J., 1987. A second law analysis of the optimum design and operation of thermal energy storage systems. *International Journal of Heat and Mass Transfer*, 30, 43-57.

Kumaresan, G., Velraj, R., Iniyan, S., 2011. Thermal Analysis of D-mannitol for Use as Phase Change Material for Latent Heat Storage. *Journal of Applied Sciences*, 11(16), 3044-3048.

Kuravi, S., Trahan, J., Goswami, D.Y., Rahman, M.M., Stefanakos, E.K., 2013. Thermal energy storage technologies and systems for concentrating solar power plants. *Progress in Energy and Combustion Science*, 39(4), 285-319.

Laing, D., Bahl, C., Bauer, T., Lehmann, D., Steinmann, W.-D., 2011. Thermal energy storage for direct steam generation. *Solar Energy*, 85(4), 627-633.

Laing, D., Bauer, T., Lehmann, D., Bahl, C., 2010. Development of a Thermal Energy Storage System for Parabolic Trough Power Plants With Direct Steam Generation. *Journal of Solar Energy Engineering-Transactions of the ASME*, 132(2).

Laing, D., Lehmann, D., Fiß, M., Bahl, C., 2009. Test Results of Concrete Thermal Energy Storage for Parabolic Trough Power Plants. *Journal of Solar Energy Engineering-Transactions of the ASME*, 131(4), 041007-041007-041006.

Laing, D., Steinmann, W.D., Fiss, M., Tamme, R., Brand, T., Bahl, C., 2008. Solid media thermal storage development and analysis of modular storage operation concepts for parabolic trough power plants. *Journal of Solar Energy Engineering-Transactions of the ASME*, 130(1), 011006-011006-5.

Laing, D., Steinmann, W.D., Tamme, R., Richter, C., 2006. Solid media thermal storage for parabolic trough power plants. *Solar Energy*, 80(10), 1283-1289.

Lavan, Z., Thompson, J., 1977. Experimental-Study of Thermally Stratified Hot Water Storage Tanks. *Solar Energy*, 19(5), 519-524.

Littman, H., Barile, R.G., Pulsifer, A.H., 1968. Gas-Particle Heat Transfer Coefficients in Packed Beds at Low Reynolds Numbers. *Industrial & Engineering Chemistry Fundamentals*, 7(4), 554-561.

Lof, G.O.G., Hawley, R.W., 1948. Unsteady-State Heat Transfer between air and loose solids. *Industrial & Engineering Chemistry*, 40(6), 1061-1070.

M. Waked, A., 1986. Solar energy storage in rocks.*Solar & Wind Technology*, 3(1), 27-31.

Mao, Q.J., 2016. Recent developments in geometrical configurations of thermal energy storage for concentrating solar power plant. *Renewable & Sustainable Energy Reviews*, 59, 320-327.

Markus Eck, Martin Eickhoff, Pablo Fontela, Doerte Laing, Mirko Meyer-Grunefeldt, Marc Mollenhoff, Marcus Nolke, Francisco Ortiz Vives, Klaus-Jurgen Riffelmann, Andres Sanchez-Biezma, Bahl, C., 2009. Test and Demonstration of the Direct Steam Generation (DSG) at 500°C. *SolarPACES 2009 - Electricity, fuels and clean water powered by the sun*, 15.-18. Sep. 2009, Berlin, Germany.

Mawire, A., McPherson, M., 2009. Experimental and simulated temperature distribution of an oil-pebble bed thermal energy storage system with a variable heat source. *Applied Thermal Engineering*, 29(5-6), 1086-1095.

Mawire, A., McPherson, M., van den Heetkamp, R.R.J., Mlatho, S.J.P., 2009. Simulated performance of storage materials for pebble bed thermal energy storage (TES) systems. *Applied Energy*, 86(7-8), 1246-1252.

Mazzucco, G., Xotta, G., Salomoni, V.A., Giannuzzi, M., Maiorana, C.E., 2017. Solid thermal storage with PCM materials. Numerical investigations. *Applied Thermal Engineering*, 124, 545-559.

Medrano, M., Gil, A., Martorell, I., Potau, X., Cabeza, L.F., 2010. State of the art on high-temperature thermal energy storage for power generation. Part 2-Case studies. *Renewable & Sustainable Energy Reviews*, 14(1), 56-72.

Mehling, H., Cabeza, L.F., 2010. *Heat and cold storage with PCM: An up to date introduction into basics and applications*. Springer Berlin Heidelberg.

Meier, A., Winkler, C., Wuillemin, D., 1991. Experiment for Modeling High-Temperature Rock Bed Storage. *Solar Energy Materials and Solar Cells,* 24(1-4), 255-264.

Mirzanamadi, R., Johansson, P., Grammatikos, S.A., 2018. Thermal properties of asphalt concrete: A numerical and experimental study. *Construction and Building Materials*, 158, 774-785.

Moffat, R.J., 1982. Contributions to the theory of single-sample uncertainty analysis, *Journal of Fluids Engineering- Transactions of the Asme*, 104(2), 250–260.

Montanes, R.M., Windahl, J., Pålsson, J., Thern, M., 2018. Dynamic Modeling of a Parabolic Trough Solar Thermal Power Plant with Thermal Storage Using Modelica. *Heat Transfer Engineering,* 39(3), 277-292.

Montes, M.J., Abanades, A., Martinez-Val, J.M., 2009. Performance of a direct steam generation solar thermal power plant for electricity production as a function of the solar multiple. *Solar Energy*, 83(5), 679-689.

Muller-Steinhagen, H., Nitsch, J., 2005. The contribution of renewable energies to a sustainable energy economy. *Process Safety and Environmental Protection*, 83(4), 285-297.

Nallusamy, N., Sampath, S., Velraj, R., 2007. Experimental investigation on a combined sensible and latent heat storage system integrated with constant/varying (solar) heat sources. *Renewable Energy*, 32(7), 1206-1227.

Nandi, B.R., Bandyopadhyay, S., Banerjee, R., 2012. Analysis of high temperature thermal energy storage for solar power plant, *IEEE Third International Conference on Sustainable Energy Technologies (ICSET)*, 438-444.

National Renewable Energy Laboratory. Accessed on 28.02.18 and available from: (*https://www.nrel.gov/csp/solarpaces/by_project.cfm*).

Navarro, M.E., Martínez, M., Gil, A., Fernández, A.I., Cabeza, L.F., Olives, R., Py, X., 2012. Selection and characterization of recycled materials for sensible thermal energy storage. *Solar Energy Materials and Solar Cells*, 107, 131-135.

Niyas, H., Prasad, L., Muthukumar, P., 2015. Performance investigation of high-temperature sensible heat thermal energy storage system during charging and discharging cycles. *Clean Technol Envir* 17(2), 501-513

Nsofor, E.C., Adebiyi, G.A., 2001. Measurements of the gas-particle convective heat transfer coefficient in a packed bed for high-temperature energy storage. *Experimental Thermal and Fluid Science*, 24(1), 1-9.

Oro, E., Gil, A., de Gracia, A., Boer, D., Cabeza, L.F., 2012. Comparative life cycle assessment of thermal energy storage systems for solar power plants. *Renewable Energy*, 44, 166-173.

Ozger, O.B., Girardi, F., Giannuzzi, G.M., Salomoni, V.A., Majorana, C.E., Fambri, L., Baldassino, N., Di Maggio, R., 2013. Effect of nylon fibres on mechanical and thermal properties of hardened concrete for energy storage systems. *Materials & Design*, 51, 989-997.

Ozturk, H.H., Başçetinçelik, A., 2003. Energy and Exergy Efficiency of a Packed-bed Heat Storage Unit for Greenhouse Heating. *Biosystems Engineering,* 86(2), 231-245.

Pacheco, J.E., Showalter, S.K., Kolb, W.J., 2002. Development of a molten-salt thermocline thermal storage system for parabolic trough plants. *Journal of Solar Energy Engineering-Transactions of the ASME*, 124(2), 153-159.

Pantaleo, A.M., Camporeale, S.M., Miliozzi, A., Russo, V., Mugnozza, G.S., Markides, C.N., Shah, N., 2017. Thermo-economic Assessment of an Externally Fired Hybrid CSP/biomass Gas Turbine and Organic Rankine Combined Cycle. *Energy Procedia*, 105, 174-181.

Pelay, U., Lu, L.A., Fan, Y.L., Stitou, D., Rood, M., 2017. Thermal energy storage systems for concentrated solar power plants. *Renewable & Sustainable Energy Reviews*, 79, 82-100.

Perez M, R, P., 2015. Update 2015-A Fundamental look at supply side energy reserves for the planet. *Natural Gas*, 2 (9), 215.

Prasad, L., Muthukumar, P., 2013. Design and optimization of lab-scale sensible heat storage prototype for solar thermal power plant application. *Solar Energy*, 97, 217-229.

Prieto, C., Rodriguez, A., Patino, D., Cabeza, L.F., 2018. Thermal energy storage evaluation in direct steam generation solar plants. *Solar Energy*, 159, 501-509.

Rao, C.R.C., Niyas, H., Prasad, L., Palanisamy, M., 2018. Performance Investigation of Lab-Scale Sensible Heat Storage System. *Proceedings of Concentrated Solar Thermal Energy Technologies, Springer Singapore*, 169-186.

Reddy, K.S., Kumar, K.R., 2012. Solar collector field design and viability analysis of stand-alone parabolic trough power plants for Indian conditions. *Energy for Sustainable Development*, 16(4), 456-470.

Reddy, V.M., 2012. Flexural behaviour of steel fiber reinforced high strength rice husk ash cement concrete simply supported beams. *International Journal of Civil and Structural Engineering*, 2(4), 1138–1143.

Reddy, V.S., Kaushik, S.C., Ranjan, K.R., Tyagi, S.K., 2013. State-of-the-art of solar thermal power plants-A review. *Renewable & Sustainable Energy Reviews*, 27, 258-273.

Riaz, M., 1977. Analytical Solutions for Singleand Two-Phase Models of Packed-Bed Thermal Storage Systems. *Journal of Heat Transfer*, 99, 489-492.

Rohsenow, W.M., Hartnett, J.P., Cho, Y.I., 1998. Handbook of Heat Transfer. *Tata McGraw Hill.*

Rosen, M.A., 2001. The exergy of stratified thermal energy storages. *Solar Energy*, 71(3), 173-185.

Sagara, K., Nakahara, N., 1991. Thermal performance and pressure drop of rock beds with large storage materials. *Solar Energy*, 47(3), 157-163.

Sawin JL, Sverrisson F, Seyboth K, Adib R, Murdock HE, C, L., 2016. *Renewables 2016 Global Status Report Key findings - A Record Breaking Year for Renewable Energy: New Installations, Policy Targets, Investment and Jobs mainstreaming renewables.*

Schenk, O., Gärtner, K., 2004. Solving unsymmetric sparse systems of linear equations with PARDISO. *Future Generation Computer Systems*, 20(3), 475-487.

Schlipfa, D., Schicktanza, P., Maiera, M., Schneider, G., 2015. Using sand and other small grained materials as heat storage medium in a packed bed HTTESS. *Energy Procedia*, 00, 000-000.

Schumann, T.E.W., 1929. Heat transfer: A liquid flowing through a porous prism. *Journal of the Franklin Institute*, 208(3), 405-416.

Selvam, R.P., Castro, M., 2010. 3D FEM Model to Improve the Heat Transfer in Concrete for Thermal Energy Storage in Solar Power Generation. *Proceedings of the ASME 2010 4th International Conference on Energy Sustainability, Phoenix, Arizona, USA*, 1-9.

Shin, K.Y., Kim, S.B., Kim, J.H., Chung, M., Jung, P.S., 2002. Thermo-physical properties and transient heat transfer of concrete at elevated temperatures. *Nuclear Engineering and Design*, 212(1-3), 233-241.

Shitzer, A., Levy, M., 1983. Transient-Behavior of a Rock-Bed Thermal Storage-System Subjected to Variable Inlet Air Temperatures - Analysis and Experimentation. *Journal of Solar Energy Engineering-Transactions of the ASME*, 105(2), 200-206.

Singh, R., Saini, R.P., Saini, J.S., 2006. Nusselt number and friction factor correlations for packed bed solar energy storage system having large sized elements of different shapes. *Solar Energy*, 80(7), 760-771.

Skinner, J.E., Brown, B.M., Selvam, R.P., 2011. Testing of High Performance Concrete as a Thermal Energy Storage Medium at High Temperatures. *ASME 5th International Conference on Energy Sustainability*, ES2011-54463, 723-728.

Skinner, J.E., Strasser, M.N., Brown, B.M., Panneer Selvam, R., 2013. Testing of High-Performance Concrete as a Thermal Energy Storage Medium at High Temperatures. *Journal of Solar Energy Engineering-Transactions of the ASME*, 136(2), 021004-021004-6.

Sorour, M.M., 1988. Performance of a small sensible heat energy storage unit. *Energy and Conversion Management*, 28(3), 211-217.

Sragovich, D., 1989. Transient Analysis for Designing and Predicting Operational Performance of a High-Temperature Sensible Thermal-Energy Storage-System. *Solar Energy*, 43(1), 7-16.

Standish, N., Drinkwater, J.B., 1970. The effect of particle shape on flooding rates in packed columns. *Chemical Engineering Science*, 25(10), 1619-1621.

Steinmann, W.D., Laing, D., Tamme, R., 2009. Development of PCM Storage for Process Heat and Power Generation. *Journal of Solar Energy Engineering-Transactions of the ASME*, 131(4). 041009-041009-4.

Strasser, M.N., Selvam, R.P., 2014. A cost and performance comparison of packed bed and structured thermocline thermal energy storage systems. *Solar Energy*, 108, 390-402.

Suleiman, B.M., 2011. Measurements of Thermal Conduction in Partially Saturated Specimens Using the Transient Hot-Disk Technique. *Journal of Testing and Evaluation*, 39(4), 529-534.

Tamme, R., Laing, D., Steinmann, W.-D., 2003. Advanced Thermal Energy Storage Technology for Parabolic Trough. *Proceedings of ASME International Solar Energy Conference, Kohala Coast, Hawaii, USA, March 15–18. ISEC2003-44033*, 563-571.

Tamme, R., Laing, D., Steinmann, W.D., 2004. Advanced thermal energy storage technology for parabolic trough. *Journal of Solar Energy Engineering-Transactions of the ASME*, 126(2), 794-800.

Tian, Y., Zhao, C.Y., 2013. A review of solar collectors and thermal energy storage in solar thermal applications. *Applied Energy*, 104, 538-553.

Vaivudh, S., Rakwichian, W., Chindaruksa, S., 2008. Heat transfer of high thermal energy storage with heat exchanger for solar trough power plant. *Energy Conversion and Management*, 49(11), 3311-3317.

Van Lew, J.T., Li, P.W., Chan, C.L., Karaki, W., Stephens, J., 2011. Analysis of Heat Storage and Delivery of a Thermocline Tank Having Solid Filler Material. *Journal of Solar Energy Engineering-Transactions of the ASME*, 133(2), 021003-021003-10.

Wang, K.Y., West, R.E., Kreith, F., Lynn, P., 1985. High-Temperature Sensible-Heat Storage Options. *Energy*, 10(10), 1165-1175.

Wu, M., Li, M.J., Xu, C., He, Y.L., Tao, W.Q., 2014. The impact of concrete structure on the thermal performance of the dual-media thermocline thermal storage tank using concrete as the solid medium. *Applied Energy*, 113, 1363-1371.

Xu, B., Han, J., Kumar, A., Li, P., Yang, Y., 2017. Thermal storage using sand saturated by thermal-conductive fluid and comparison with the use of concrete. J*ournal of Energy Storage*, 13, 85-95.

Xu, B., Li, P.W., Chan, C.L., 2012. Extending the validity of lumped capacitance method for large Biot number in thermal storage application. *Solar Energy*, 86(6), 1709-1724.

Xu, C., Wang, Z.F., He, Y.L., Li, X., Bai, F.W., 2012. Sensitivity analysis of the numerical study on the thermal performance of a packed-bed molten salt thermocline thermal storage system. *Applied Energy*, 92, 65-75.

Xu, E., Yu, Q., Wang, Z., Yang, C., 2011. Modeling and simulation of 1 MW DAHAN solar thermal power tower plant. *Renewable Energy*, 36(2), 848-857.

Yang, Z., Garimella, S.V., 2010a. Molten-salt thermal energy storage in thermoclines under different environmental boundary conditions. *Applied Energy*, 87(11), 3322-3329.

Yang, Z., Garimella, S.V., 2010b. Thermal analysis of solar thermal energy storage in a molten-salt thermocline. *Solar Energy*, 84(6), 974-985.

Zanganeh, G., Commerford, M., Haselbacher, A., Pedretti, A., Steinfeld, A., 2014. Stabilization of the outflow temperature of a packed-bed thermal energy storage by combining rocks with phase change materials. . *Applied Thermal Engineering* , 70(1), 316-320.

Zanganeh, G., Pedretti, A., Zavattoni, S., Barbato, M., Steinfeld, A., 2012. Packed-bed thermal storage for concentrated solar power - Pilot-scale demonstration and industrial-scale design. *Solar Energy*, 86(10), 3084-3098.

Zarza, E., Rojas, M.E., Gonzalez, L., Caballero, J.M., Rueda, F., 2006. INDITEP: The first pre-commercial DSG solar power plant. *Solar Energy*, 80(10), 1270-1276.

Zavattoni, S.A., Barbato, M.C., Pedretti, A., Zanganeh, G., Steinfeld, A., 2014. High Temperature Rock-bed TES System Suitable for Industrial-scale CSP Plant – CFD Analysis Under Charge/Discharge Cyclic Conditions. *Energy Procedia*, 46, 124-133.

Appendix – A

Mix design of M30 Grade Mix

The proportioning of M30 using the proposed mix design method is presented below:

I. Stipulations for mix proportioning

1.1 Characteristic strength of concrete specified (f_{ck}): 30 N/mm^2

1.2 Maximum size of aggregate to be used: 10 mm (annular)

1.3 Degree of workability – (slump): 0.8 C.F

1.4 Exposure condition specified: Mild

1.5 Degree of quality control expected: Good

II. Test data of materials

2.1 Specific gravity of cement (OPC) = 3.02

2.2 Specific gravity of coarse aggregate = 2.72

2.3 Specific gravity of fine aggregate = 2.63

2.4 Water absorption of coarse aggregate = 0.5%

2.5 Water absorption of fine aggregate = 1%

2.6 Free (Surface) moisture for coarse and fine aggregates = Nil & 2% respectively

2.7 Absorbed moisture for coarse and fine aggregates = Nil & 1% respectively

2.8 Grading of Fine Aggregate (FA)

Sieve Size	Percentage passing
4.75 mm	98.6
2.36 mm	95.2
1.18 mm	83
600 microns	50.8
300 microns	17.5
150 microns	1.4
75 microns	0.4

2.9 Grading of Coarse Aggregate (CA)

Sieve Size	Percentage passing
6.3 mm	100
4.75 mm	31.8
2.36 mm	3.4
1.18 mm	0.05

III. Mix design

10 mm MSA, C.F = 0.80, W/C Ratio = 0.55

3.1 Standard deviation (from table 2, IS 456-2000 for good control) = 5 N/mm^2

3.2 Target average 28-day compressive strength of concrete

$$f'ck = fck + 1.65 \times S$$

$$= 30 + 1.65 \times 5$$

$$= 38.5 \text{ N/mm}^2$$

3.3 Water – cement ratio = 0.49 (from Fig.2. IS 10262-1982)

3.4 Maximum water – cement ratio specified for durability condition = 0.45 (from Table-3)

3.5 Water–cement ratio to be adopted for concrete = 0.45

3.6 Water content from Table -5 = 208 lit. (for a workability of 0.80 C F)

3.7 Sand as percentage of total aggregate by absolute volume from Table- 5 = 40% for W/C ratio of 0.60

3.8 Cement content = 206/0.45 = 457.8 kg/m^3

3.9 Minimum Cement content = 350 kg/m^3 (from Table-3 specified for durability condition)

3.10 Required Cement content = 425.8 kg/m^3 (Higher of 4.12 and 4.13)

3.11 Entrapped air, as percentage of volume of concrete = 3 %

3.12 Sand content

$$V=\left[W+\frac{C}{S_C}+\frac{1}{(p)}\cdot\frac{f_a}{S\,f_a)}\right]\times\frac{1}{1000}$$

$$(1-0.03)=\left[208+\frac{462.2}{3.02}+\frac{1}{(0.4)}\cdot\frac{f_a}{2.63}\right]\times\frac{1}{1000}$$

$f_a=633.31$ kg/m^3

3.13 Coarse aggregate content

$$V=\left[W+\frac{C}{S_C}+\frac{1}{(1-p)}\cdot\frac{C_a}{S\,C_a)}\right]\times\frac{1}{1000}$$

$$(1-0.03)=\left[208+\frac{462.2}{3.02}+\frac{1}{(1-0.4)}\cdot\frac{C_a}{2.72}\right]\times\frac{1}{1000}$$

$C_a=993.89$ kg/m^3.

3.14 Extra water required for absorption of coarse aggregate = (@ 0.5%) x 993.89 = 5 litre

3.15 Extra water available as surface moisture in fine aggregate = (@ 2.0%) x 633.31 = 13 litre

3.16 Actual quantity of water to be added = 208 + 5-13 = 200 litre

3.17 Actual quantity of sand = 633.31 x 1.02 = 645.97 kg

3.18 Actual quantity of coarse aggregate = 633.31 /1.005 = 630.16 kg

Note: Similar analysis has been done while preparing the samples of the other Mix Designs *viz.*, from M20 to M40 (excluding M30).

Appendix – B

Estimation of the concrete for M2/M3 prototypes

Weight of the concrete (W) = Volume of the concrete (V) × Density (ρ) × Factor of the safety

Volume of the concrete can be calculated by using the eq. (B.1)

$$V=\left[\frac{\pi}{4}(D^2-n\,d^2)-n\,n_{fin}\,b\,h\right]L\;\;(m^3) \tag{B.1}$$

$$=\left[\frac{\pi}{4}(0.324^2-22\times0.0127^2)-22\times5\times0.002\times0.01\right]\times1\;\;(m^3)$$

$$V=0.07746\;\;(m^3)\text{ or approximately }\;0.078\;\;(m^3)$$

$\therefore W=0.078\times2450\times1.2\;\;(kg)$ Or $229.32\;\;(kg)$.

Appendix – C

Error Analysis

The theory of perturbation technique reported by Kline and McClintock, (1953) and Moffat, (1982) is used to calculate the uncertainty of any dependent parameter, which depends on certain measured quantities of the experimental studies. If a parameter ‘P’ depends on the independent variables such as u_1, u_2, u_3 ….u_n, then P can be expressed as a function of all the independent variables as given in Eq. (D.1)

$$P = P(u_1, u_2, u_3, ...u_n) \quad \text{(D.1)}$$

Then, the total uncertainty of the parameter (ΔP) is given by Eq. (D.2)

$$\Delta P = \sqrt{\left(\frac{\partial P}{\partial u_1}\Delta u_1\right)^2 + \left(\frac{\partial P}{\partial u_2}\Delta u_2\right)^2 + \left(\frac{\partial P}{\partial u_3}\Delta u_3\right)^2 + ... + \left(\frac{\partial P}{\partial u_n}\Delta u_n\right)^2} \quad \text{(D.2)}$$

Energy Stored / Discharged

The uncertainties are estimated for the energy stored/discharged, which is due to the individual uncertainties of the independent parameters. These independent parameters are temperature difference, volumetric specific heat and volume of the storage material. Energy stored/discharged in/from the storage material is calculated using the Eq. (D.3) and (D.4).

$$Q_S = \rho_s V C_{ps} \left(T(t) - T_{ini} \right) \ (J) \qquad \text{(D.3)}$$

$$Q_D = \rho_s V C_{ps} \left(T_{ini} - T(t) \right) \ (J) \qquad \text{(D.4)}$$

Applying the Kline – McClintock's rule, we have,

$$\Delta Q = \sqrt{\left(\frac{\partial Q}{\partial(\rho C_{ps})} \Delta(\rho C_{ps}) \right)^2 + \left(\frac{\partial Q}{\partial V} \Delta V \right)^2 + \left(\frac{\partial Q}{\partial k} \Delta k \right)^2} \quad (\because \Delta T = k) \qquad \text{(D.5)}$$

The maximum uncertainty in measuring the volume of the storage material is given by the following procedure.

$$V = \frac{\Pi}{4}(D^2 L) \qquad \text{(D.6)}$$

$$\frac{\partial V}{\partial D} = \frac{\Pi}{4}(2D)L \qquad \text{(D.7)}$$

$$\frac{\partial V}{\partial L} = \frac{\Pi}{4}(D^2) \qquad \text{(D.8)}$$

$$\Delta V = \sqrt{\left(\frac{\partial V}{\partial D} \Delta D \right)^2 + \left(\frac{\partial V}{\partial L} \Delta L \right)^2} \qquad \text{(D.9)}$$

$$\Delta V = \sqrt{\left(\frac{2V}{D} \Delta D \right)^2 + \left(\frac{V}{L} \Delta L \right)^2} \qquad \text{(D.10)}$$

$$\frac{\Delta V}{V} = \sqrt{4\left(\frac{\Delta D}{D} \right)^2 + \left(\frac{\Delta L}{L} \right)^2} \qquad \text{(D.11)}$$

$$\frac{\Delta V}{V} = \sqrt{4(0.01)^2 + (0.01)^2}$$

$$\Rightarrow \frac{\Delta V}{V} = 2.22\% \qquad \text{(D.12)}$$

(Since the maximum uncertainty in the measurement of diameter and length of the storage prototype are ± 1 %).

The uncertainty involved in measuring the temperature is ± 0.5 °C. The maximum uncertainty while measuring the temperature difference $(\Delta T = k)$ is given by the following procedure.

We know that $\frac{\Delta k}{k} = \frac{k_2 - k_1}{k_2}$ (D.13)

$$\Rightarrow \frac{(T_{avg2}-T_{ini2})-(T_{avg1}-T_{ini1})}{(T_{avg2}-T_{ini2})} \tag{D.14}$$

$$\Rightarrow \frac{(433.5-352.5)-(432.5-352.5)}{(433.5-352.5)}=0.025$$

$$\Rightarrow \frac{\Delta k}{k}=\pm 2.5\% \tag{D.15}$$

The maximum uncertainty in the measurement of volumetric specific heat is ± 5 %.

$$i.e., \ \frac{\Delta(\rho C_{ps})}{(\rho C_{ps})}=\pm 5\% \tag{D.16}$$

The maximum uncertainty in measuring the energy stored/discharged is given by the following procedure.

$\frac{\partial Q}{\partial k}=\rho C_p V$ i.e., $\frac{\partial Q}{\partial k}=\frac{Q}{k}$. Similarly, $\frac{\partial Q}{\partial(\rho C_p)}=Vk=\frac{Q}{(\rho C_p)}$ and $\frac{\partial Q}{\partial V}=\rho C_p k=\frac{Q}{V}$

On substituting in the eqn. (D5),

$$\Delta Q=\sqrt{\left(\frac{Q}{(\rho C_{ps})}\Delta(\rho C_{ps})\right)^2+\left(\frac{Q}{V}\Delta V\right)^2+\left(\frac{Q}{k}\Delta k\right)^2} \tag{D.17}$$

$$\frac{\Delta Q}{Q}=\sqrt{\left(\frac{\Delta(\rho C_{ps})}{(\rho C_{ps})}\right)^2+\left(\frac{\Delta V}{V}\right)^2+\left(\frac{\Delta k}{k}\right)^2} \tag{D.18}$$

On substituting all the individual uncertainties in Eq. (D.18),

$$\frac{\Delta Q}{Q}=\sqrt{(0.05)^2+(0.022)^2+(0.025)^2}$$

$$\therefore \frac{\Delta Q}{Q}=0.06 \quad or \quad 6\%$$

Therefore, the estimated uncertainty of energy stored/discharged is ± 0.84 MJ (± 6 %).

Summary

The uncertainties involved in the estimation of energy stored / discharged is ± 0.84 MJ (± 6 %).